# Numerical constitutive laws for powder compaction using particle properties and packing arrangement

Thesis submitted for the degree of

Doctor of Philosophy

at the University of Leicester

*by*

**Lida Che**

Department of Engineering

University of Leicester

2016

## Dedications

To my dear parents, Juntie Che and Jing Yu

And

To my dear wife, Mengna Liu

# Abstract

Numerical studies, calibrated and validated using experiments, were carried out to develop a constitutive law for powder compaction. In order to simulate powder compaction at particle level, single particle compression/breakage test is used to characterise the mechanical properties, which include elastic modulus, Poisson's ratio and yield strength. Finite Element Analysis (FEA) of single particle compression was carried out and validated vs. single particle compression testing and then used to establish a suitable hardening law.

The particle size, shape and packing arrangement were obtained using X-ray computed tomography. This information was transferred to FEA. Due to the presence of complex geometrical structures, Meshlab and Solidworks were chosen to deal with the arrangement of particles in the structure.

The multi-particle finite element method (MPFEM) was implemented into the finite element software package Abaqus/EXPLCIT v6.14 and used to simulate the powder compaction process. The model input parameters include mechanical properties (of the single particle) and interactions between particles (e.g. friction). The stress-strain curves predicted by MPFEM were validated experimentally using compaction tests performed in a die instrumented with radial stress sensors. The method proposed was used for constitutive model development for powder compaction as an alternative to bulk powder characterisation.

The stress-strain curves MPFEM were analysed using the deformation plasticity framework. Contours of constant complementary work in Kirchhoff stress space were established and a model consistent with the behaviour of the materials was identified in order to capture the materials response under conditions experienced in practical die compaction processes.

# Acknowledgement

Firstly, I would like to express my sincere gratitude to my supervisor Dr Csaba Sinka for the continuous support of my Ph.D study and related research, for his patience, motivation and immense knowledge. His guidance helped me in all the time of research and writing of this thesis. I could not have imagined having a better advisor and mentor for my Ph.D study.

Secondly, I would like to thank Professor Jingzhe Pan for his support and great help that make me confident to complete this degree. I also appreciated the support of Graham Clark, Alan Wale and Ian Bromley who contribute to my lab work. I would like thank all the faculties, colleagues and staff for all the supporting of my study and daily life.

A special thanks to my family. Words cannot express how grateful I am to my mother-in-law, father-in-law, my mother and my father for all the sacrifices that you have made on my behalf. Your selfless dedication for me was what sustained me thus far. At the end I would like express appreciation to my beloved wife Mengna Liu who spent sleepless nights with and was always my support in the moments when there was no one to answer my queries.

## Table of Contents

## List of Tables

## List of Figures

## List of Symbols

a contact area

A the cross-sectional area of the die

$A_H$ Hamaker constant

D diameter of particle

$D_0$ the initial relative density

$D_{ijkl}$ stress-strain matrix

E Young's modulus

$\bar{E}$ macroscopic effective strain

$E_a$ macroscopic axial strain

$E_e$ equivalent strain

$E_{ij}$ Hencky logarithmic strain

$E_p$ photon energy

$E_r$ macroscopic radial strain

$\mathrm{f_0}$ the void volume fraction

$\mathrm{F_c}$ cap surface

$\mathrm{F_{ci}}$ contact force of particle i

$F_d$ break force of diametrical compression

$\mathrm{F_{ij}^p}$ the plastic contact force between particle i and j

$\mathrm{F_b}$ bottom punch force

$\mathrm{F_n}$ normal force

$\mathrm{F_s}$ shear failure surface

$\mathrm{F_t}$ tangential force

$\mathrm{F_T}$ top punch force

$F_u$ the break force of uniaxial compression

$\mathrm{F_v}$ Van der waals force

$h$ the distance between two surfaces of particles

H hydrostatic strain

$I$ transmitted X-ray intensity

$I_0$ the incident X-ray intensity

$I_i$ moment of inertia

K elastic modulus

$k_s$ tangential stiffness coeffiicient

$m_i$ mass of Particle i

M a constant controlling the shape of the surface

$n_{ij}$ the unit vector of the centre of particle i pointed to the centre of particle j

N compression force

$p$ external pressure

P hydrostatic pressure

$p_0$ the maximum pressure of the contact surface

$P_c$ pressure on contact surface

$P_n$ normal contact force between particles

$P_y$ the hydrostatic yield stress

q Mises equivalent stess

$r_i, r_j$ radii of two particles

R particle radius

S surface area of a particle

$S_c$ surface area where particels move apart

$S_{ij}$ stiffness

t thickness

$T_{ke}$ the Kirchoff effective stress

$T_{kh}$ the Kirchoff hydrostatic stress

$T_i$ torque arising from the tangential contact force

$T_{ij}$ Kirchoff stress

u the relative approach between the centres of two particles

$u^c$ compatible deformation field

$v_i$ the Voronoi cell surrounding particle i

$V_i$ linear velocity

$V_s$ solid volume

Z coordination number

$Z_a$ the material atomic number

β internal friction angle

δ the total normal displacement

$\varepsilon_{ij}$ true strain component

$\varepsilon_{ij}^c$ compatible strain field

$\varepsilon_v$ the Von Mises uniaxial constant strain

$\bar{\Sigma}$ macroscopic effective deviatoric stress

$\Sigma_a$ macroscopic axial stress

$\Sigma_{ij}$ the macroscopic average true stresses

$\Sigma_m$ macroscopic mean stress

$\Sigma_r$ macroscopic radial stress

$\lambda_i$ principal stretches

$\mu_c$ linear X-ray attenuation coefficient of the material

ν Poisson’s ratio

$\xi_s$ the tangential displacement

$\rho_{ij}$ $(i, j = 1,2,3 \ldots)$ solid fraction

$\rho_{in}$ the initial relative density

$\rho_r$ current relative density

$\sigma_c$ the uniaxial strength

$\sigma_d$ the tensile strength from diametrical compression

$\sigma_{ij}$ (i, j=1,2,3) the component of stress

$\sigma_{rb}$ radial stress at bottom sensor

$\sigma_{rt}$ radial stress at top sensor

$\sigma_T$ top punch stress

$\sigma_v$ the Von Mises uniaxial constant stress

$\sigma_y$ material yield strength

$\tau$ shear stress

$\Psi$ implicit potential

$\omega$ work done per unit volume

$\bar{\omega}$ complementary work done per unit volume

$\omega_e$ work done per unit volume along the extremal path

$\bar{\omega}_e$ complementary work done per unit volume along the extremal path

$\omega_i$ angular velocity

$\Omega_e$ macroscopic work done per unit initial volume along an extremal path

$\bar{\Omega}_e$ macroscopic complementary work done per unit initial volume along an extremal path

# Chapter1. Introduction

## 1.1 Industrial applications of powder compaction

Powder materials are used widely in many areas of the process industries, for example, pharmaceuticals, powder metallurgy, ceramics, plastics, cosmetics, mineral processing, food processing industries and so on. It is not difficult to find that the products prepared by powder materials appear in various areas of life. Powder technology has played a positive role in the progress and development of human civilization. More and more investigators focus on this technology in different ways. Figure 1-1 shows the preparation processing of powder products, which includes filling, handling, compaction, sintering, and other operations. During the processing steps, factors that affect product performance include particle properties (including friction and cohesion between particles) and compression parameters. The performance of the product cannot be improved without the optimal design of the material and process.

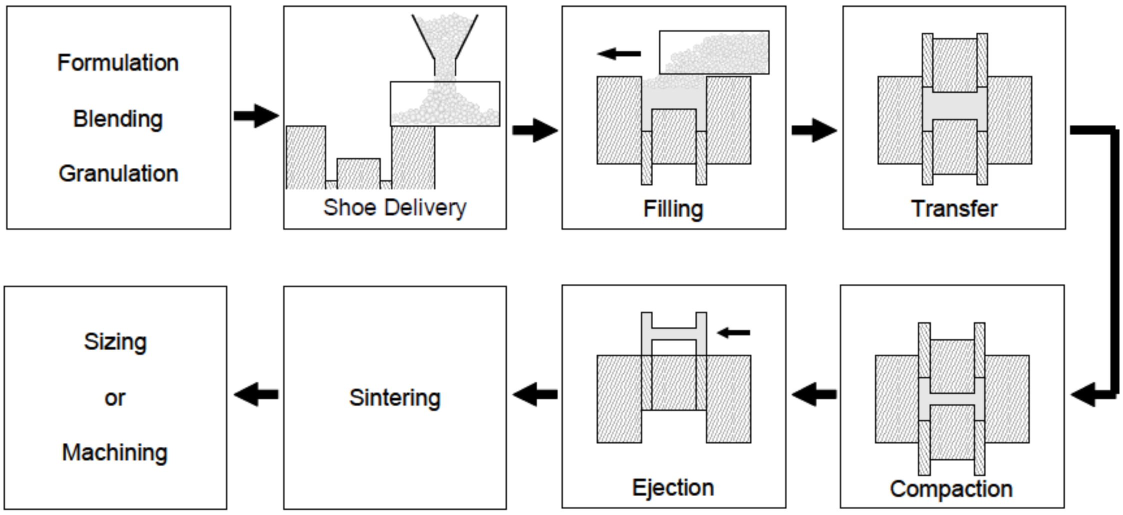


Figure 1-1 Processing steps in powder compaction technology (Schneider, 2003)

One of the most important stages is compaction where loose particles are transformed into a compact product with a high density. The compaction technology was used in powder metallurgy at first and then it was extended to other fields.

### 1.1.1 Powder metallurgy

Powder metallurgy has been an attractive technology for traditional and advanced materials. Through the compression operation, powder is formed into compacts with required shapes. Then, the green body is transformed into a final product by sintering. When a mechanical component needs to be mass produced, powder compaction is a very effective way to save time and money. In addition, materials with different properties can be tailored through powder mixing; in this case, the desired mechanical behaviour of homogeneous materials can be achieved.

### 1.1.2 Ceramics industry

Ceramic components are widely used in many sectors, which include the aerospace, electronics, biomedical and optical fields. Figure 1-2 shows typical ceramic products used in industry. The processing of dry ceramics consists of four main steps: milling, mixing, forming and sintering. Firstly, the initial ceramic material is broken up to small size particles. The material is then mixed according to the required recipe and compacted to a desired shape. Lastly, the final product is achieved by sintering processing. Compared with powder metallurgy, there are special requirements for ceramic products, such as filter ability, purity, electric isolation etc.

Figure 1-2 Ceramic products (King’s Ceramics and Chemicals Co., Ltd)

### 1.1.3 Pharmaceutical industry

In the pharmaceutical industry, powder technology is also a key processing route. Compared with metal and ceramic powders, the difference is that the final product, typically a tablet, is made without sintering processing. Figure 1-3 shows specimens of pharmaceutical tablets after compaction. The tablets can be compressed into complex shapes. In addition to mechanical strength tablets must satisfy special requirements regarding chemical stability and bioavailability.

Tablets are composite powder systems that contain active ingredients and excipients. The processing steps include: mixing, die filling and compression. Firstly, different active ingredients and excipients are mixed. Then the mixture is transferred into a die and compressed into tablets. However, the tablet compression remains a complicated engineering problem. Defects such as cracking, chipping, and delaminating may lead to insufficient mechanical integrity (Sinka et al., 2009, Wu et al., 2003, Procopio and Zavaliangos, 2005, Marin et al, 2003, Jerier et al, 2011 etc.)

Figure 1-3 Pharmaceutical tablets (Allied Chemicals & PharmaCeuticals Pvt. Ltd.)

## 1.2 Compaction methods

Compaction can be divided into quasi-static and dynamic methods. The dynamic method normally uses a loading hammer or vibration to compress for large scale. There are a several methods of quasi-static compaction, such as roller compaction, isostatic compaction, single station compaction and multi-station compaction which are described below. Only the quasi-static compaction approach (Wu, 2005a) is considered in this thesis.

Roller compaction is a dry granulation method which is considered effective to provide pre-densification and improve the flowability of the primary powders. During roll compaction, the feed powders pass through the gap between two counter-rotating rolls under gravity or feeding force. The powders are held in the reducing gap by the friction forces on the roll surface. In the area close to the minimum roll gap, the powders are compressed into a higher density ribbon. The applications of roller compaction consist of production of ceramic or metal powder sheet or strip for filter applications or for clad/bimetal production (Freund-Vector Corporation, 2012). A typical roller compactor used in pharmaceutical and chemical production is shown in Figure 1-4.

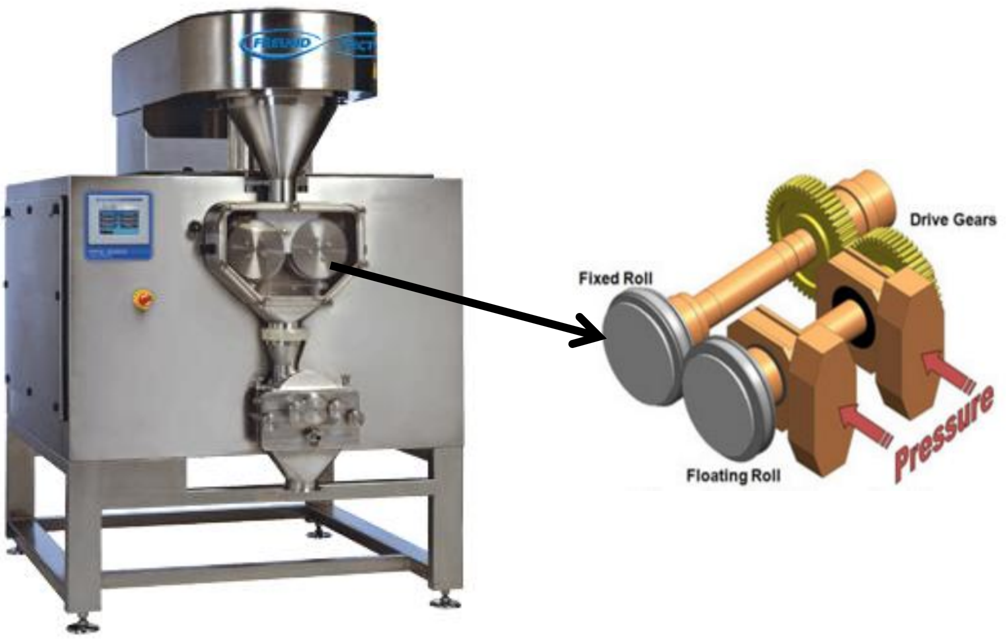


Figure 1-4 Roller compacter (Freund-Vector Corporation, 2012)

In isostatic a uniform pressure is applied simultaneously to all the external surfaces of the powder body. The alternative name of isostatic compaction is hydrostatic compaction, which is limited to liquid use as the pressure medium for rubber bag pressing. Figure 1-5 shows a model of the isostatic compaction machine. Isostatic compaction has been successfully used in powder metallurgy and ceramics.


Figure 1-5 Isostatic press ( EPSInc, USA, 1996)

Single station compaction is a type of powder compacting process that uses a die and applies compression to both upper and lower punches. The lower punch is generally used for holding powders and has a function of ejecting the tablet after compaction. And the upper punch mainly furnishes the required pressure. A single station press is shown in Figure 1-6. The powder is compressed into tablets of uniform size and weight. It can be employed in development and low-volume production and is similar to presses use for other powder system. Single station compression is used to manufacture tablets of a wide variety of materials, including pharmaceuticals, powder metallurgy, cleaning products and cosmetics.

Figure 1-6 Single station compactor (CapPlus Technologies, Inc., 2013)

Multi-station compaction has multiple die and punch sets for compacting pharmaceutical material into tablets. Typical tablets are produced using high speed rotary presses which yield a high volume of production. The die table is shown diagrammatically in Figure 1-7. A high speed rotary tablet press can produce over 500,000 tablets per hour (LFA Machines Oxford Ltd., 2016). On a rotary tablet press, the die and punch are located on a turret. As the turret rotates the punches and dies pass sequentially through the different stages of compaction, and the consolidation stage occurs when the punches and dies make contact with the compression rollers. The tablet manufacturing cycle is consisting of die fill, weight adjustment, powder pre-compaction and main compaction and tablet ejection.

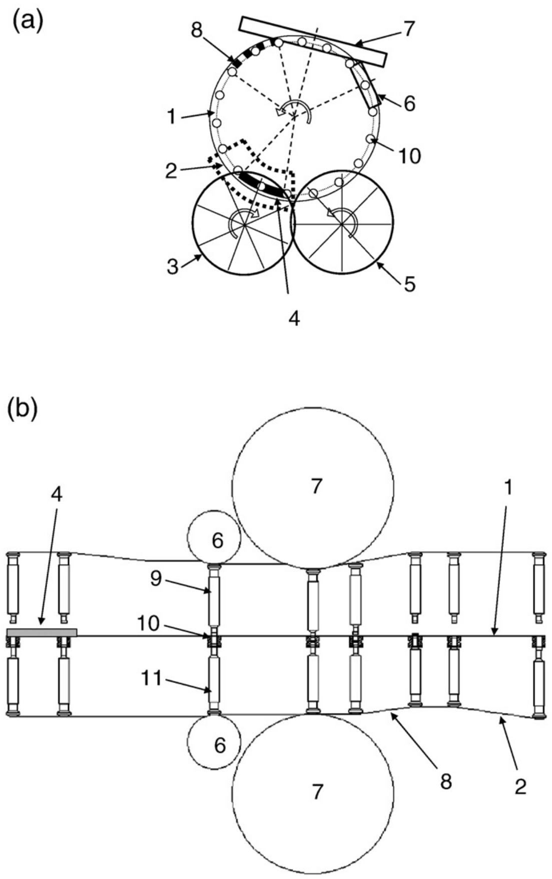


Figure 1-7 “Rotary press production cycle a) top view, b) unfolded view; 1 — die table, 2 — fillcam, 3—feed wheel with paddles, 4—die fill area, 5—metering wheel with paddles, 6—pre-compression roller, 7—main compression roller, 8—ejection cam, 9—upper punch,10 — die, 11 — lower punch.” (Sinka et al., 2009)

## 1.3 Research trends in simulation of powder compaction

Common requirements for powder products include strength, density uniformity, dimensional tolerance and weight uniformity as described above. There are expensive experiments and unsuitable procedures that are used currently in industry. To understand material behaviour and to improve product performance, the numerical approach is considered as an effective solution for predicting material characteristics.

The numerical methods over the past 10-30 years have been based on Finite Element Analysis (FEA) and Discrete Element Method (DEM). FEA can incorporate a wide range of constitutive models that describe the mechanical transformation from loose powder state to fully dense material. To model practical powder compaction processes, it is necessary to consider realistic particle shapes, packing arrangements and appropriate constitutive laws. The multi-particle FE model is considered in this thesis to develop constitutive laws for the modelling of actual powder compaction process.

## 1.4 Research aim and thesis structure

The overall aim of this research is to develop a methodology to obtain numerical constitutive laws for powder compaction as an alternative to experimental characterisation of bulk compaction behaviour.

Chapter 2 presents a literature review of the constitutive laws for powder compaction. The multi-particle finite element method (MPFEM) for modelling die compaction is described. A review of the literature of experimental characterisation techniques of powder compaction is provided. The use of X-ray CT techniques for characterising particle shape and packing arrangement is introduced.

Chapter 3 is concerned with the compression behaviour of single particles. Experiments are carried out to obtain mechanical properties for use as input data in FEA of single particle compression.

Chapter 4 presents an experimental study of the compaction behaviour of bulk powders using the instrumented die system. The experimental procedure and data analysis procedure is described and the constitutive model parameters are determined.

Chapter 5 describes the use of X-ray computed tomography (CT) to characterise the

3D packing arrangement of particles. This information is used as input into MPFEM.

A model using MPFEM is created in Chapter 6 and implemented in the finite element software Abaqus. MPFEM is used to generate stress-strain curves under radial loading conditions in strain space. The input data are the particle properties (Chapter 3) and packing arrangement (Chapter 5) and the model prediction is validated against bulk compaction experiments (Chapter 4) for closed die compaction.

Chapter 7 Presents an analysis of the stress strain curves obtained numerically using the framework of defamation plasticity and the parameters of the constitutive model are determined.

Finally, the overall conclusions and future work from this research are summarised in Chapter 8 and 9, respectively.

# Chapter 2. Review of literature and research objectives

In materials engineering, the relationship between material deformation and loading (or a stress-strain relationship) is termed constitutive law. Hooke's law is the simplest constitutive law which describes linear elastic materials (Whelan and Hodgeson, 1978). Plastic behaviour is described using a yield condition.

## 2.1 Review of experimental characterisation techniques

### 2.1.1 Bulk powder compaction

The compaction behaviour of powders is an important characteristic since it affects the final product properties. The powder compaction process depends on a number of different factors including particle properties such as particle shape, size distribution, elastic and plastic properties and friction. However, the relationship between single particle properties and bulk compression behaviour has not yet been fully understood. Extensive studies have been carried out into the compaction properties of metal powders (Gan & Gu, 2008; Sivasankaran et al., 2010), ceramics (Nagarajan et al., 1997; Vogler et al, 2007) and pharmaceutical materials (Michrafy, et al., 2002; Zhang et al., 2006; Yap et al., 2008; Frenning et al. 2009; Klevan et al. 2009; Klevan et al., 2010). The deformation mechanisms of powders undergoing compression is illustrated in Figure 2-1 (Stasiak et al., 2010).

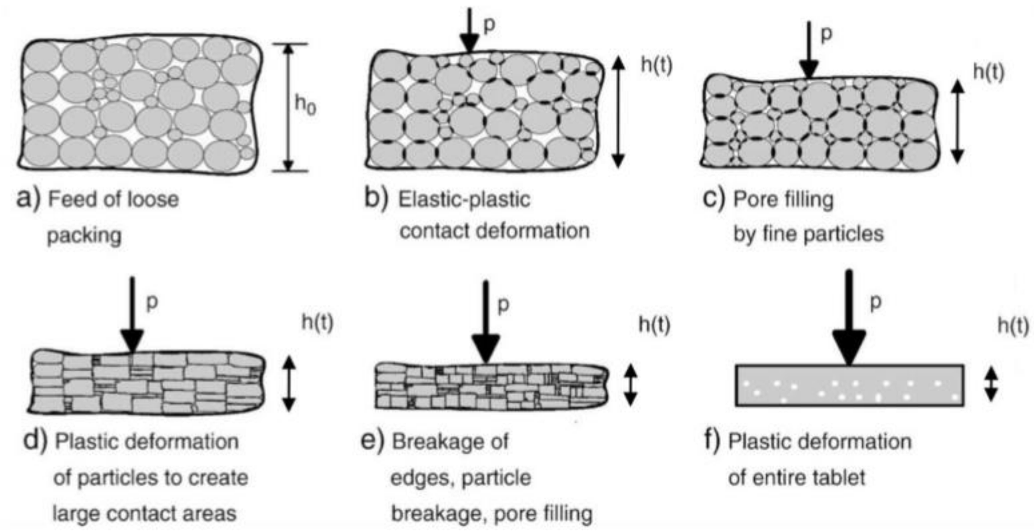


Figure 2-1 A general schematic of mechanisms of powder compression (Stasiak et al., 2010)

Powder compaction can be carried out using isostatic and uniaxial compaction (Govindarajan and Aravas, 1994). In this thesis, only die compaction techniques are involved. A large number of die compaction experiments have been carried out by researchers (Briscoe and Rough, 1998, Turenne et al., 1999; Wikman et al., 2000; Guyoncourt et al., 2001 and Cunningham et al., 2004). Because of friction between powder and die, the die compaction is generally classified into three types as shown in Fig 2-2 (Wu, 2005a).

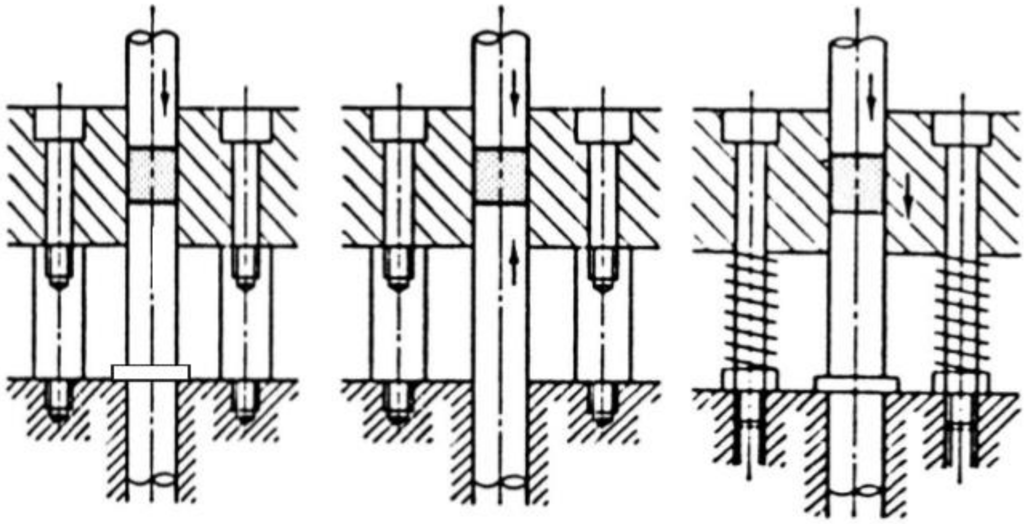

(a) (b) (c)

Figure 2-2 Three categories of close die system: (a) Single-action compaction system, (b) Double-action compaction system, (c) Floating die system (Wu, 2005a)

Single-action compaction (Figure 2-2 a) involves a moving upper punch, a fixed lower punch and a fixed die plate. The upper punch applies axial pressure within the powder mass. For the double-action compaction (Figure 2-2 b), both top and bottom punches compress powder at the same time, and the die plate is fixed. The floating die system is similar as single-action compaction, but the die table is supported by the springs as is shown in Figure 2-2 c.

Friction plays a key role in die compaction. There are a few factors can affect the coefficient of friction between die wall and powder such as the nature of the powder material, sliding velocity and contact pressure. To minimise friction, lubricants are added to lubricate the punch and die. Commonly used lubricants include Magensium Stearate, Zinc Stearate, Calcium Stearate, ethylene bis-stearamide etc ( Wornyoh et al., 2007).

The compaction process of powders involves a complex densification mechanism, such as rearrangement, contact between particles resulting in elastic and plastic deformation, fragmentation of particles and formation of interparticulate bonds. A constitutive law which describes this mechanical behaviour should capture all these mechanisms from loose powder to compact material. This requires an understanding of the mechanisms taking place at particle level.

### 2.1.2 Particle packing

Particle packing is important in powder compaction. German (1989) states that the bimodal and trimodal mixtures can increase the packing density, however, in order to find out an optimal configuration the composition and particle size ratio must be carefully determined.

Studies in particle packing arrangement date back to the 1960s (Ridgway and Tarbuck, 1967; Sloane, 1984; Cumberland and Crawford, 1987; Smith, 1953). In 1694, Newton and Gregory were concerned with packing of spheres and studied the maximum coordination numbers for equal sized spheres. They thought that the maximum coordination number for spheres is 13 because of the solid angle subtended by a contacting sphere is less than 1/13 of the total. Rumpf and Gupte (1975) demonstrated that a maximum coordination is 12 for ordered packing.

#### 2.1.3.1 Ordered packing

In two dimensions, particles can be packed into ordered and random structures. The packing arrangement does not totally describe the basic structure because of the particle shape. Significant overlap of the disks is required to attain total coverage with an estimated excess in disk area of 21% over the covered area necessary to produce a complete covering (Rogers, 1964 and Kingman, 1965). As a sequence, a disk (2D) or a sphere (3D) is considered as a low packing efficiency object.

There are two ordered packing arrangement of disks as shown in Figure 2-3 (Heyliger , 2013). According to the number of the contact points for each disk, which is the coordination number and the fractional density, they observed that the packing density increases with the coordination number. Here, only four-fold and six-fold geometry, which show that one particle has four and six contacts, are considered with calculated packing density of 0.7854 and 0.9069. However, a statistical model of packing arrangement shows a density of 0.42 for a coordination of two (Nikolenko and Kovalchenko, 1985). The structure of the six-fold (contacts) geometry gives the theoretical maximum packing density for disks (Rogers, 1958) and is the same as that which builds up the densest ordered packing in 3D.

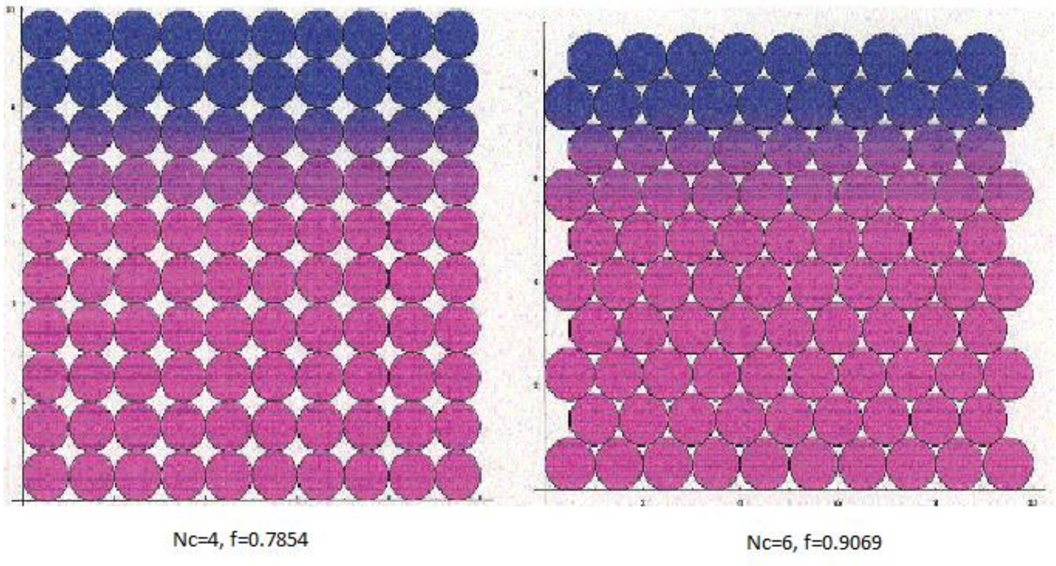


Figure 2-3 Ordered packing in two dimensions with coordination numbers of four and six (Heyliger , 2013).

### 2.1.3.2 Random packing

The difference between an ordered and random packing is shown in Figure 2-4 (McDonoghet al., 1998). The ordered structure shows a uniform arrangement and an average of contact points. Compared with random structure, it shows different coordination number, packing density and void size. The random packing is dependent on the assembling procedure of the packing arrangement. Under the random conditions, an assumed unidirectional force, such as gravity or a central attraction force is normally used in contact of the disks. This can be defined and simulated in computer, for example, by defining an assembly routine for the particles entering into a container under gravity and depositing into a given packing.

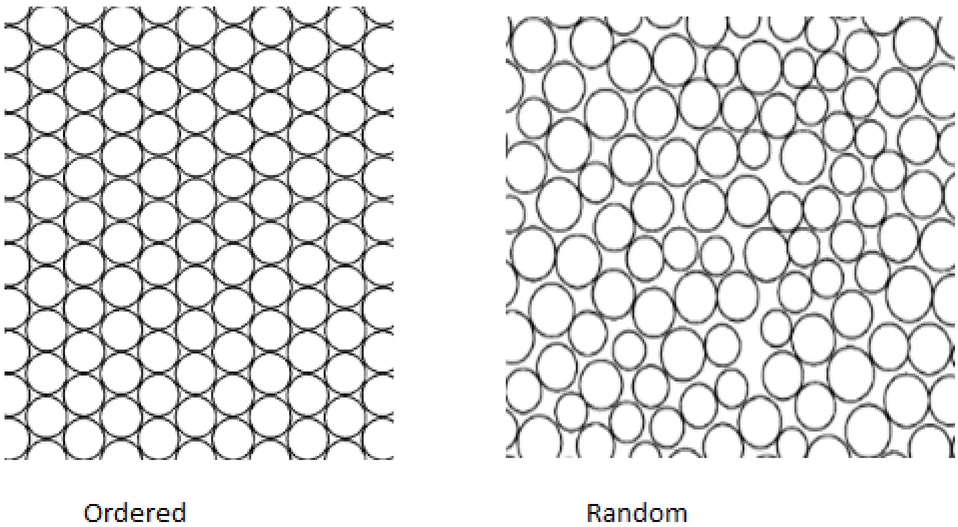


Figure 2-4 Contrast the structure of ordered array and Random array (McDonoghet al., 1998)

.

## 2.2 X-ray Computed Tomography

X-ray CT is a non-destructive inspection technique that gives cross-sectional images in planes through components (Kak, 1979). The X-ray CT apparatus mainly consist of an X-ray source and a detector as shown in Figure 2-5. The specimen is placed on a precision stage in the path of the X-ray beam. A detector array is involved to measure the intensities of the X-ray beam launched through the specimen. The specimen is rotated in the beam during scanning. In early or large devices, the X-ray source and detector rotates at the same time in order to obtain the 2D projections (Lin and Miller, 2001). However, the lab-scale devices are currently based on the rotation of the sample instead of simultaneous rotation of the source and detector.

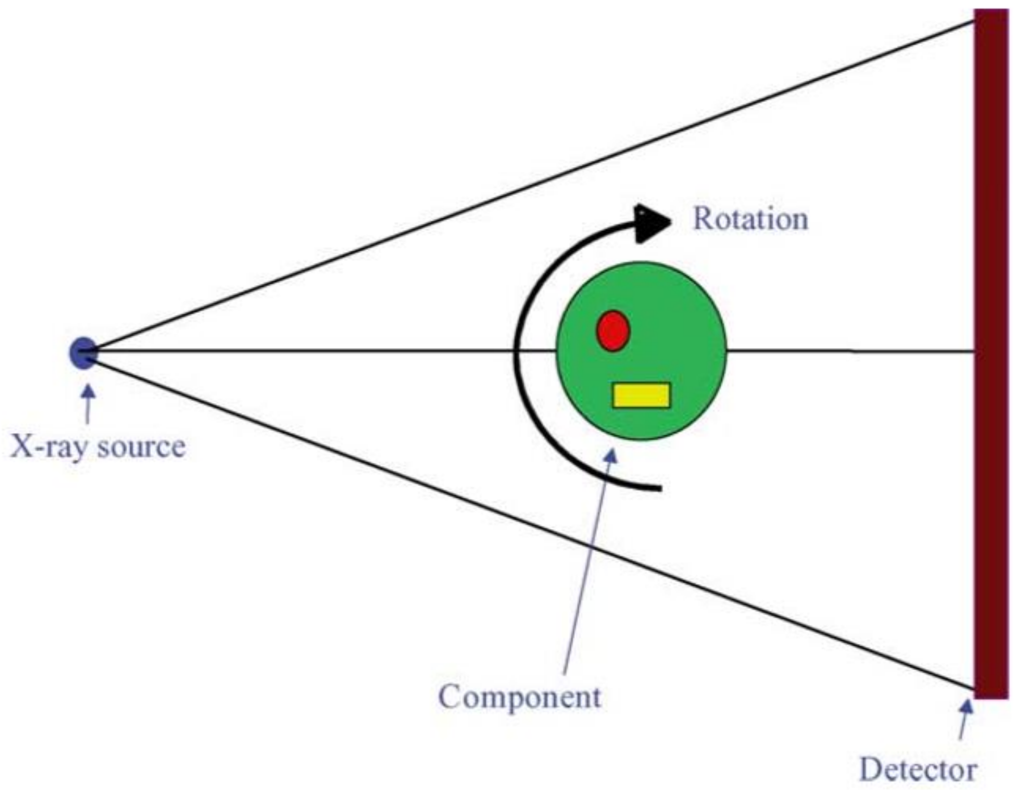


Figure 2-5 The schematic diagram of a X-ray CT device (Sinka et al., 2004)

From the measured transmitted intensities, a mathematical algorithm is used to reconstruct the CT images (Mersereau, 1974). The achieved CT images are true cross-section images. If a small size X-ray source is used, the spatial resolution can increase, for example, to 10 μm for mm sized specimen. The CT image values, which are grey levels, gives information on the material X-ray attenuation coefficient at every point in the image. Of considerable interest is the correction for a number of effects, especially beam hardening, which will allow the grey levels to be alternated to value of the local material density (Phillips and Lannutti, 1997; Burch 2001a, b). Thus, generally speaking, it is necessary to measure and correct for the non-linear effects of beam hardening, because the X-ray source generates radiation having a broad spectrum of photon energies. The dependence of the transmitted X-ray intensity $(I)$ on the linear X-ray attenuation coefficient of the material ($\mu_c$) can be expressed by

$$I = I_0 e^{-\mu_c t} \tag{2-1}$$

Where $I_0$ is the incident X-ray intensity, t is the thickness of the material. As the beam passes through the material, the lower energy is absorbed first since the linear X-ray attenuation coefficient is energy dependent (Lin and Miller, 2001):

$$\mu_c = \rho\left(a + \frac{b{Z_a}^{3.8}}{{E_p}^{3.2}}\right) \tag{2-2}$$

Where $\rho$ is the material density, $Z_a$ is the material atomic number, $E_p$ is the photon energy and a, b are the material constant.

Applications of X-ray computed tomography (CT) are widely used in variety of scientific and industrial fields, for instance: mechanical properties (Busignies et al., 2006; Mueth et al., 2000); colloidal deposition during filtration (Li, Lin, Miller, & Johnson, 2006); analysis of granule structures (Ansari & Stepanek, 2006b); mixing and segregation (Jia et al.2007; Yang & Fu, 2004) porous media (Betson, Barker, Barnes, Atkinson, & Jupe, 2004; Nakashima & Watanabe, 2002; Spanne et al., 1994; Wong, 1999) pore structure analysis of filter cakes (Lin&Miller, 2001); visualisation of catalyst thickness around bubbles during fluidisation (Kai et al., 2005); analysis of the mixing of solids in a double cone blender using marker particles (Chester et al., 1999) and determination of moisture content during drying of sludge (Leonard et al., 2003). X-ray CT is also being used for other industrial applications, such as the analysis of voidage in minerals and applications in hydrology (Lin, Miller, & Cortes, 1992; Miller, Lin, & Cortes, 1990; Wildenschild et al., 2002).

The X-ray CT and computer simulations were first combined in the 1990s to analyse the detail of the material structure (Olson & Rothman, 1997; Spanne et al., 1994). More recently the conjunction of the X-ray technics and computer simulations has become widespread in many different fields such as the analysis of fluid flow through a porous network, permeability of microstructures, hydraulic properties, dissolution of tablets, and particle compression (Lin & Miller, 2004; Sukop et al., 2008; Lu, Landis, & Keane, 2006; Selomulya et al., 2006; Spanne et al., 1994; Karpyn & Piri, 2007; Vogel, Tolke, Schulz, Krafczyk, & Roth, 2005; Jia & Williams, 2006, 2007; Golchert, Moreno, Ghadiri, & Litster, 2004; Golchert, Moreno, Ghadiri, Litster, &Williams, 2004). X-ray CT and computer simulations are combined by characterising structural distribution through the use of X-ray CT and comparing to the predictions of computer simulations.

For particle packing, the 3D structure of dense random packings representative of particles have been achieved by X-ray system using image processing routines (Fu et al., 2006). It captured the particle size and shape distributions for mono-spherical particles. In Fu et al. (2006) study, a DEM model for the powder packing was built based on individual particle information obtained from X-ray CT (shown in figure 2-6). This methodology shown a novel method of linking the internal structure of particle agglomerates.

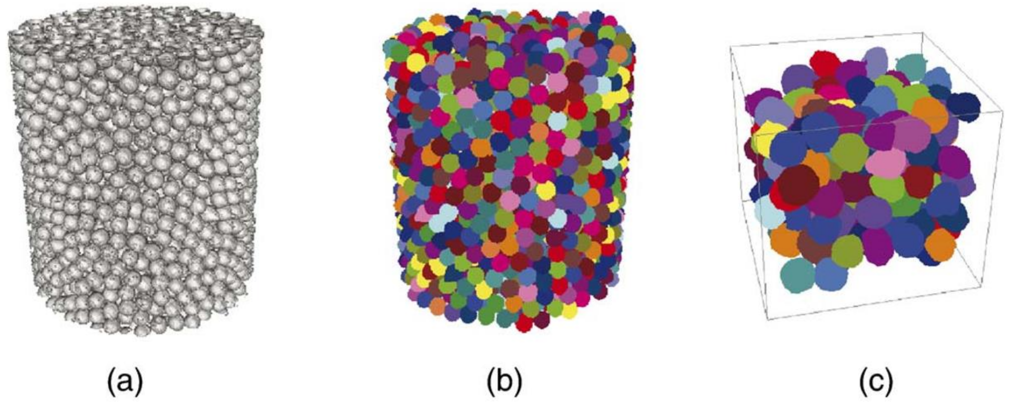


Figure 2-6 (a) 3D reconstruction in X-ray CT; (b) 3D objects from image segmentation on (a) and (c) a magnified part of packed particles (Fu et al., 2006).

In this research, the real particle shape and packing arrangement will be characterised using X-ray CT and the structural information is transferred into finite element analysis.

## 2.3 Modelling approaches

### 2.3.1 Discrete approach

DEM was created by Cundall and Strack in 1979 and immediately received the attention of scholars, who develop it constantly. This numerical simulation method is designed to solve the problem of non-continuum mechanics. The granular medium of non-continuum consists of discrete particles which locate independently from each other and interact at contact points. Local translation, rotation and deformation in the particles are allowed and also, the contact surface can be deformed, separated and slipped. Hence, the nonlinear deformation characteristics can be simulated factually under constitutive relationships. With the development of the numerical algorithms and computing capability, it becomes possible to simulate large amounts of particles numerically; thus DEM became widely used to solve engineering problems, especially in powder mechanics.

In DEM the solution space is discretized into an array of discrete elements. Adjacent elements can interact. The relative displacement is the basic variable. Through the relationship of relative displacement and force, the normal and tangential force is obtained between two elements; then, the total force and moment are calculated by summation of the forces resulting from interactions with other elements and the external forces on the element from other physical fields. According to Newton's second law of motion, the acceleration of the element is calculated; the velocity and displacement of the element are obtained by integration. Thus the physical quantities of any element at any moment (e.g. acceleration, velocity, angular velocity, displacement, etc.) are obtained.

**Motion equation**

DEM is generally used to model the dynamic processing of multi-particles. According to Newton's equations of motion, the translational and rotational motions of individual particles are given by:

Translational

$$m_i \frac{dV_i}{dt} = F_{ci} + F_v + m_i g \quad (2\text{-}3)$$

Rotational

$$I_i \frac{d\omega_i}{dt} = T_i \quad (2\text{-}4)$$

Where $m_i, I_i, V_i, \text{and } \omega_i$ are mass, moment of inertia, linear velocity and angular velocity of the particle i. $m_i g$ is the gravity. $F_{ci}$ is the contact force which includes the normal force $F_n$ and tangential force $F_t$, and $F_v$ is the Van der waals force. $T_i$

is the torque arising from the tangential contact force.

**Tangential force model**

Generally, the particle is not perfectly spherical; there are complex textures on the particle surface. The presence of these textures and the deformation of the particle during collision give rise to tangential forces. The tangential force model was implemented by many researchers (Kruggel-Emden et al., 2007, Tsuji et al., 1992 and Cundall and Strack, 1979). The Cundall and Strack model assumed that there is a virtual spring on the contact point between particles when two particles contact with each other. The formulation of tangential force $\mathrm{F_t}$ is given by:

$$\mathrm{F_t} = -\min\left(\left|\mathrm{k_s}\xi_\mathrm{s}\mathrm{n_{ij}}\right|, \left|\mu\mathrm{F_n}\right|\right) \times \mathrm{sgn}(\xi_\mathrm{s})\mathrm{S_{ij}} \tag{2-5}$$

Where $\mathrm{k_s}$ is tangential stiffness coefficient, $\mathrm{n_{ij}}$ is the unit vector of the centre of particle i pointed to the centre of particle j, $\xi_\mathrm{s}$ is the tangential displacement and $\mathrm{S_{ij}}$ is stiffness.

**Van der Waals force model**

Besides the contact force and gravity, Van der Waals force between particles needs to be considered particularly for small particle sizes. The solution of Van der Waals force $\mathrm{F_v}$ is shown as:

$$\mathrm{F_v} = \frac{A_H}{6\mathrm{h}^2}\frac{\mathrm{r_i r_j}}{\mathrm{r_i}+\mathrm{r_j}}\mathrm{n_{ij}} \tag{2-6}$$

in which is $A_H$ Hamaker constant, h is the distance between two surfaces of particles and $\mathrm{r_i}, \mathrm{r_j}$ are radii of two particles.

**Elastic contact law**

Usually, the particle deformation is described by elastic-plastic contact laws. The elastic part of the contact force is given by Hertz contact law (Johnson, 1985). The normal elastic Force $F_{ij}^{e}$ between two spheres i and j as a function of their overlap $h_{ij}$

$$F_{ij}^{e} = \frac{4}{3}(\frac{1-\nu_i^2}{E_i} + \frac{1-\nu_j^2}{E_j}) \cdot \sqrt{R_{ij}^{*} h_{ij}^{\frac{3}{2}}} \quad (2\text{-}7)$$

where $R_{ij}^{*}$ equal to $(R_iR_j)/(R_i+R_j)$, $E_i$ and $E_j$ are the Young's modulus of their constitutive materials. $\nu_i$ and $\nu_j$ are Poisson's ratio.

**Elasto-plastic contact law**

Particle contact deformation can be irreversible; in this case plastic deformation must be taken into account. Storaker's plastic force-law is commonly used for this purpose (Storaker et al., 1997). In the limiting case of a rate-independent material, it is based on a hardening and rigid-plastic Von Mises material.

$$\sigma_v = \sigma_0 \varepsilon_v^{\frac{1}{m}} \quad (2\text{-}8)$$

where $\sigma_v$ and $\varepsilon_v$ are the Von Mises stress and strain. $\sigma_0$ and $m$ are material constants. Storaker's force-law provided a normal plastic force between the particles i and j as a function of $\sigma_0$ and m. where $c(m) = \sqrt{1.43e^{\frac{-0.97}{m}}}$ is related to the area of the contact zone. This plastic force-law is derived from the finite analysis and Hill's theory of the rigid sphere – deformable plane indentation problem.

$$F_{ij}^{p} = \pi\sigma_0 2^{\frac{2m-3}{2m}} 3^{\frac{m-1}{m}} C(m)^{\frac{2m+1}{m}} R_{ij}^{*\frac{2m-1}{2m}} h_{ij}^{\frac{2m+1}{2m}} \quad (2\text{-}9)$$

The combination of the Storakers's model with Hertz contact is often used to represent DEM of particle compaction (Martin et al, 2003). However, these models are limited to the initial stages of compaction. Particle deformation is given at contacts and interaction between neighbouring contacts is usually ignored. The models are considered valid up to a relative density around 0.85 (Jerier et al., 2011). A high density model which overcomes this limitation by considering the contact interferences was developed by Jerier (Jerier et al, 2011).

**High density model**

For high density compaction analysis, the influence on each contact force around all particles must be taken into consideration. The use of the Voronoi cells enabled the analysis of the influence of neighbouring contacts (Artz, 1982). A 3D Voronoi partition of the packing is defined and the packing volume is the sum of all Voronoi cells. The simulation of packing of 4000 spheres generated by a geometric algorithm (Jeirer et al., 2009) is presented in Figure 2-7. The local solid fraction of the weighted Voronoi partition associated with particle i:

$$\rho_i = \frac{4}{3}\frac{\pi R_i^3}{v_i} \tag{2-10}$$

where $v_i$ is the Voronoi cell surrounding the particle i. It can state that $\rho_i$=1 means that the volume of the cell is completely filled by the material originally contained in the particle i. A solid fraction $\rho_{ij}$ is proposed to define the contact level between particle i and j for the force-law of DEM of high density compaction (Harthong et al., 2009):

$$\rho_{ij} = \frac{1}{2}\left(\rho_i + \rho_j\right) \tag{2-11}$$

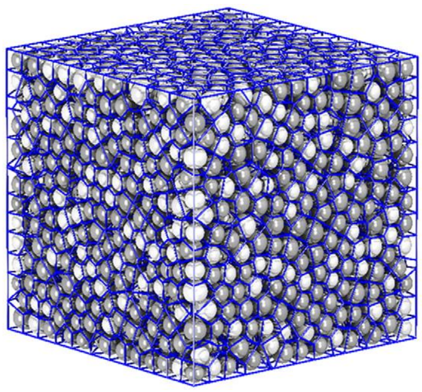

Figure 2-7 4000 packing spheres showed with the associated Voronoi cells (Jerier et al, 2011)

Figure 2-8 shows the cubic unit cell with a single spherical particle from FEM solutions of isostatic compaction. Harthong et al. (2009) determined a contact-law to describe the elastoplastic deformation of a particle. The initial solid fraction of the unit cubic is $\rho_0$=0.52. The normal force $F_{ij}$ of the "high density" force-law between the same radius R of particles i and j as a function of the parameters $\sigma_0$ and m of the particles (Harthong et al, 2009) is:

$$F_{ij}(t+\Delta t) = F_{ij}(t) + 2\sigma_0 R S_{ij}\left(m, \frac{h_{ij}}{R}, \rho_{ij}\right)\Delta h_{ij}(t) \qquad (2\text{-}12)$$

The stiffness $S_{ij}$ is given by:

$$S_{ij} = \alpha_1(m)e^{\beta_1(m)\frac{h_{ij}}{R}} + \alpha_2(m)e^{-\beta_2\frac{h_{ij}}{R}} + \alpha_3(m)\frac{\left[\max\left(0,\rho_{ij}-\rho_0\right)\right]^2}{1-\rho_{ij}} \qquad (2\text{-}13)$$

where $\rho_0$ is the solid fraction, which is resulting from the identification procedure of the law, and $\alpha_1, \alpha_2, \alpha_3, \beta_1$ and $\beta_2$ are parameters that are calculated using m:

$$\left\{\begin{matrix} \alpha_1(m) = 0.97 - \frac{0.58}{m} \\ \alpha_2(m) = \frac{15}{1+\frac{3}{m}} - 4 \\ \alpha_3(m) = 15\left(1 - \frac{1}{2m}\right) \\ \beta_1(m) = 1.75\left(1 + \frac{1}{2m}\right) \\ \beta_2 = 8 \end{matrix}\right\} \qquad (2\text{-}14)$$

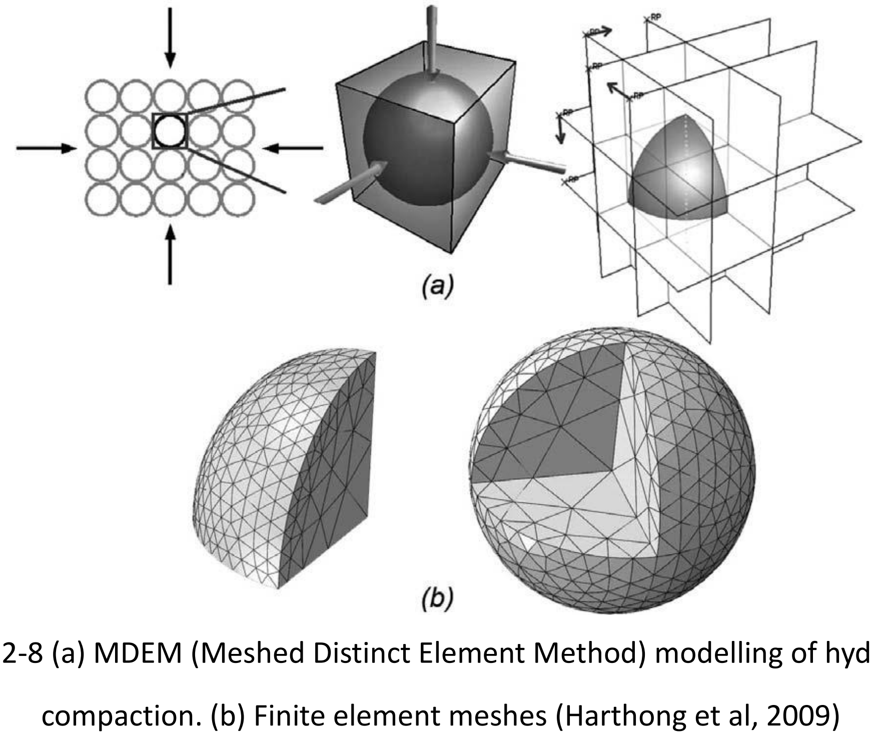

Figure 2-8 (a) MDEM (Meshed Distinct Element Method) modelling of hydrostatic compaction. (b) Finite element meshes (Harthong et al, 2009)

To validate the high-density force-law, the simulations of isostatic and die compaction with both DEM and MPFEM has been carried out as illustrated in Figure 2-9 by Jerier et al. (2011). The models include the same initial packing of 32 spheres of radius (0.15mm) located into a cube of 1mm length.

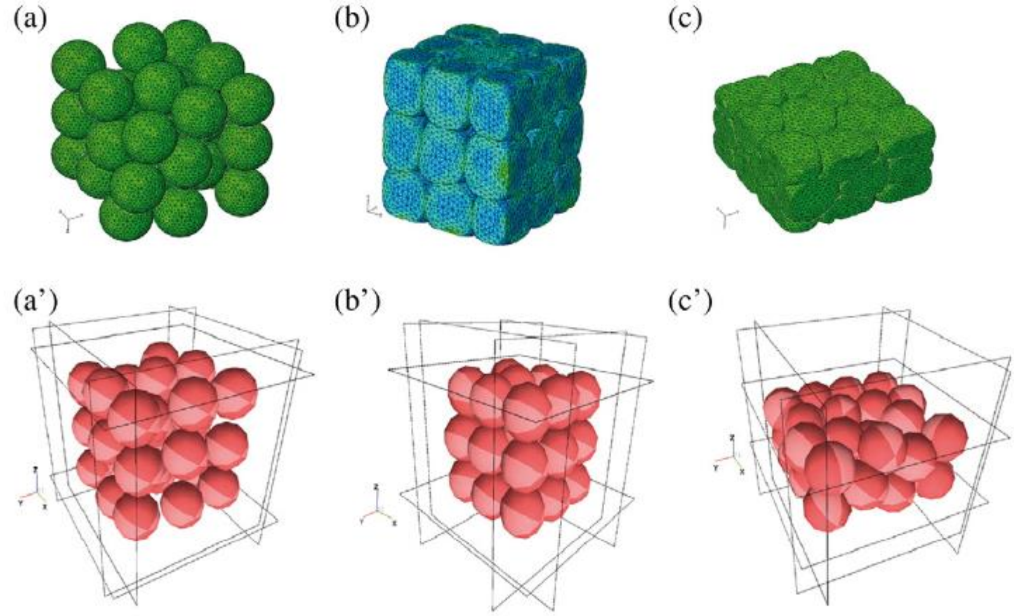


Figure 2-9 (a-b-c) 32 meshed spheres and compacted with MPFEM for isostatic (b) and uniaxial loading (c). (a'-b'-c') 32 spheres compacted with the DEM for isostatic (b') and uniaxial loading (c') using YADE Software (Jerier et al. 2011).

The case of isostatic compaction was set-up by six walls moving at a constant velocity. The stress-relative density was measured and obtained from MPFEM, DEM with the force-laws presented above and Storakers' model and shown in Figure 2-10a. The spheres are made of lead ($\sigma_0 = 20.5$MPa and m= 4.17). A good agreement was obtained between experimental and the MPFEM and DEM results with a high-density model up to a relative density equal to 0.95. However, Storakers model deviated for relative density greater than 0.85. In Figure 2-9b, the experimental data (James, 1977) was compared with an isostatic compaction model for copper ($\sigma_0 = 500$MPa and m=

3.33).

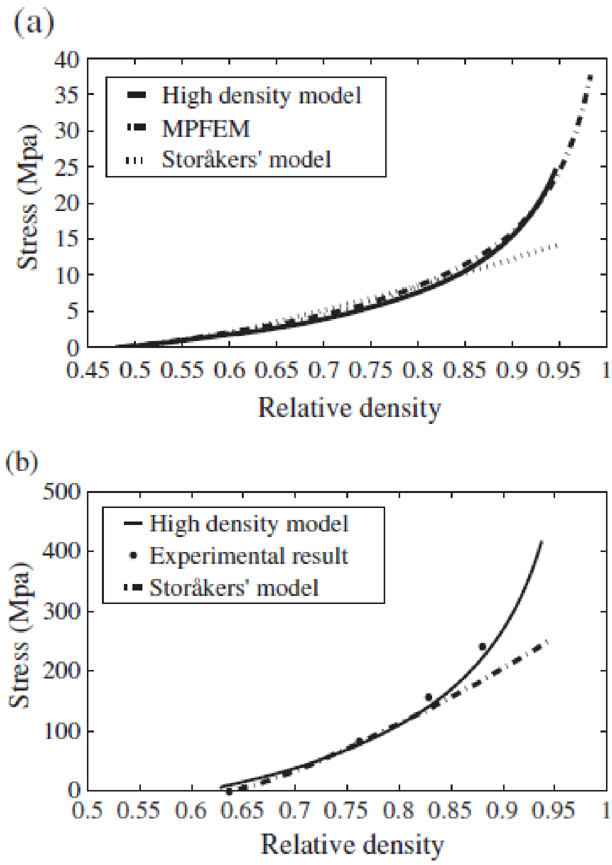


Figure 2-10 (a) Isostatic compaction using the "high density" contact law, MPFEM and Storakers' s law using the spheres made of lead in a random packing without friction. (b) Isostatic compaction of powder copper between experimental result done by James (1997), St

In the case of uniaxial compaction, the frictionless 32 spheres were compacted along one direction by a moving horizontal wall, whereas other walls were kept fixed (Figure 2-8b). The results are shown in Figure 2-11. It can be observed that the MPFEM and the "high-density" model have a good agreement when the relative density is lower than 0.9. As indicated above, a limit at a relative density of 0.85 was identified for Storakers' model for die compaction.

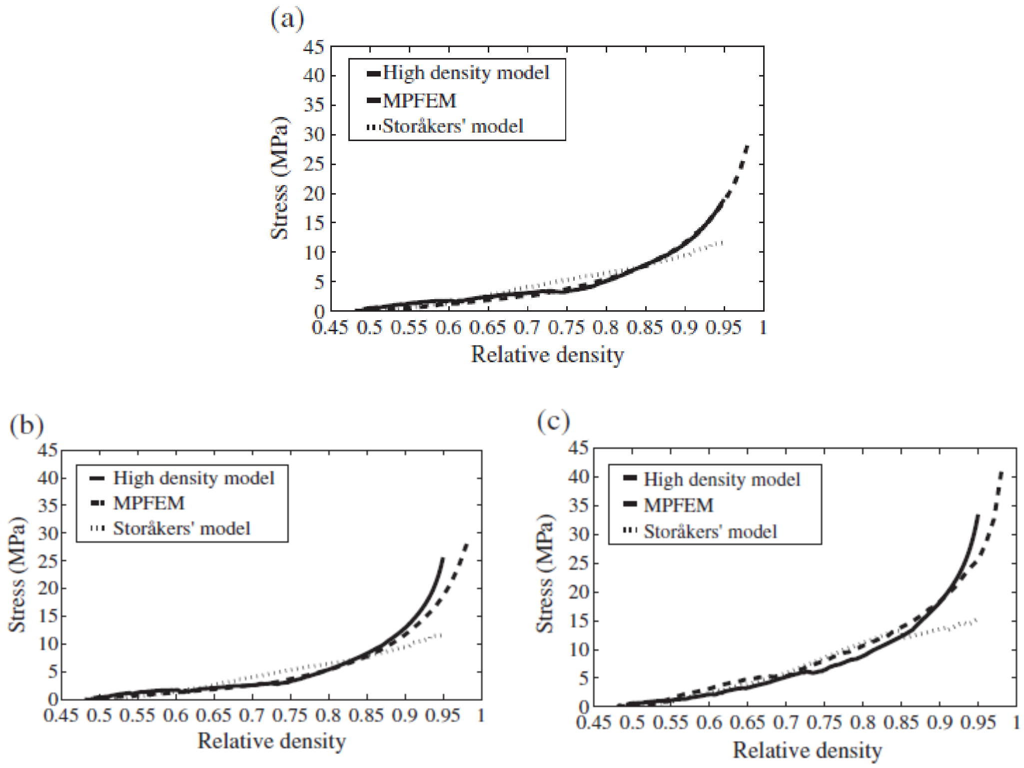


Figure 2-11 Stress-relative density curves from DEM and MPFEM for uniaxial compaction of 32 lead spheres in random packing without friction (a) X-axis, (b) the Y-axis and (c) the Z-axis (Jerier et al. 2011).

The "high density" contact law introduced a new parameter which represents the local solid fraction. This allows incorporating of the effects of plastic incompressibility into DEM simulations. The results represented above are interesting and show that the high-density model can lead to accuracy under conditions considered (spherical particle, no cohesion and frictionless contacts).

To summarise the discrete element method, the movement and deformation of the particles are described in terms of the interactions between individual particles. DEM was used successfully in large scale computation of powder flow and compaction. For powder compaction, particles are assumed as circles in 2D and spheres in 3D and can overlap or detach. However, usually DEM simulations ignore rotational stiffness.

Experimental and numerical research confirmed that particle rolling has a considerable effect on the macroscopic response of particles (Oda et al., 1982 and Oda and Iwashita, 2000). During compaction, there are strong changes in particle geometry such as resistance in rotation. As a result, DEM does not consider information regarding the stresses and strains inside the particles.

### 2.3.2 Continuum approach

During compaction the powder changes from a loose state into a dense compact. In the continuum approach, the powder is considered as a mechanical continuum given that the size of particle (typically tens of μm) is significantly smaller than the compressed specimen (typically tens of mm). Plastic behaviour is described using a yield condition. The yield surface can be determined by different tests which include simple shear, simple compression, triaxial compression (Koerner, 1971 and Doremus et al., 1995), closed die compaction (Watson and Wert, 1993), and hydrostatic compression (Kim et al., 1990).

The stress measures are defined as follows. The hydrostatic pressure $p$ and Mises equivalent stress $q$ are given by:

$$p = \frac{1}{3}(\sigma_{11} + \sigma_{22} + \sigma_{33}) \tag{2-15}$$

$$q = \sqrt{\frac{1}{2}[(\sigma_{11} - \sigma_{22})^2 + (\sigma_{11} - \sigma_{33})^2 + (\sigma_{22} - \sigma_{33})^2] + 3\sigma_{12}{}^2 + 3\sigma_{13}{}^2 + 3\sigma_{23}{}^2} \tag{2-16}$$

Where $\sigma_{ij}$ (i,j=1,2,3) are the component of stress.

### 2.3.2.1 Gurson model

The Gurson model is one of the most widely known micromechanical models to represent void nucleation in fully dens materials (Gurson, 1977). This model has been modified to include higher porosity of the material (Tvergaard, 1981) and used to simulate plasticity in porous materials. The yield function has the following form:

$$F' = \left(\frac{q}{P_y}\right)^2 + 2f_0 \cosh\left(\frac{\sqrt{3}}{2}\frac{p}{P_y}\right) - (1 + f_0^2) = 0 \qquad (2\text{-}17)$$

Where $P_y$ is the hydrostatic yield stress and $f_0$ is the void volume fraction. However, the disadvantage of this model is the assumption of the same strength in tension and compression (Shang, 2012). Other constitutive models were adapted from soil mechanics, and which included the Cam-Clay (Schofield and Worth, 1968) and the Drucker-Prager (Drucker and Prager, 1952). More recently micromechanical models (Fleck, 1995) were developed for powder compaction.

### 2.3.2.2 Cam-Clay model

The Cam-clay model dates back to the 1960s (Schofield and worth, 1968) and has been developed to solve the boundary value problems in soil media (Gens and Potts, 1988 , Yu, 1998, Sun and Kim, 2013 and Abdelhafeez and Essa, 2016). The modified model shows as a quadratic expression of the deviatoric and mean stress which is written in the form

$$F' = \frac{p}{P_y}\left(\frac{p}{P_y} - 1\right) + \left(\frac{q}{MP_y}\right)^2 = 0 \qquad (2\text{-}18)$$

Where $P_y$ is the hydrostatic yield stress and $M$ is a constant controlling the shape of the surface.

### 2.3.2.3 The Drucker-Prager Cap (DPC) model

The DPC plasticity model has been developed in the field of rock mechanics (Drucker and Prager, 1952). Recently, since it can describe shear failure, densification and hardening, the DPC model has been used to analyse powder compaction (Sinka et al., 2003, 2004a; Wu et al., 2005, 2008 , Han et al., 2008, Diarra et al., 2012, Mitra et al., 2016 and Zhou et al., 2017). The yield surface of the DPC model is shown in Figure 2-12. The yield surface includes shear failure surface $F_s$ and cap surface$F_c$. The shear failure surface is defined by two parameters (Abaqus, 2006): cohesion d and internal friction angle $\beta$

$$F_s = q - p\tan\beta - d = 0 \tag{2-19}$$

$\tan\beta$ and d can be determined from uniaxial and diametrical compression testing as illustrated in Figure 2-12:

$$d = \frac{\sigma_c\sigma_d(\sqrt{13}-2)}{\sigma_c-2\sigma_d}\ and\ \tan\beta = \frac{3(\sigma_c-d)}{\sigma_c} \tag{2-20}$$

where $\sigma_c$ is the uniaxial strength, which is calculated from the break force $F_u$ of uniaxial compression test and contact area of specimen. $\sigma_d$ is the tensile strength , which is calculated from the break force $F_d$ of the diametrical compression test and specimen size (thickness t and diameter D):

$$\sigma_c = \frac{4F_u}{\pi D^2}\ and\ \sigma_d = \frac{2F_d}{\pi Dt} \tag{2-21}$$

The cap surface is defined as (Abaqus, 2006):

$$F_c = \sqrt{(p-p_a)^2 + \frac{R^2q^2}{\left(1+\alpha-\frac{\alpha}{\cos\beta}\right)^2}} - R(d + p_a\tan\beta) = 0 \tag{2-22}$$

For a uniaxial cylindrical die compaction, the von-Mises effective stress q and the hydrostatic stress p are expressed as:

$$p = \frac{1}{3}(\sigma_z + 2\sigma_r) \tag{2-23}$$

$$q = |\sigma_z - \sigma_r| \tag{2-24}$$

Where $\sigma_z$ and $\sigma_r$ are the axial and radial stresses, R defines the shape of the “cap”, $p_a$ is a related parameter with the hydrostatic yield stress $p_b$ which is shown in

Figure 2-12.

$$p_a = \frac{p_b - Rd}{(1 + R\tan\beta)} \tag{2-25}$$

$\alpha$ is a parameter to describe the transition surface and is typically in the range 0.01~0.05 in order to have a smooth transition instead of a sharp corner between the shear failure line and cap surface (Hibbitt et al., 1998). The hydrostatic yield stress is related with a function of volumetric plastic strain $\varepsilon_v^p$:

$$p_b = f(\varepsilon_v^p) \tag{2-26}$$

The volumetric strain is given by:

$$\varepsilon_v^p = \ln\left(\frac{\rho_r}{\rho_{in}}\right) \tag{2-27}$$

Where $\rho_r$ is the current relative density, $\rho_{in}$ is the initial relative density of the particles. The relative density is defined as the ratio of the volume of particles in a unit to the total volume of the unit.

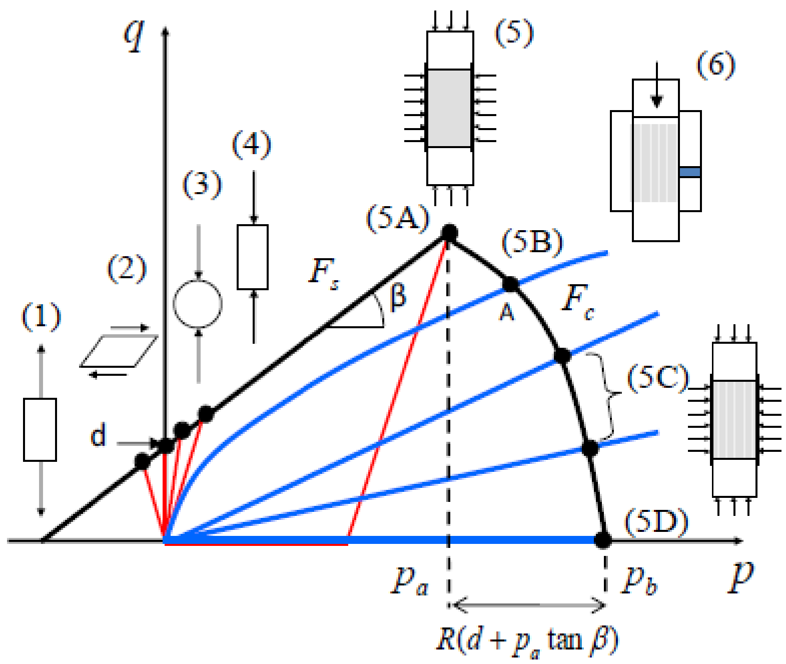


Figure 2-12 Drucker-Prager cap model and experimental procedures for determining the shear failure line using (1) uniaxial tension, (2) simple shear, (3) diametrical compression, (4) uniaxial compression; and the compaction surface using (5) triaxial testing: 5A consolidated triaxial test, 5B simulated closed-die compaction, 5C radial

loading in stress space, 5D isostatic test; (6) instrumented die compaction" (Shang, 2012).

#### 2.3.2.4 Fleck micromechanical model

Micromechanical models use the interaction between particles using contact laws to develop forms for macroscopic yield surfaces. Typically, the powder is considered as being formed of monosized spherical particles presenting elasto-plastic behaviour. A quadratic yield function for an early stage of compaction was developed by Fleck (1995):

$$F' = \left(\frac{\sqrt{5}p}{3P_y}\right)^2 + \left(\frac{5q}{18P_y} + \frac{2}{3}\right)^2 - 1 = 0 \qquad (2\text{-}28)$$

This model is only considered to be valid at low relative density where particles interact at isolated contacts.

#### 2.3.2.5 Deformation plasticity model

The deformation plasticity framework is based on the extremum theorems of Ponter and Martin (1972). This formalism evaluates the response of a random array of spherical particles under similar assumptions as Fleck and co-workers (Fleck, 1995; Fleck et al., 1997; Storakers et al., 1999). For the plastic response of polycrystalline materials theoretical models predict that the yield surface of complex evolving shapes has a vertex at the loading point (Asaro, 1983), and this has been confirmed by experiments (Phillips and Lu, 1984). However, simple macroscopic models, which include a smooth yield surfaces, can also provide an accurate description of the material response. The complexity is due to the form of laws which used to describe the translation and expansion of the surface in stress space (Mroz, 1967; Chaboche, 1993).

It is usually accepted that the incremental theories whereby the strain increment is defined when the stress reaches yield are more physically reasonable than the deformation theories. Here, the total strain is related to the current stress without considering history effects. Moreover, a deformation theory only gives an accurate description of the response for a single loading history if the true yield surface is smooth (Ponter and Martin, 1972). However, the deformation theory can provide a good description of the material response for a wide range of monotonically raising stress histories if the true yield surface includes vertices (Budiansky, 1959). Furthermore, when the true yield surface contains vertices, the deformation theory offers a more accurate description of the post-buckling response of structures than the conventional incremental theory (Hutchinson, 1974), because the direction of the strain-increment vector at a vertex is not unique in the incremental models. For example, if the stress is raised along a radial loading path in stress space, a peak form at the loading point as the stress is increased. If the element is then subject to a small added non-radial stress increment to keep the loading point at the vertex, rapid change is accompanied in the direction of the strain increment vector. However, the total strain is similar to that acquired from a radial loading history from the initial to terminal state (Cocks and Sinka, 2006).

The extremum theorems of Ponter and Martin (Ponter and Martin, 1972) are significant to the development of the deformation plasticity model. Consider an element of material is subjected to a history of loading to a strain $\varepsilon_{ij}$. The work done during this loading history is:

$$\omega(\varepsilon_{ij}) = \int_0^{\varepsilon_{ij}} \sigma_{ij} d\varepsilon_{ij} \tag{2-29}$$

In strain space, there exists a path for which the work done is a minimum, i.e.

$$\omega_e(\varepsilon_{ij}) \leq \omega(\varepsilon_{ij}) \tag{2-30}$$

$\omega(\varepsilon_{ij})$ is the work done along this extremal path. If the final stress $\sigma_{ij}$ is reached along any other path in strain space, then

$$\sigma_{ij} = \frac{\partial \omega_e}{\partial \varepsilon_{ij}} \tag{2-31}$$

Similarly, the complementary work done along any path in stress space to a terminal state $\sigma_{ij}$ is:

$$\overline{\omega} = \int_0^{\sigma_{ij}} \varepsilon_{ij}\, d\sigma_{ij} \tag{2-32}$$

In stress space, a path exists so that $\overline{\omega}$ is a maximum, i.e.

$$\overline{\omega_e}(\sigma_{ij}) \geq \overline{\omega}(\sigma_{ij}) \tag{2-33}$$

The resulting strain, $\varepsilon_{ij}$, is given by

$$\varepsilon_{ij} = \frac{\partial \overline{\omega}_e}{\partial \sigma_{ij}} \tag{2-34}$$

It can be noted that there is an equivalent extremal path for $\overline{\omega}$ in stress space for any extremal path for ω in strain space and

$$\omega_e(\varepsilon_{ij}) + \overline{\omega}_e(\sigma_{ij}) = \sigma_{ij}\varepsilon_{ij} \tag{2-35}$$

A stable hyperelastic material that is less stiff than the inelastic material used to define it is effectively defined by the extremal paths in Equations (2-31) and (2-34), which thus gives a consistent set of relationships for the definition of a deformation theory. The use of these relationships requires a consistent definition of stress and strain. The conventional incremental plasticity models describe the material behaviour using the true (Cauchy) stress and increments of true strain which is the symmetric part of the deformation increment tensor. The minimum work path of a given deformation history can be resolved into a pure rotation followed by straining so that the relative magnitude of the true train increments kept constant. This deformation can be described in terms of the principal components of the true strain, $\varepsilon_{\mathrm{I}}, \varepsilon_{\mathrm{II}}, \varepsilon_{\mathrm{III}}$, or the principal equivalently stretches, $\lambda_i = exp\varepsilon_i, i = \mathrm{I}\ to\ \mathrm{III}$. Therefore the potential $\omega_e$ can be presented as a function of either the true strain or principal stretches.

The above theoretical results will be used to develop a model for the deformation response of powder compacts. General relationship for the macroscopic response will be derived, and then this structure will be applied to the micromechanical model of Fleck et al. (Fleck, 1995; Fleck et al., 1997; Storalers et al., 1999) to gain a specific form of constitutive model (Cocks and Sinka, 2006).

2.3.2.5.1 Structure of constitutive laws

Figure 2-13 shows a macroscopic element of material which includes a random array of contacting particles that form an equilibrium structure. The initial volume is taken as a reference state. The applied loading to the particles can be expressed in terms of the macroscopic average true stresses, $\Sigma_{ij}$, and Hencky logarithmic strains $E_{ij}$. To simplify, it can be assumed that the initial volume is unity and at a given instant $V = J$, the ratio of volumes in the deformed and reference configurations. For the material which deforms according to the deformation model of equation (2-34)

$$J\Sigma_{ij}dE_{ij} = T_{ij}dE_{ij} = \int_{V_s} \sigma_{ij}d\varepsilon_{ij}$$

$$= \int_{V_s} d\omega_e(\varepsilon_{ij})dV = d\Omega_e \quad \text{(2-36)}$$

where $T_{ij} = J\Sigma_{ij}$ is the Kirchoff stress, $V_s$ is the solid volume and $\Omega_e$ is given by

$$\Omega_e = \Omega_e(E_{ij}) = \int_V \omega_e(\varepsilon_{ij}^e)dV \quad \text{(2-37)}$$

And is a function of the macroscopic strain $E_{ij}$. Equation (2-36) indicates that

$$T_{ij} = \frac{\partial\Omega_e}{\partial E_{ij}} \quad \text{(2-38)}$$

A dual potential $\bar{\Omega}_e$ can also be defined so that

$$E_{ij} = \frac{\partial\bar{\Omega}_e}{\partial T_{ij}} \quad \text{(2-39)}$$

The two potentials are related to each other similar to Equation (2-35)

$$\Omega_e(E_{ij}) + \bar{\Omega}_e(T_{ij}) = T_{ij}E_{ij} \quad \text{(2-40)}$$

Also, the corresponding results to those of Equation (2-30) and (2-31) work for the macroscopic porous body are illustrated by Ponter and Martin (1972), which is shown as

$$\Omega_e(E_{ij}) \leq \Omega(E_{ij}) \text{ and } \bar{\Omega}_e(T_{ij}) \geq \bar{\Omega}(T_{ij}) \quad \text{(2-41)}$$

Where $\Omega(E_{ij})$ and $\bar{\Omega}(T_{ij})$ are the work and complimentary work done per unit initial volume along the loading path to the strain $E_{ij}$ and stress $T_{ij}$.

These results show a general structure of a deformation plasticity model for a powder compact that can be used to offer a theoretical structure for the explanation of the results and direct an experimental analysis programme. The equation (2-41) proposes that the loading path should be determined in which the complementary work per unit initial volume is maximised. The analysis results for loading paths should be plotted as surfaces of constant complementary work in Kirchhoff stress space. It should be checked that the total strain vector is normal to these surfaces as describe by equation (2-39), and the sensitivity of the complementary work to choice of loading path should be evaluated. For the situation where the macroscopic yield surfaces involve vertices, it would be expected that $\bar{\Omega}(T_{ij})$ is insensitive to the choice of loading path.

In this section, the structure of constitutive model is related to a wide range of inelastic materials. The bounding character of the deformation plasticity model requires the underlying incremental response to be stable where dissipation by frictional sliding between particles is considered. Based on above framework, a micromechanical model of powder compaction is developed by Cocks and Sinka (2006). The model offers description of the surfaces of constant complementary work that can be used to analyse MPFEM results in the following Chapters.

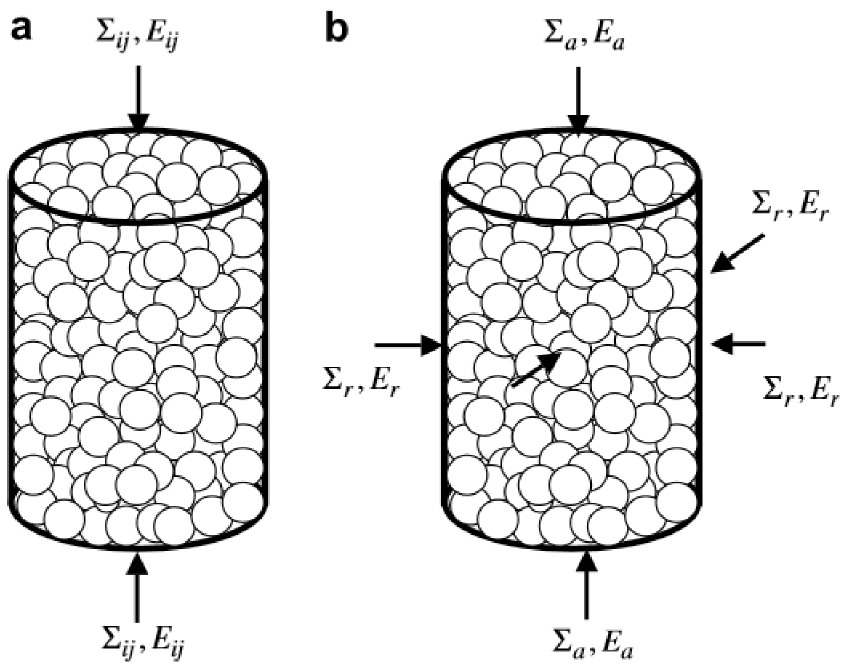


Figure 2-13 (a) a unit cell of powder compact consisting of a random packing arrangement of realistic irregular particles subjected to macroscopic stresses $\Sigma_{ij}$and strains $E_{ij}$. (b) The element of material shown in (a) controlled by an axisymmetric stress and strain history (Cocks and Sinka, 2006)

## 2.3.3 Overview of FEA

FEA is a numerical solution for solving the elasticity and plasticity problems. In the early 1950s (Turner et al., 1956), it was firstly used in the field of continuous physical research, including aircraft static and dynamic structural analysis to obtain the structural deformation, stress, natural frequency and mode shape. The validity of this approach means the application of FEA extends from linear to nonlinear problems. The analysis of the object extends from elastic material to the plastic, viscoelastic, viscoplastic and composite materials, and from a continuous body to a non-continuous body.

In FEA a large structure is divided into finite areas called elements and nodes. The assumption is that the deformation of the structure is simple in each element. The deformation and stress of each element and that of the entire structure are determined. It has been theoretically proved that, when the number of elements are large enough, the finite element solution converges to the exact solution of the problem (Strang and George, 1973; Hasting et al., 1985; Reddy, 2006). But the calculation quantity increases accordingly. To this end, it is necessary to find the balance between computational requirements and calculation accuracy.

In powder engineering, FEA can be used to optimise the formulation of powder and improve a product performance criterion by the selection of process parameters. This method is used for all classes of powders.

### 2.3.4 Multi-particle finite element method (MPFEM)

MPFEM for powder compaction involves considering each particle individually. As a result of combining discrete behaviour of particle assemblies, MPFEM has the ability to account for large contact deformation and up to a high relative density which cannot be achieved in DEM. A "unit cell" is used to define a representative arrangement of particles. In the unit cell, each particle is meshed individually. The assembly is compacted by rigid wall boundaries. This approach has been implemented by different researchers (Akisanya et al., 1994, Ransing et al., 2000, Wu et al., 2000 and Huang et al., 2017). However, these simulations are limited to an ordered particle packing or monosized spherical particles. Procopio and Zavaliangos (2005) improved this by creating a model which simulated a large amount of random packing particles, without simplified assumptions regarding contact mechanics. Although the MPFEM gives an excellent platform to determine and examine issues with respect to particle shape, size and material properties, they studied monosized, elastic-perfectly plastic, circular particles with goal of establishing the accuracy of this method and to investigate the effect of basic factors. They aimed to understand the development of the yield surface during monotonic loading to a given density.

To set-up MPFEM, the optimal selection of the finite element mesh was investigated (Procopio and Zavaliangos 2005). If the outer surface of the particle is adequately discretized, FEA can describe the interparticle interactions with little geometric compromise. As shown in Figure 2-14a, there are 72 structured nodes on the particle surface with 169 total nodes and 132 total elements per particle. The smallest length scale is the external surface elements which are accurately defined as 3.75% of the particle diameter. The accuracy of this designed mesh has been verified with comparing against a 2700 element mesh which is illustrated in Figure 2-14b. This 2700 element mesh is elastic-perfectly plastic particles with a ratio of Young's modulus to yield stress of E/$\sigma_y$=100 and a Poisson ratio of $v = 0.3$ in various configurations (Figure 2-14c) under central motion of their centres. The result shown in Figure 2-14c determined that the proposed mesh has excellent accuracy and is very economical with regard to the degrees of freedom. This structured particle mesh saves simulation time.

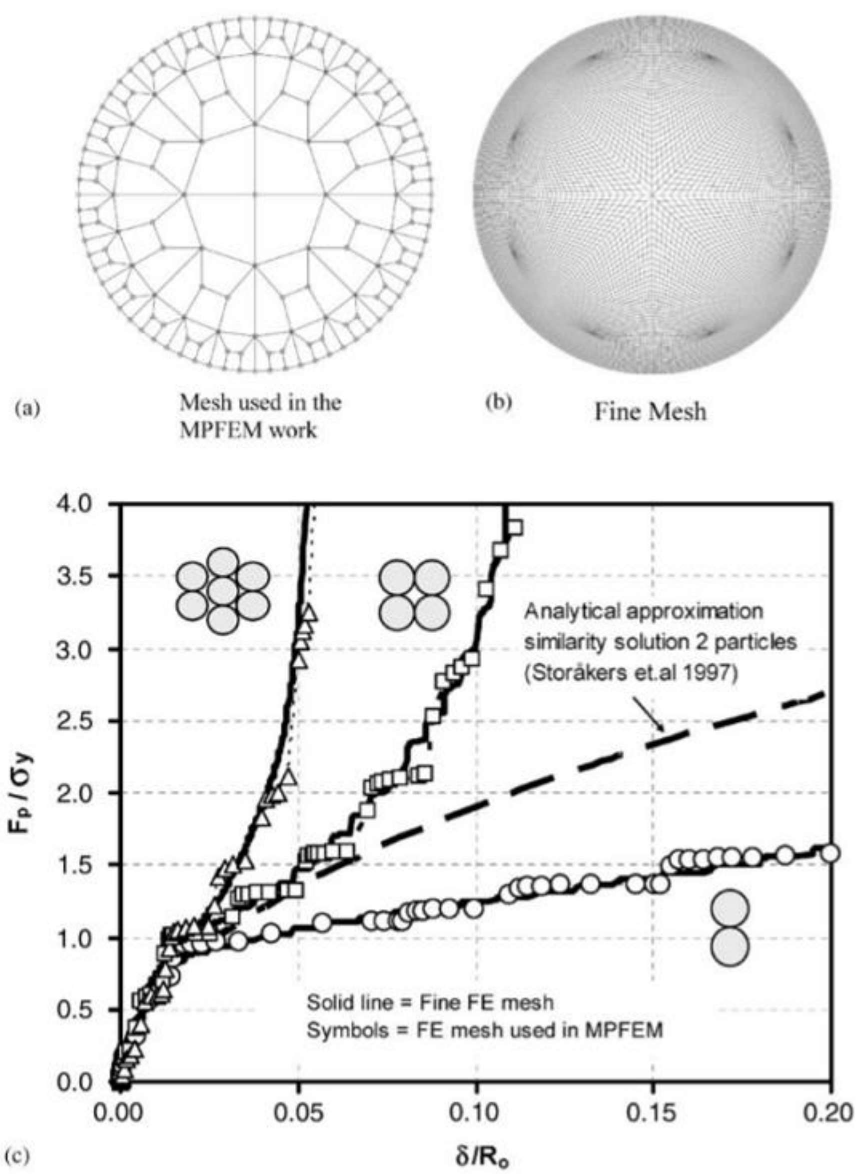


Figure 2-14 Normalized interparticle force (c) as a function of interparticle strain for a simplified quarter cylinder under normal loading, simple cubic loading and hexagonal loading for (a) designed structured mesh used in the MPFEM (Procopio and Zavaliangos, 2005) and (b) fine finite element mesh overlaid with the similarity solution of Storakers et al. (1997)

For the initial particle configuration, a low density random packing of particles was created in a rectangular box. The particle collection was densified by applying position dependent initial velocities to the particle which are zero at the centre of the rectangle and increase linearly with radial distance. To ensure the particle motion, a full finite element simulation was carried out with the additional constraint of moving rigid boundaries that envelop the motion of the particles. During particle compaction, the simulation time is accelerated by using mass scaling which increases inertia and the maximum stable time increments. The boundary condition of this model uses moving rigid surfaces to apply displacement. Simulations were performed by varying symmetrically the prescribed motion of the radial (r) and axial (a) rigid boundaries velocities to maintain a specified ratio E/H, where H and E are the hydrostatic strain and equivalent strain in the 2D plane, respectively defined as

$$H = (E_a + E_r) \; and \; E_e = \frac{1}{2}(E_a - E_r) \tag{2-54}$$

The macroscopic stress is calculated from the reaction forces of the moving rigid boundaries and is described using the following measures of the stress:

$$\Sigma_m = \frac{1}{2}(\Sigma_a + \Sigma_r) \; and \; \Sigma = (\Sigma_a - \Sigma_r) \tag{2-55}$$

where $\Sigma_m$ is the hydrostatic component and $\Sigma$ is the deviatoric stress response.

For material properties, Procopio and Zavaliangos (2005) assumed that the particles are linear elastic-perfectly plastic with $E/\sigma_y$ of 100 and Poisson's ratio of 0.3, where $E$ is the Young's modulus and $\sigma_y$ is the uniaxial yield stress. They pointed out that the selection of $E/\sigma_y$ is important for both accuracy and computational efficiency of this model. Mesarovic and Fleck (2000) showed that the effect of elasticity occurs at $E/\sigma_y < 500$, but it remains small up to $E/\sigma_y$ of 100.

The interaction between wall and particles is considered frictionless. The Coulomb interaction with an upper limit of the shear stress, $\tau_{max} = \tau_y = \sigma_y/\sqrt{3}$ and friction coefficient between particles $\mu = 0, 0.1, 0.192\ and\ 0.3$ were studied. The specific value of $\mu = 0.192$ is based on the ratio of the upper limit yield stress shown above and the maximum contact pressure which is given by the Prandtl solution for the indentation of a semi-infinite medium by a flat die (Hill, 1950), $p = 2.97\sigma_y$.

Figure 2-15 shows a comparison of the MPFEM for isostatic compaction with $\mu = 0.192$ with:

1. There is a plasticity solution to the problem of a cylinder controlled by external pressure where the bore radius is chosen to express the porosity (Torre, 1948),

$$p = \frac{-\sigma_y}{\sqrt{3}} \ln(1 - D) \tag{2-56}$$

2. The Helle solution (Helle et al., 1985) for the limiting external pressure which will cause yielding of a particle based on simplified equations of coordination number and geometry,

$$p = 3D^2 \frac{(D - D_0)}{(1 - D_0)} \sigma_y \tag{2-57}$$

3. 2D Gurson model, modified as

$$p = \frac{-\sigma_y}{\sqrt{3}} \cosh^{-1}\left[\frac{1 + (1 - D)^2}{2q_2(1 - D)}\right] \tag{2-58}$$

   where $q_2 = 1.5$ based in comparison to numerical results to account for localization effects (Tvergaard, 1990)

4. The unit cell FEM of periodic hexagonal packing arrangement of discs (PHAD) for two material property combinations: $E/\sigma_y = 100{,}1000$

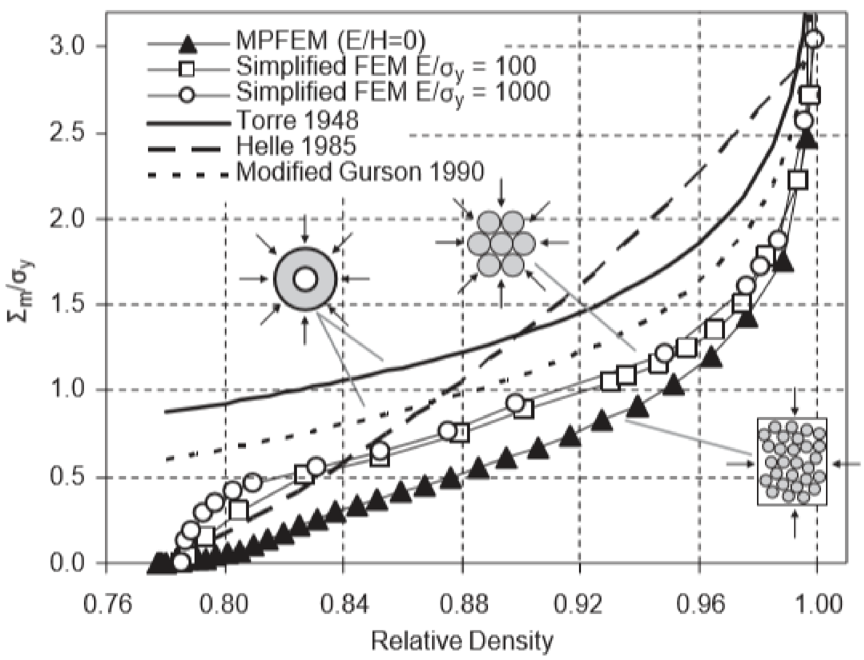


Figure 2-15 Comparison of predicted mean stress against relative density for isostatic pressing (E/H=0) for 2D Torre model, the Helle solution, the modified Gurson model, two periodic hexagonal FEM simulation for E/σ_y=100,1000 and MPFEM simulation (Procopio and Zavaliangos, 2005)

The results show that the Torre and the modified Gurson model overestimate the prediction of the periodic arrangement for all relative densities. They are often claimed to be suitable for the last stage of compaction. This large difference can be due to geometric effects. In their case, it is a cylinder with a hole that is compressed by external pressure. Yielding occurs everywhere along the periphery of the inner hole. However, for the particle level compaction, the yielding on the particle contact is given on a smaller area. For the finite element solution of the PHAD, the effect of elasticity does not indicate a main role in the stress response for $E/\sigma_y = 100\ and\ 1000$. Compared with the PHAD, MPFEM shows a lower stress response owing to the accomplished densification by particle rearrangement and non-affine motion apart from the plastic yielding at the particle contacts. In Figure 2-15, only MPFEM includes particle rearrangement and non-affine motion.

Procopio and Zavaliangos (2005) also compared the hydrostatic compaction solution between the MPFEM and the Fleck and Redanz (2001) 2D DEM model which is shown in Figure 2-16 (a)-(c) for low relative densities. The DEM solution relaxed the assumption of affine particle motion and predicted a reduced stress response due to the ability for the particles to rearrange. But its resolution still shows a higher densification stresses than the MPFEM. Storakers et al. (1997) explained one reason for this difference. The solution in their DEM work has a narrow range of application as shown in Figure 2-14 (c). In addition, the lateral motion of contacting particles on the centre-to-centre line does not change the level of interparticle force despite the potential change in contacting area between particles. In a real situation, the relative movement of the contacting particle may cause the contact area to shift from the previous deformed material toward neighbouring material, where there are undeformed areas on the surface of the particles, which in turn significantly reduces the interpaticle forces. However, such phenomena is captured naturally by the MPFEM, which is capable of following interparticle contacts with no compromises in the geometry assumption.

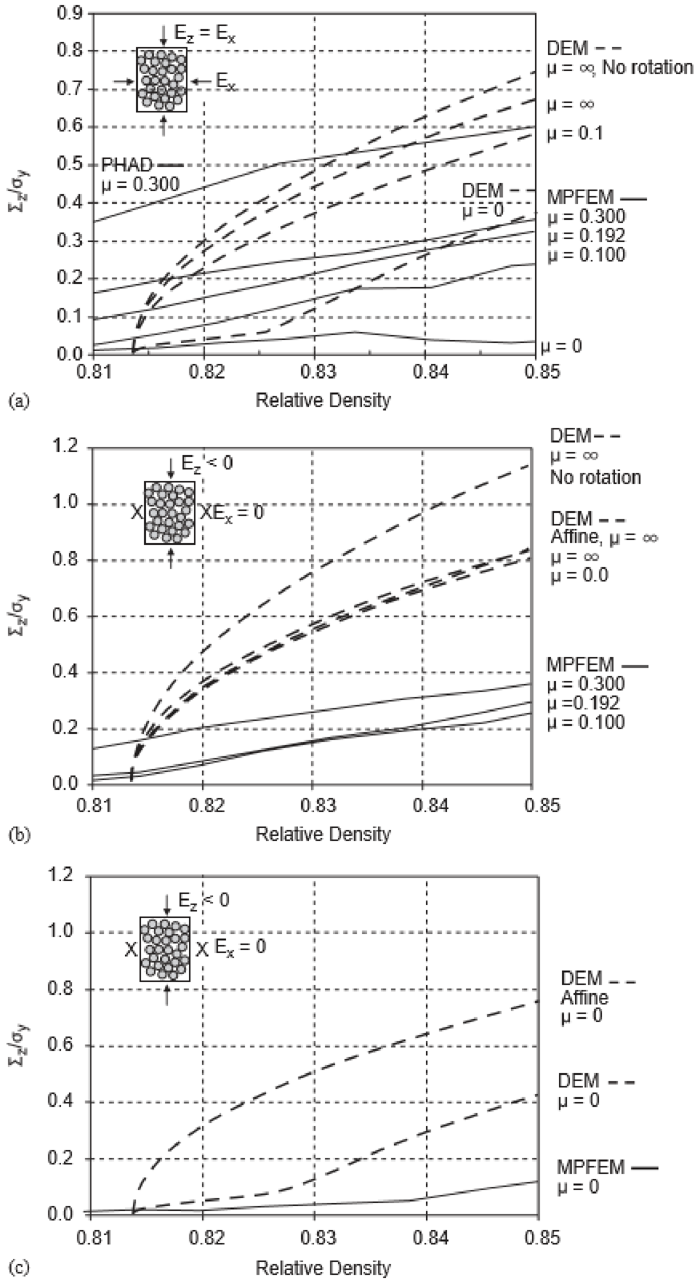


Figure 2-16 Comparison of the hydrostatic compaction solution between MPFEM (Procopio and Zavaliangos, 2005) and 2D DEM solution (Redanz and Fleck, 2001)

Although, the DEM can successfully handle large numbers of particles, the application of DEM has limits regarding the deformation behaviour at particle contact level. The MPFEM can provide necessary degrees of freedom that allow a local natural contact deformation rather than a uniform deformation in DEM. As a result, the MPFEM can address rearrangement, non-affine motion, particle rotation and large deformation to high relative densities. The MPFEM offers unprecedented insight in the compaction behaviour of particles. Therefore, further examination of important effects such as particle shape and material behaviour, which are practically impossible to examine by DEM or other micromechanical models, needs to be explored.

## 2.4 Research objectives

The overall objective of this research is to develop a complete methodology for determining the constitutive law for the compaction behaviour of a powder material using particle properties and packing arrangements without the need to carry out compaction experiments on bulk powders. This is achieved through the following specific objectives:

1. Characterisation of the mechanical properties of particles in order to describe elastic and plastic behaviour

2. Characterisation of particle size, shapes and packing arrangements and set-up of a representative cell for FEA

3. Numerical calculation (using MPFEM) of stress-strain curves for the unit cell subject to a variety of loading paths in strain space

4. Validation of the multi-particle model against data generated closed die compaction experiments

5. Development of constitutive laws for compaction using the deformation and incremental plasticity framework

The framework of research structure is shown in Figure 2-17. There are two steps involved in setting up MPFEM. First, characterisation of single particle properties as input parameters for MPFEM. These properties (e.g. Young's modulus, Poisson's ratio and yield stress) are calculated based on Hertz law using the break force and displacement which are obtained from single particle breakage test. To validate these input parameters, a single particle compression model is created. Second, the actual particle size, shape and packing arrangement are captured from X-ray CT system. Through an image analysis process, the multi-particle geometry is defined and transferred into finite element software. Coupled with the particle characteristics, the constitutive model will be simulated using MPFEM. The model needs to be validated by involving the experimental data from instrumented die compaction. Then the deformation plasticity framework will be applied to develop the constitutive law.

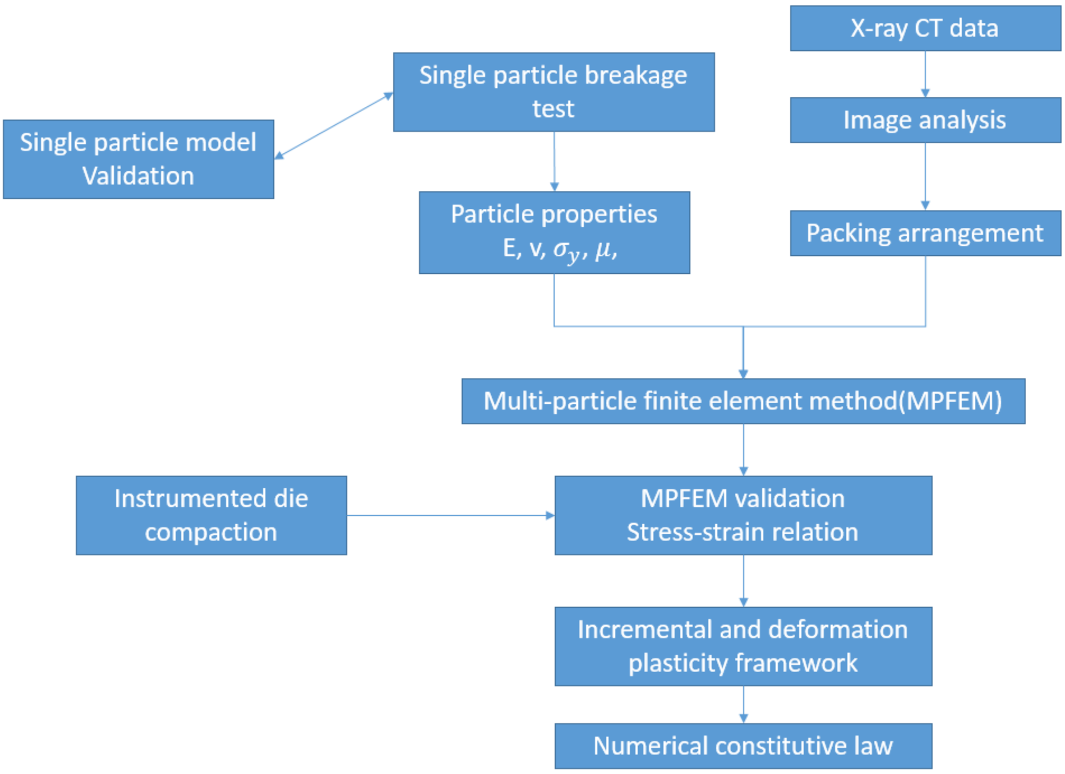


Figure 2-17 The framework of research structure

# Chapter 3. Experimental characterisation of mechanical properties of single particles and modelling single particle deformation

The development of numerical constitutive laws using the multi-particle finite element method requires the mechanical properties of single particles as inputs. In this chapter, the experimental methodology used to measure physical and mechanical properties (density, elastic modulus and yield stress) are presented. For practical purpose, it is important to determine in a clear and efficient manner. Table 3-1 summarises the procedures for determining compaction the mechanical properties of the particles.

Table 3-1 Methodology for determining single particle properties

| Parameter | Description | Procedure |
|---|---|---|
| Elastic Behaviour | | |
| E, Gpa | Young's modulus | Single particle elastic test (Section 3.2.1) |
| V, | Poisson's ratio | |
| Plastic behaviour | | |
| $\sigma_y$, MPa | Yield stress | Single particle breakage test (Section 3.2.2) |

## 3.1 Material

In this research a relatively large compressible granule is used as the specimen to carry out the elastic and breakage test. The size of the granule (approximately 0.8 mm diameter) was selected in order to facilitate high quality X-ray CT images.

Granules made of microcrystalline cellulose were prepared using the extrusion/spheronization process. Microcrystalline cellulose is a fine powder which is widely used as excipient in pharmaceutical and other industries. It is purified, partially depolymerized cellulose prepared using mineral acid to hydrolyze cellulose pulp and obtain a natural cellulose in free flowing powder form which is insoluble in water and forms a stable dispersion. Because of the existence of hydrogen bonds between the microcrystalline cellulose molecules, the powder is highly compressible. It has material characteristics for wet granulation processes and extrusion/spheronisation.

Spheronization is widely employed in food and pharmaceuticals (Shyamala and Lakshmi, 2010). The basic machine includes a rotating disk at the base of a fixed cylindrical bowl. The disc is termed “friction plate” and has a groove pattern on the processing surface to engage with the material. Extrudates are loaded into the spheronizer and the process can be divided into a number of stages. Firstly, the cylindrical extrudate segments are broken into segments with a length ranging from 1 to 1.2 times the diameter (Caleva Process Solution Ltd., 2016). Then the segments collide with the bowl wall and the friction plate. The ongoing action of segments colliding with the vessel creates a rope-like movement of particles. The continuous collision and friction of particles gradually reshape the cylindrical segments into spheres. When these particles have obtained the required particle shape and size, the discharge valve of the chamber is opened and the particles are discharged by the centrifugal force (Caleva Process Solution Ltd., 2016).

The starting material for spheronisation is Microcrystalline Cellulose Avicel PH101 manufactured by FMC Biopolymer. The density of the fully dense material is measured is 1480 kg/m$^3$ by calculating average mass and volume.

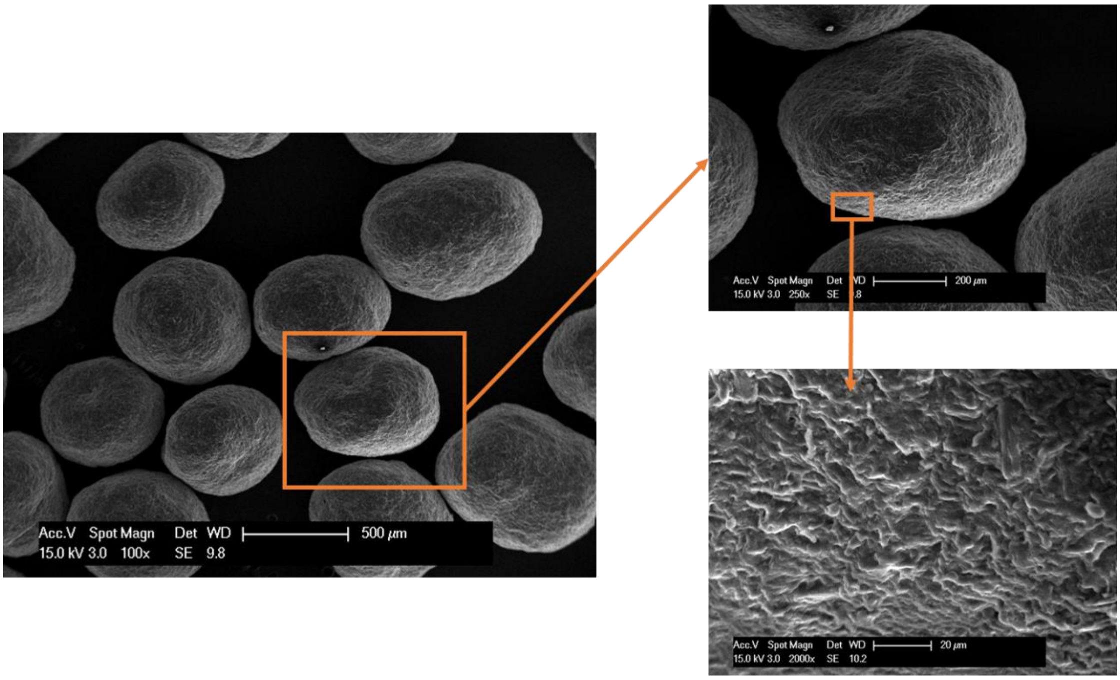


Figure 3-1 SEM micrograph of microcrystalline cellulose particle used in this study

## 3.2 Characterisation of single particle mechanical properties

The mechanical strength of a compact is strongly dependent on the mechanical properties of the individual particles and the interactions between particles. Therefore, it is important to characterise the deformation and compression behaviour of single particles. Young's modulus and yield stress are the two main material properties that affect the compaction behaviour of powders.

## 3.2.1 Elastic test

This elastic compression of single particle is conducted using a machine for micromechanical fatigue test (MMT-11N Shimadzu Co., Japan). As shown in Figure 3-2, the system includes voltage regulator, UPS power supply, controller, signal amplifier, stretching mechanism and computer.

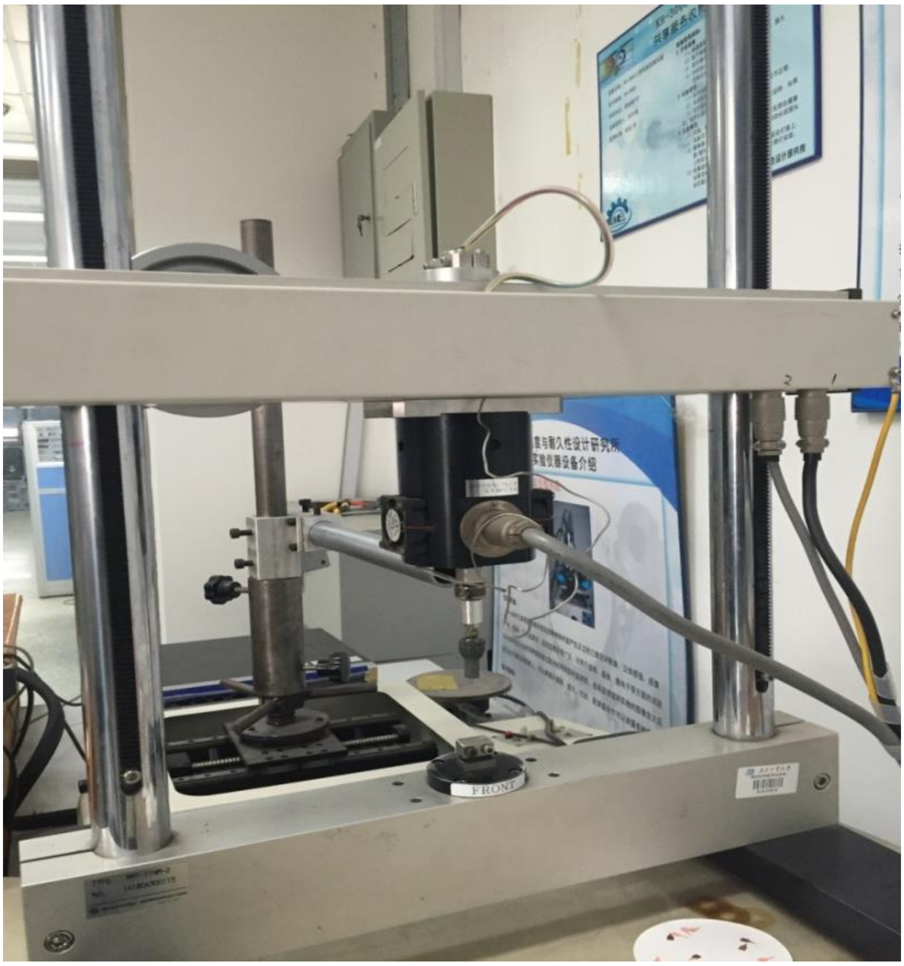


a) Tensile agencies

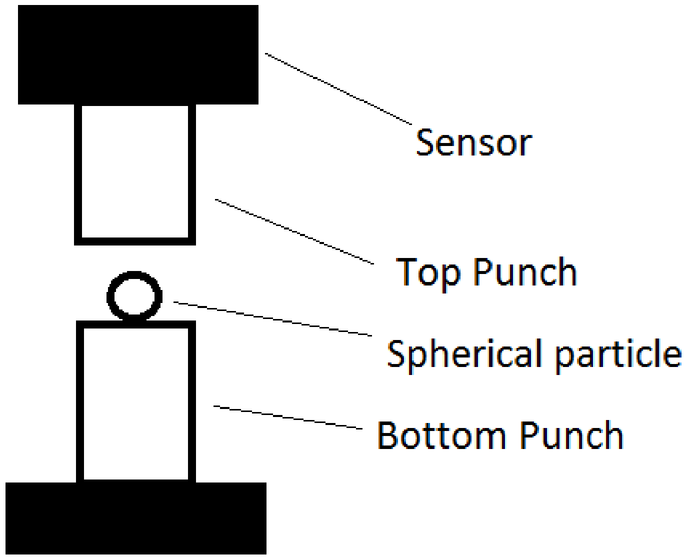


b) Schematic diagram

Figure 3-2 MMT-11 micro-fatigue testing of single particles

The main features of this fatigue machine involves small energy consumption, low noise, simple operation. It uses the advanced two-degree-of-freedom PID adaptive control mode that has automatic adjustment of control parameters. The system setting, control and data collection can be done using corresponding test software in PC. The controller contains a 20-bit high-precision A/D converter to achieve real-time accurate measurement.

MMT-11N has a high frequency response of the electromagnetic vibrator as a loading mechanism. Through the closed-loop control, it can be controlled and measured under small force and displacement with high speed and precision. The loading range is ± 10N, the frequency is from 1 to 60 Hz and the displacement range is ± 2mm.

This compression test is carried out at room temperature using load control. As the sine wave expression is simple, it is selected as waveform to apply cycle load, and the loading frequency is 1, 5, 10Hz which means there are 1, 5, 10 cycles tested per second. The maximum loading force starts to record from 7N to 9N, and there are 90 cycles output in every 0.5N increment.

In elastic compression test, the cyclic loading is applied until the set value is reached. These tests under different frequency (1, 5, 10Hz) are finished with a big agreement. The results are shown in figure 3-3.

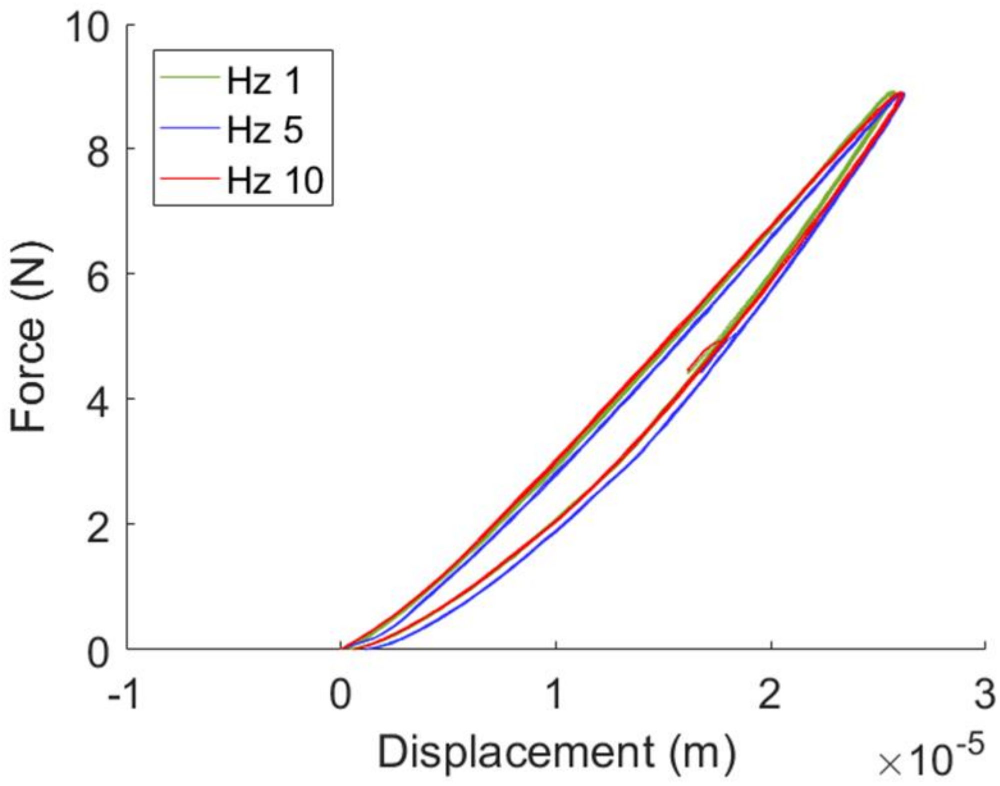


Figure 3-3 Elastic compression test

In order to determine the properties of single particles the solution of the problem of a single elastic sphere of Hertz is used, which represents a relationship between normal force and displacement of the centres of two spheres undergoing deformation at the contacts. The assumptions used in the Hertz model are: (1) the contact bodies are homogeneous, isotropic and the material is linear elastic; (2) the applied load is static; (3) the diameters of the particles are much larger than the dimension of contact surface; (4) the contact surface is smooth without friction effects; (5) the deformation of the bodies is small.

According to Hertz theory, when a particle is loaded by a normal force $\mathrm{N}$, the particle will undergo a local contact surface deformation. The pressure $P_c$ on the contact surface is:

$$P_c = \mathrm{p_0}\{1 - (\mathrm{r}^2/\mathrm{a}^2)\}^{1/2} \tag{3-1}$$

Where r is the radial distance from the centre of the contact surface, a is the surface of contact and $\mathrm{p_0}$ is the maximum pressure of the contact surface. The surface of contact a is given by:

$$\mathrm{a} = \left(\frac{3\mathrm{NR}}{4\mathrm{K}}\right)^{1/3} \tag{3-2}$$

Where R is the radius of the particle and K is the bulk modulus and a constant represented the elastic properties of the particle. It can be calculated from Young's modulus E and Poisson's ratio $\nu$ :

$$\frac{1}{\mathrm{K}} = \frac{1-\nu^2}{\mathrm{E}} \tag{3-3}$$

The total normal displacement $\delta$ is given by:

$$\delta = \left(\frac{9\mathrm{N}^2}{16\mathrm{RK}^2}\right)^{1/3} \tag{3-4}$$

Based on the result of elastic test, Young's modulus is fitted using equation (3-4). In this experiment, the unloading curve shows the elastic behaviour of the single particle. As shown in figure 3-4, the unloading curves represent a better trends match.

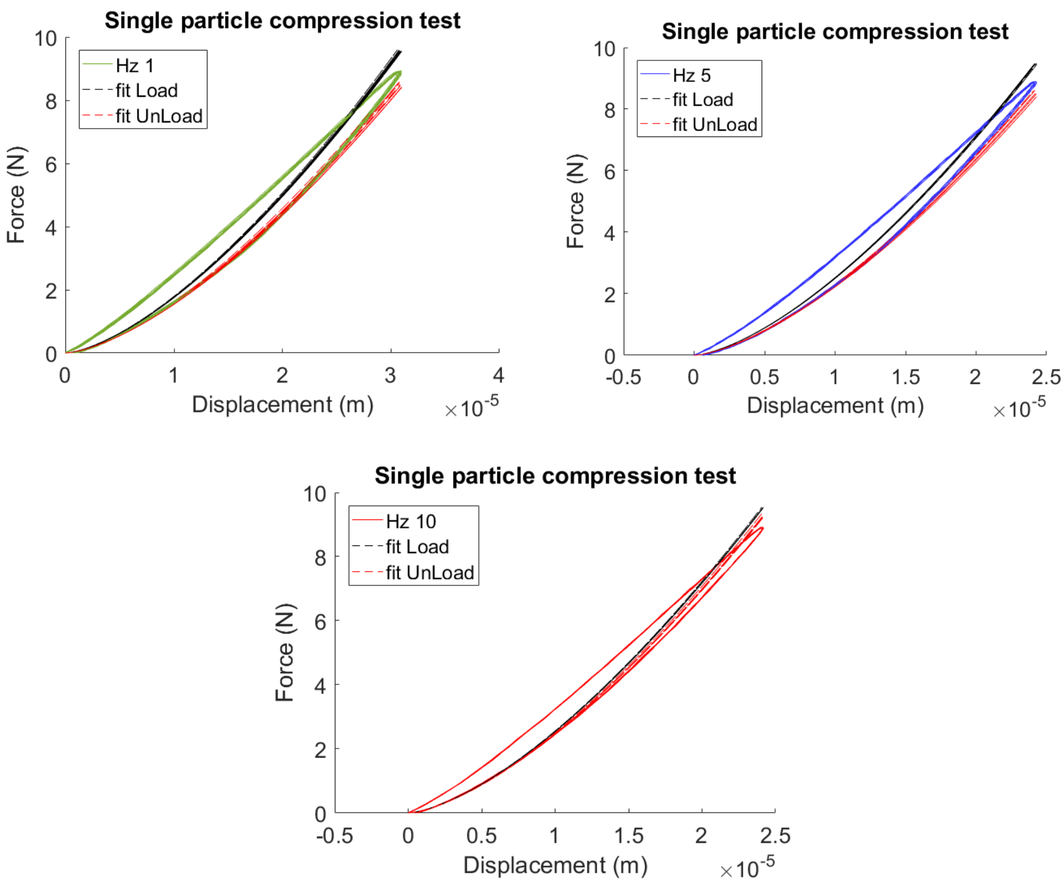


Figure 3-4 Fitting curves in 1, 5, 10Hz

### 3.2.2 Breakage test

The granule breakage test is carried out using an "Instron 2716-016" compression/tension machine manufactured by Instron UK that is suitable for small specimen testing. The machine has a rated capacity of 1kN; for granule breakage a 500N load cell was used. The system is illustrated in Figure 3-5.

The particle is compressed using two cylindrical punches which have 12 mm diameter. The bottom punch is fixed. The movement of the top punch is controlled using displacement as feed-back. A relatively low rate of 1 mm/min is applied to capture the deformation and breakage of a relatively small particle (0.8mm).

The elastic compliance of the two punches and the compression system was determined and correction procedures for the elastic compliance of the system (detailed in Chapter 4) were applied to the measured force-displacement curves.

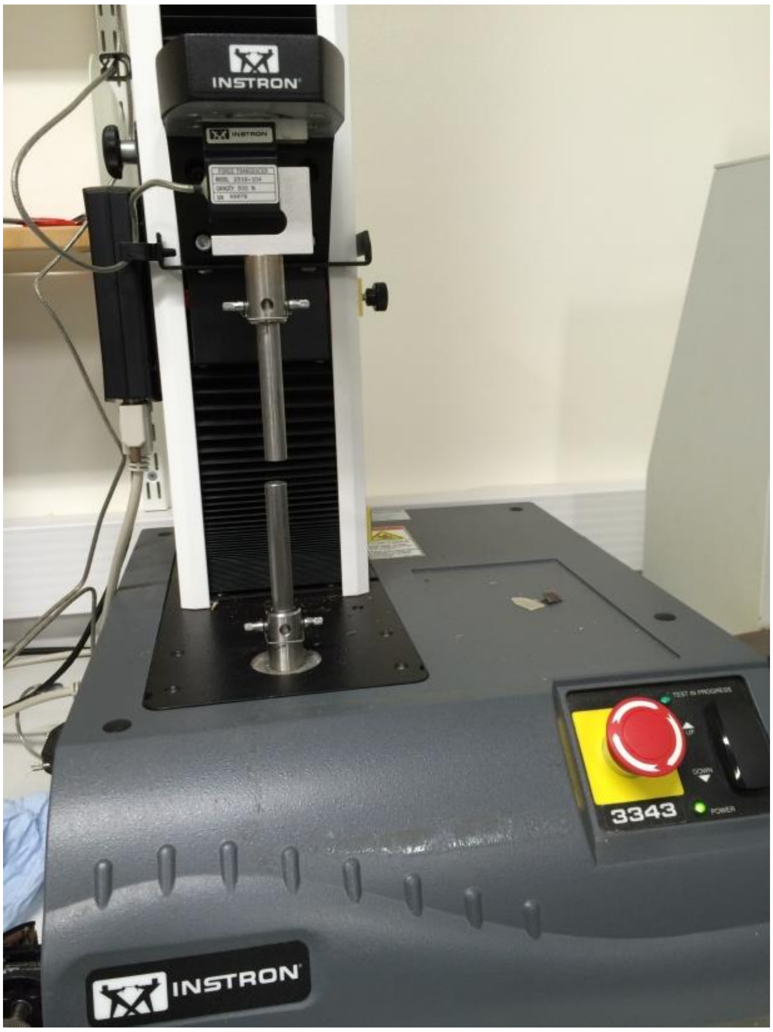


Figure 3-5 Instron system for single particle breakage

In a typical breakage test, the force increases with displacement until a peak value is reached, where brittle failure is observed and a crack is developed through the centre of the particle. For the purpose of data analysis, the break force is defined as the maximum force value which is followed by the 20% drop. With further compression, the force increases as the fragments are broken up. The results are shown in Figure 3-6.

In summary, the granule having diameters of 0.8 mm were compressed between rigid platens and the average break force was found at to 12 N and the applied displacement is 0.09mm.

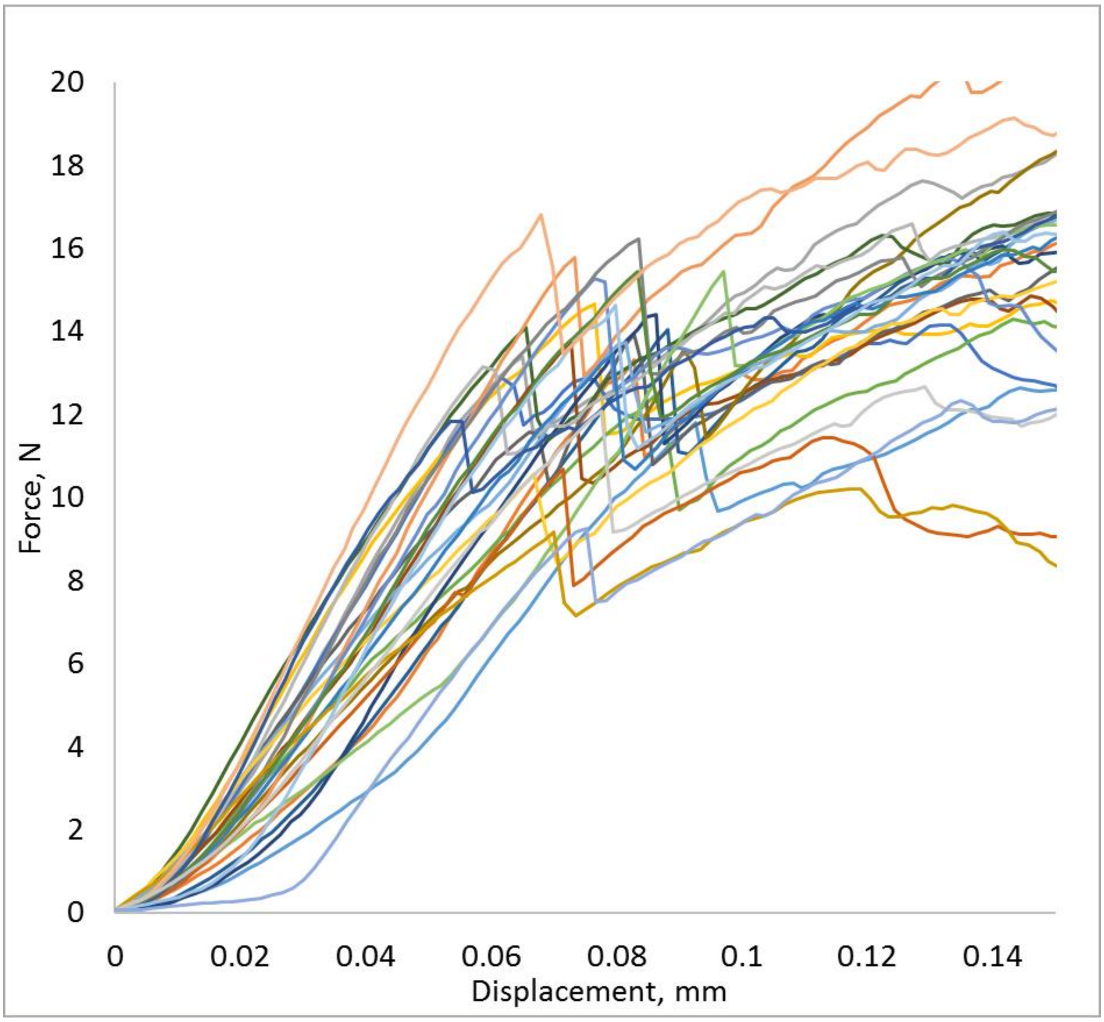


Figure 3-6 Force-displacement curves single particle compression test

The value of the maximum pressure $p_0$ is obtained by equating the sum of the pressure over the contact area to the compression force N. Then, the maximum pressure can be given by

$$p_0 = \frac{3N}{2\pi a^2} \quad (3\text{-}5)$$

The maximum pressure is 1.5 times the average pressure on the surface of contact. In this case, the failure of single particle is produced by maximum tensile stress. This stress occurs at the circular boundary of the surface of contact (Johnson, 1985). It acts in radial direction which can gives

$$\sigma_y = \frac{p_0(1-2v)}{3} \tag{3-6}$$

Where $\sigma_y$ is the yield stress which will be used as an input parameter in FEA of single particle and MPFEM.

The mechanical properties determined from single particle compression are presented in Table 3-2

Table 3-2

| | |
|---|---|
| Radius, (mm) | 0.45±0.003 |
| Young's modulus, (GPa) | 1.5 |
| Poisson's ratio | 0.35 |
| Yield stress, (MPa) | 45 |

## 3.3 FEA of single particle compression

FEM of single particle compression is carried out and validated against the experiments. The commercial finite element package

To represent the FEM, Abaqus is widely used in current research and industry. It is a set of powerful engineering simulation software to solve problems ranging from the simple linear analysis to complex nonlinear problems. It is considered to be the most powerful finite element software. Abaqus cannot only do a single part of mechanical and muti-physics analysis, but also can do system-level analysis and research. That is a unique analysis feature compared with other analysis software. Especially, it covers different contact types that can give hard or soft contact, Hertz contact (small sliding contact), and limited sliding contact and so on. And the friction and damping on contact surfaces can be considered and defined as well. It is able to design an accurate simulation of the actual engineering structures. One of the main solver modules, Abaqus/EXPLICIT v6.12 (2012), is implemented in this research.

To build a single particle model in Abaqus, a 1/8 3D meshed spherical geometry is created for the 0.8 mm diameter particle. The material is considered isotropic. The normal force is applied by a rigid flat body in this model. Two simulations are performed, 1) using an elastic model and 2) using an elastic –plastic model. The force-displacement cure is used for comparison with experiments.

Table 3-3 Calculation and simulation input parameters for 1/8 3D ball

| | Experimental Validation model |
|---|---|
| 2/3D | 3D |
| Element type | 3D stress C3D8R |
| Sample shape | 1/8 sphere |
| Displacement in FEM, (mm) | 0.09 |

Figure 3-7 illustrates the stress distribution in a single particle using the elastic perfectly plastic model with material parameters in Table 3-2 and Table 3-3. This distribution is standard and in agreement to the analytical solution.

Some elements reached the yield stress when the displacement reached 0.015 mm. As a result in Figure 3-8, the elastic-plastic model curve matched the experimental result very well. Therefore, the finite element model using input parameters in Table 3-2 is consistent with the experimentally measure compression behaviour of a single particle.

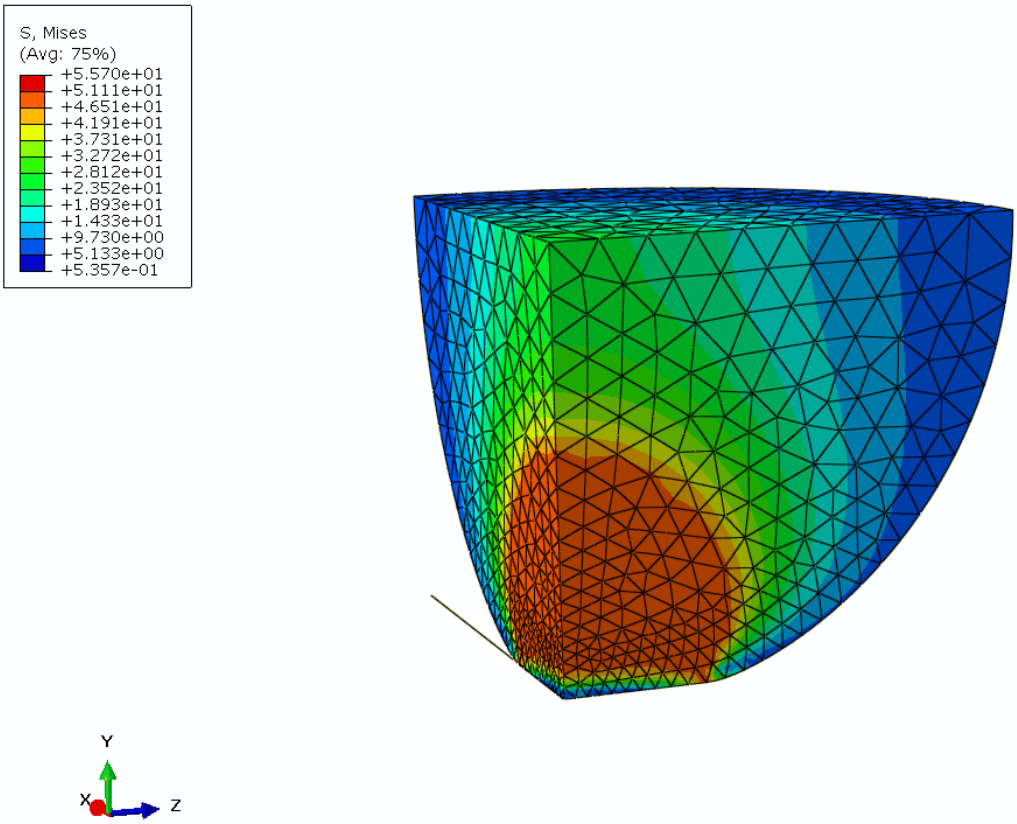


Figure 3-7 Stress distribution in single particle during compression

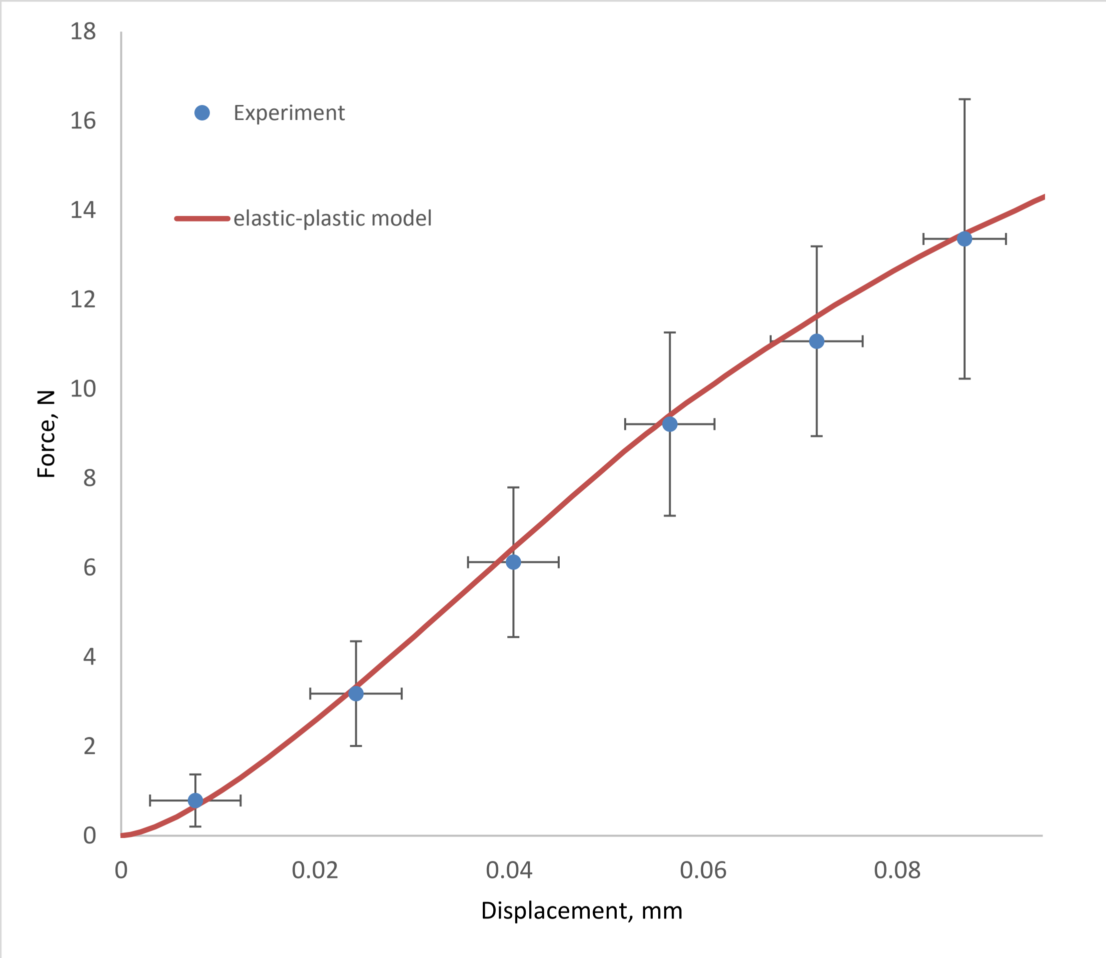


Figure 3-8 Force-Displacement curves from experimental data and FEM

## 3.4 Conclusions

The normal contact of a spherical particle was simulated by the finite element method. The finite element model was calibrated from single particle compression test data. This Chapter established the mechanical properties (E, v and $\sigma_y$) of the particles, which will be used as inputs into MPFEM.

# Chapter 4 Compaction behaviour of powders

Die compaction tests have been adopted by many researchers (Briscoe and Rough, 1998, Wikman et al., 2000, Cunningham et al., 2004). This chapter presents experiments carried out on standard dies (referred to as “closed die”) and in a die instrumented with radia stress sensors (referred to as “instrumented die”). The results are used for calibration and validation of MPFEM.

## 4.1 Experimental methods for multi-particle compaction

### 4.1.1 Closed die system

One of the most representative tests for studying powder compressibility is the closed die compaction. Closed die compaction experiments generate axial stress – density density curves. The axial stress is calculated from the applied load and the density from mass and volume measurements. The advantages of the closed die system are that they reproduce industrial conditions with some accuracy and they are mechanically simple to set-up and operate. However, the system usually has only one force output, thus the effect of friction between powder and die wall cannot be isolated. For the purpose of applying unifoirm stress to the specimen friction should be minimized.

In this research, closed die compacion will be carried out for comparison. The diameter of the die is 11mm, and the inside height is 18.7 mm. The applied loading for the specimen will be around 150 MPa with 1mm/min compression rate. The lubricated punch will be used to reduce the friction effect.

In order to generate constitutive data, it is necessary to measure not only the axial stress but also the radial stress in the specimen. For this purpose a die instrumented with radial stress sensors is necessary. The coeficient of friction between powder and wall can be calculated. The instrumented die system can also be used to measure unloading following compaction; unloading data can be used to deternie the elastic properties as a function of density.

### 4.1.2 Instrumented die compaction

Instrumented die system is widely used (Ernst et al., 1991 and Guyoncourt et al., 2001). In die compaciton the radial strain is zero due to the elastic deformation of the die being neglected. Figure 4-1 (b) shows the die instrumented with radial stress sensor which was used in this research. The diameter of the instrumented die is 10.5mm and the diameter of the sensors is round with 1mm. The position of these two pressure sensors are fixed on 10 and 12mm from the top of the die. The material of the die, the tolerance and the surface finish of the instrumented die are consistent with dies used on high speed pharmaceutical tablet presses.

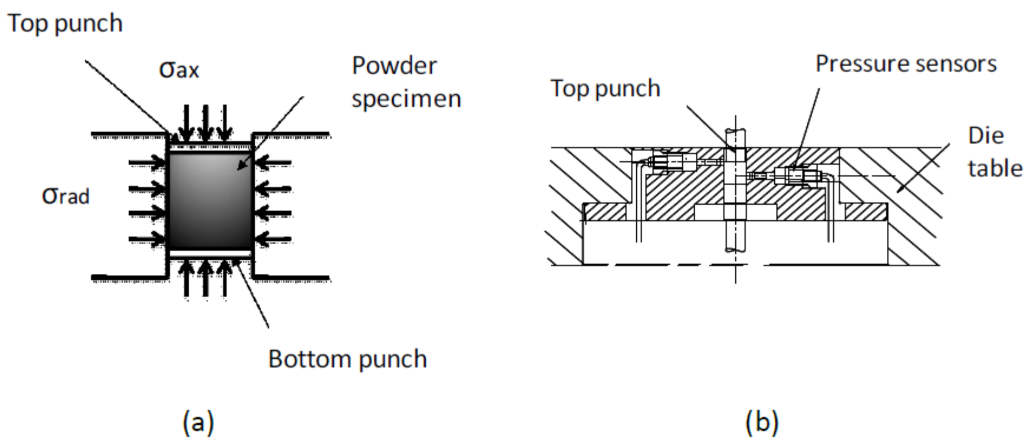


Figure 4-1 (a) Closed die section view, (b) Instrumented die section view (Shang, 2012)

The axial load is applied using a universal tension/compression machine “MTS 810 material testing” manufactured by MTS System Corporation shown in Figure 4-2. The maximum axial load that can be applied by the system is 100 kN (corresponding to around 900 MPa for the diameter of the instrumented die) the radial stress was limited to 200MPa by the construction of the sensors.

The die is assembled into the MTS system as shown in Figure 4-2. The lower punch is stationary and the load is applied using the upper punch. The forces applied by both top and bottom punches are measured and the corresponding axial stress is calculated. Because of the effect of friction, the force applied by upper punch is always larger than the force transmitted to the lower punch.

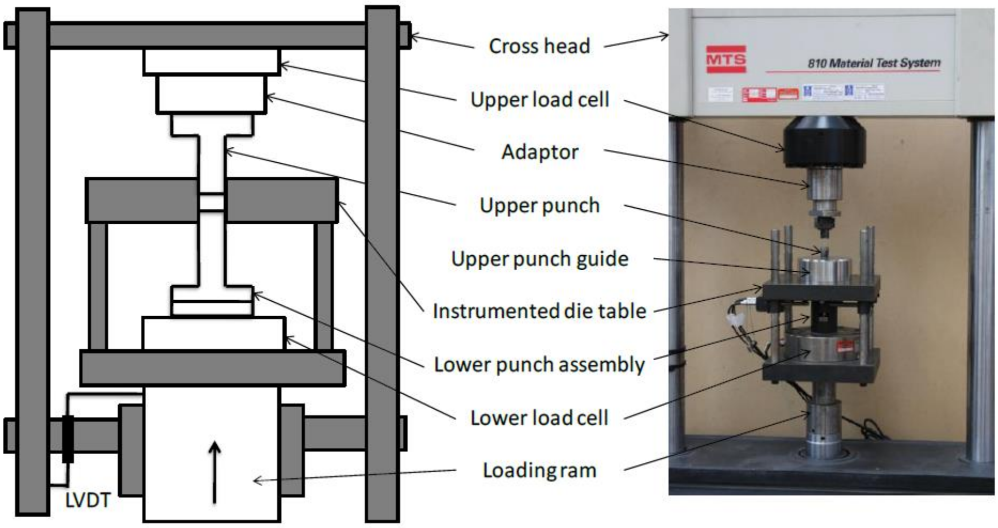


Figure 4-2 Illustration of instrumented die system (Shang et al., 2011)

Before the compression, the die and punches is pre-lubricated using magnesium stearate in order to reduce the friction effect. The zero position of the top punch is set to the top of the die during a calibration routine. During this compression process, the displacement of the top punch is measured using a linear variable differential transformer mounted to the cross-head of the MTS testing machine. The axial strain is calculated using the logarithmic definition of strain. The compression force at the top and bottom punches are recorded. The outputs of the MTS system are: displacement $\mathrm{d}$ of top punch, top punch force $\mathrm{F_T}$, bottom punch force $\mathrm{F_b}$, radial stress at top sensor $\sigma_{rt}$ and bottom sensor $\sigma_{rb}$. The axial stress at top and bottom are calculated by:

$$\sigma_t = \frac{F_t}{A} \text{ and } \sigma_b = \frac{F_b}{A} \tag{4-1}$$

Where $A = \pi D^2/4$ is the cross-sectional area of the die.

The initial die internal height for powder fill is 13.5 mm. The powder is carefully filled into the die by hand in order to achieve a uniform packing. A scraper is used to level the top surface of the powder to same level as the die. For tablet ejection, the lower punch is removed and the tablet is ejected using the top punch. The loading and unloading rates are set at 10 mm/min and 1mm/min.

## 4.2 Results and data extraction

### 4.2.1 Elastic compliance of compaction systems

The elastic deformation of the testing frame under the applied load is included in the displacement output of the system. Correction for system compliance is therefore necessary.

The compression machine is typically made of steel. Also, the strain is workout by a displacement measurement. So, in a closed die and instrumented die system, it is very important to recognise that the specimen cannot be exported directly. The total displacement includes not only the deformation of the specimen but also the elastic compliance of various elements of the testing frame (e.g. punch and load cell). The punch deformation is still significant even if testing frames are so-called “stiff”. To determine the stiffness (or its inverse, the compliance) of the testing frame, the top and bottom punches are compressed together (without a powder sample). The displacement-force relation for the system loading is shown in Figure 4-3 and Figure 4-4 for the closed die system and the instrumented die system, respectively. The force-displacement curves are non-linear at the beginning of compression and become linear at higher loads.

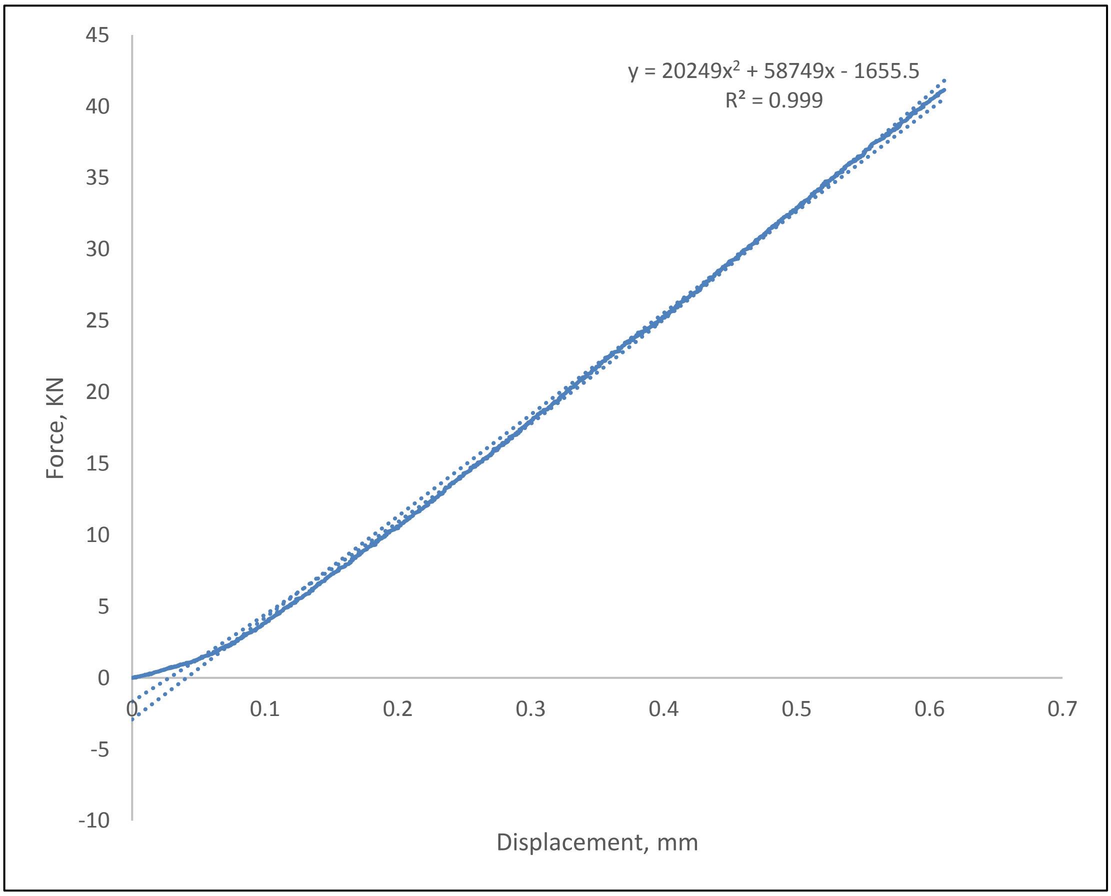


Figure 4-3 Compliance curve of closed die compaction

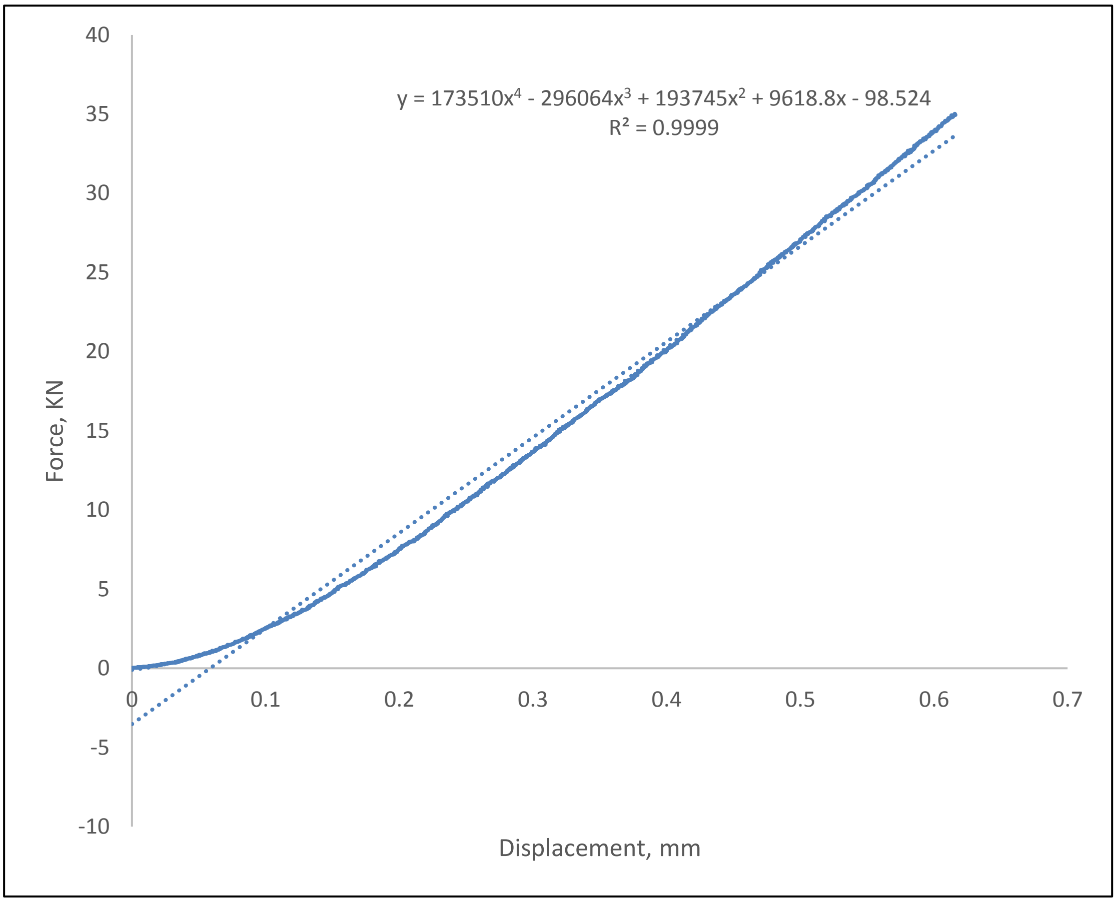


Figure 4-4 Compliance curve of instrumented die system

Figure 4-5 compares the corrected and uncorrected displacements for a typical closed die compaction experiment.

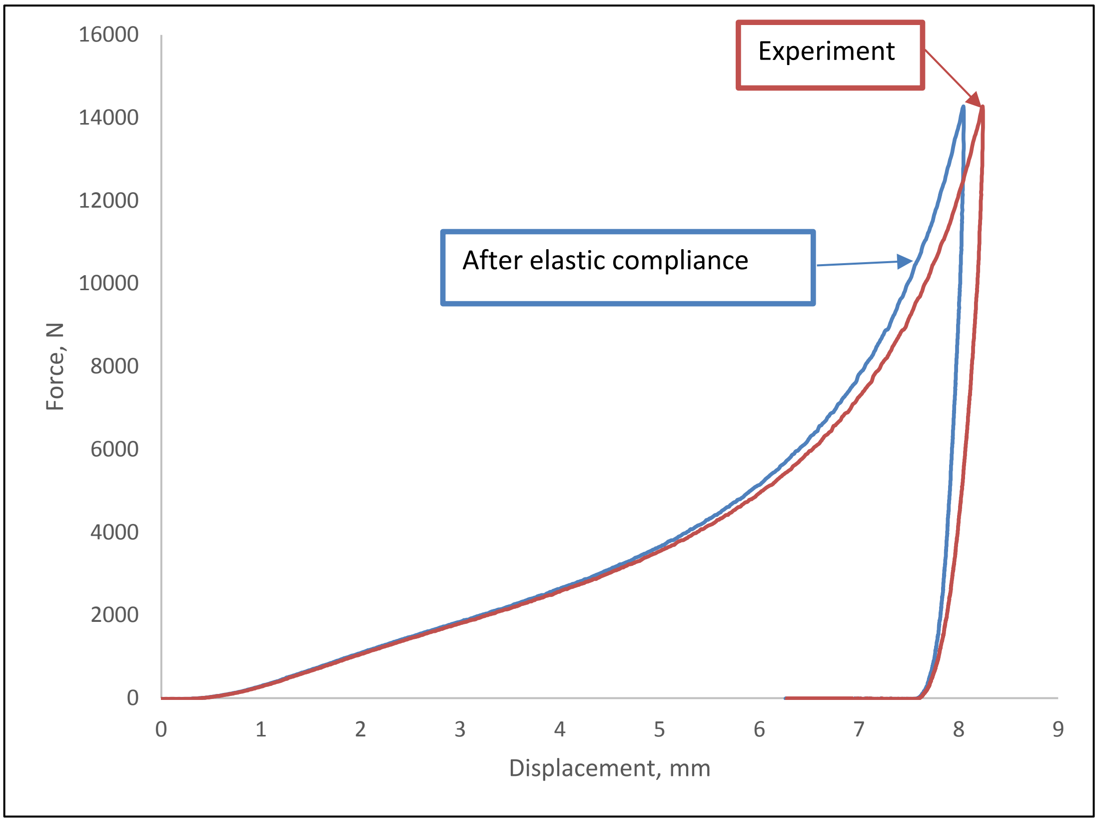


Figure 4-5 Full curve of Force-displacement behaviour of close die compaction

The axial stresses applied by the top and bottom punch being different, the specimen is subject to non-homogeneous stress Thus the strain is also non-homogeneous. In order to extract constitutive data, this effect was eliminated using the procedure developed by Shang (Shang et al., 2011).

### 4.2.2 Closed die compaction results

Closed die compaction has been carried out for axial stress levels under 150MPa. The result of a typical closed die compaction test after elastic compliance is shown in Figure 4-6. Because there is only one axial force sensor in closed die system, one loading and unloading curve was obtained. Compared with the stress-density curve from instrumented die compaction (also shown in Figure 4-6), the result of closed die compaction agreed closely with the axial bottom stress-density curve of instrumented die compaction. The discrepancy is due to the effect of friction between powder and die which is not identical in the two systems.

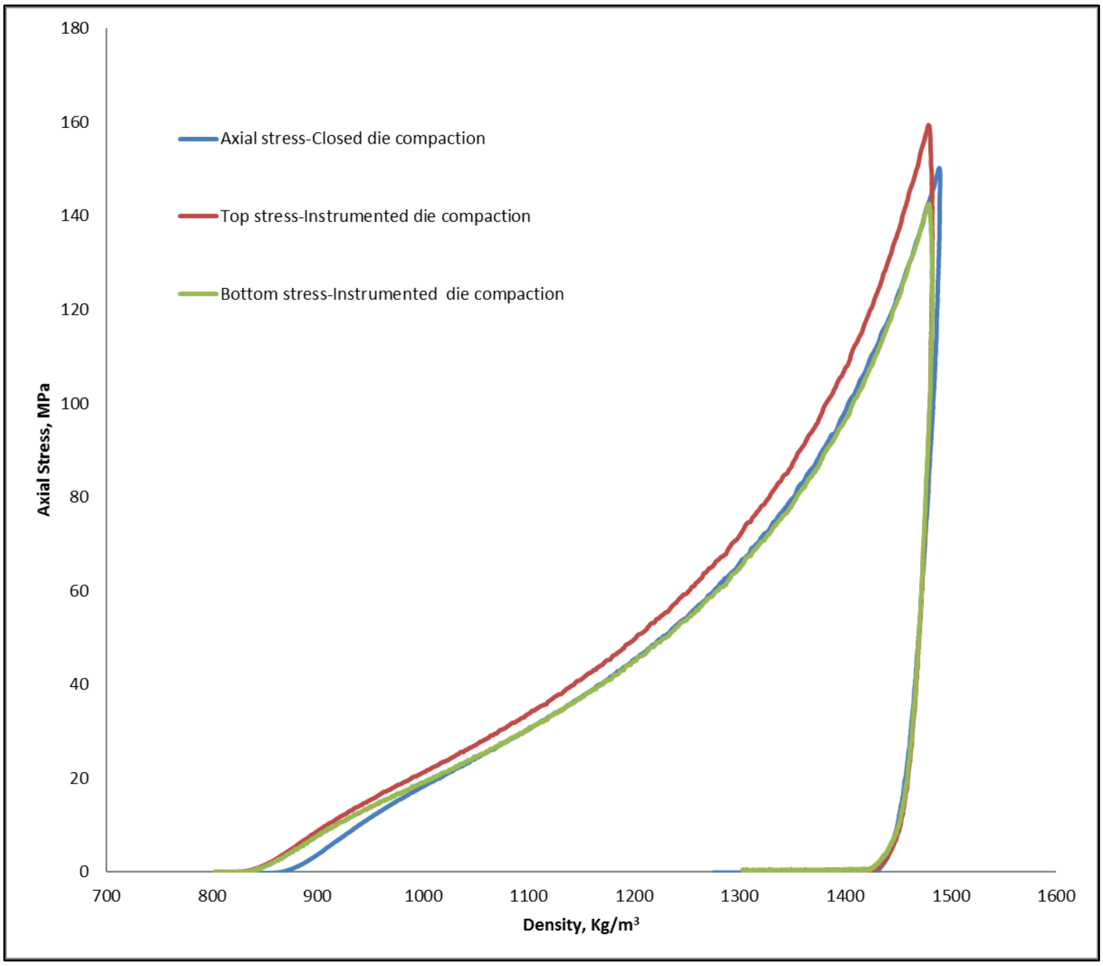


Figure 4-6 Comparison of closed die and instrumented die compaction

### 4.2.3 Instrumented die compaction results

A close up image of the compressed particulate structure is presented in Figure 4-7. A Typical stress density curves are presented in Figure 4-8. Five repeated experiments show good agreement. Therefore, only one result shown in Figure 4-8. As expected, the top axial stress is always larger than the bottom stress. However, the radial stresses measured by the top and bottom radial stress sensors are inconsistent due to experimental errors related to particle size (0.8 mm diameter particles are comparable to 1 mm diameter radial stress sensors).

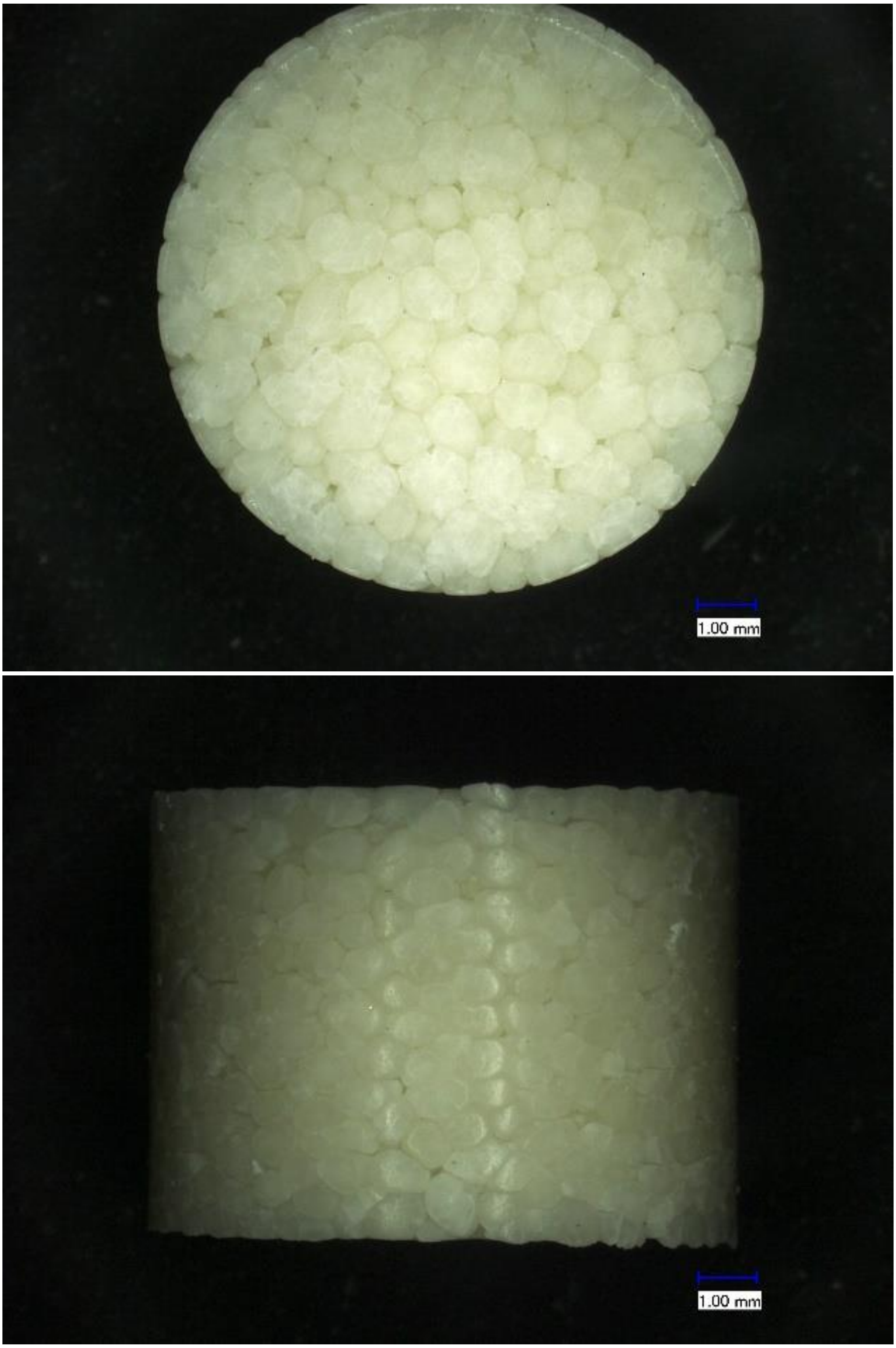


Figure 4-7 Top and side views of Specimen after 150 MPa instrumented die

compaction under microscope

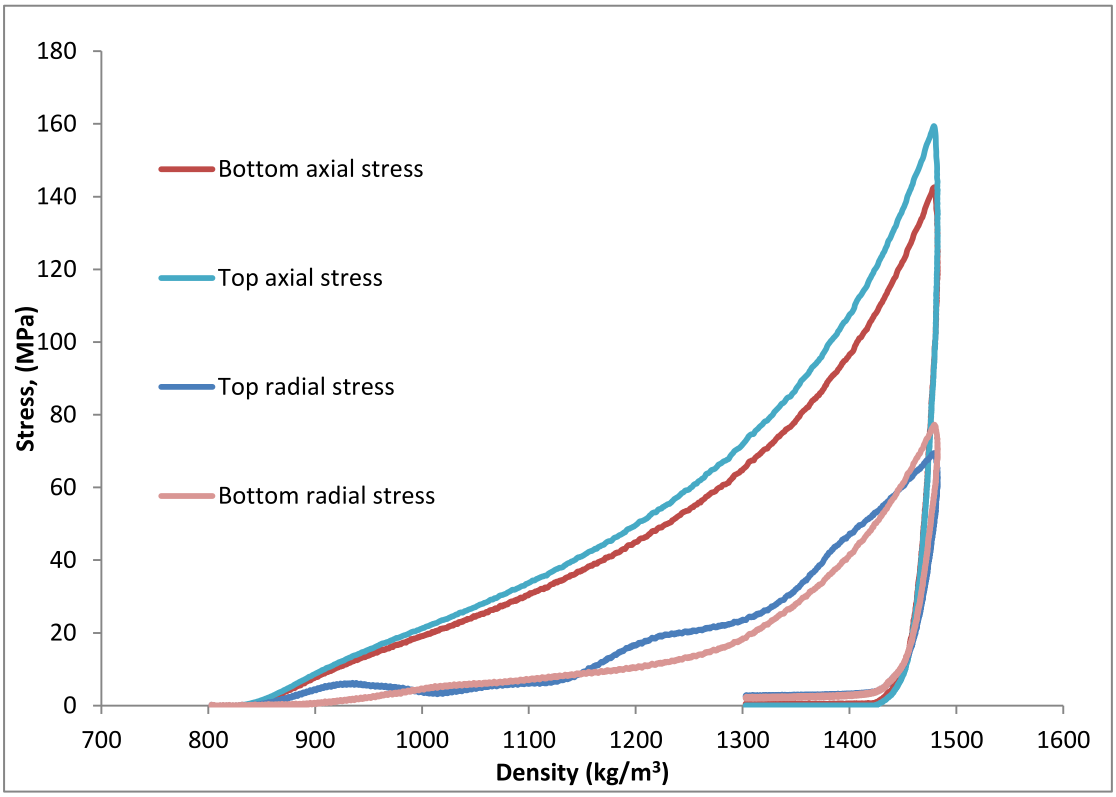


Figure 4-8 Data from instrumented die compaction

The average stress defined by using the Janssen-Walker method shown as

$$\sigma_{average} = \frac{\sigma_T - \sigma_B}{\ln\frac{\sigma_T}{\sigma_B}} \tag{4-2}$$

The average stress-density response of the sample can therefore be described as demonstrated in Figure 4-9 Compared with top and bottom stresses, the average stress well represented using Janssen-Walker method. This average curve will be used in further MPFEM validation.

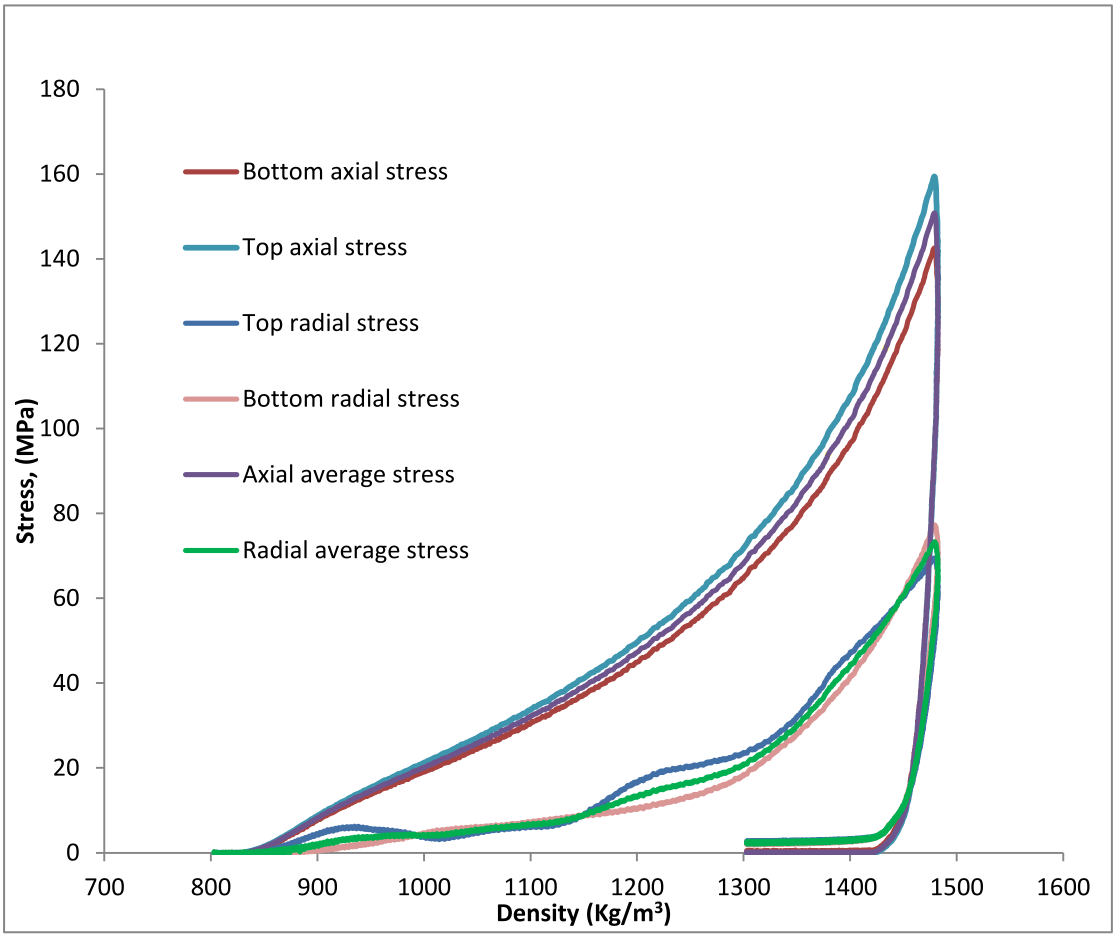


Figure 4-9 The average, top sensor and bottom sensor stress-density curves from instrumented die compaction

## 4.3 Conclusions

Closed die and instrumented die compaction experiments were performed. The main outputs show the use of the closed die and the instrumented die system. The friction of wall and particles still affect the final result. Compared with close die compaction, the instrumented die system can give loading range by different sensors which is more reliable in analysing the particle characterisation. The radial and axial stress evolutions with density obtained from the instrumented die compaction test which are used to validate MPFEM described in Chapter 6.

# Chapter 5. Characterisation of particle packing using X-ray CT

X-ray CT is carried out using a X-TEK 225kv system which is shown in Figure 5-1. X-ray CT is non-destructive technique which can be used to visualise particle shape and packing arrangement for real powder. This technique is based on collecting radiography images on a sample that is rotated 360 degrees in small increments. 3D reconstruction is carried out to generate detailed structural information.

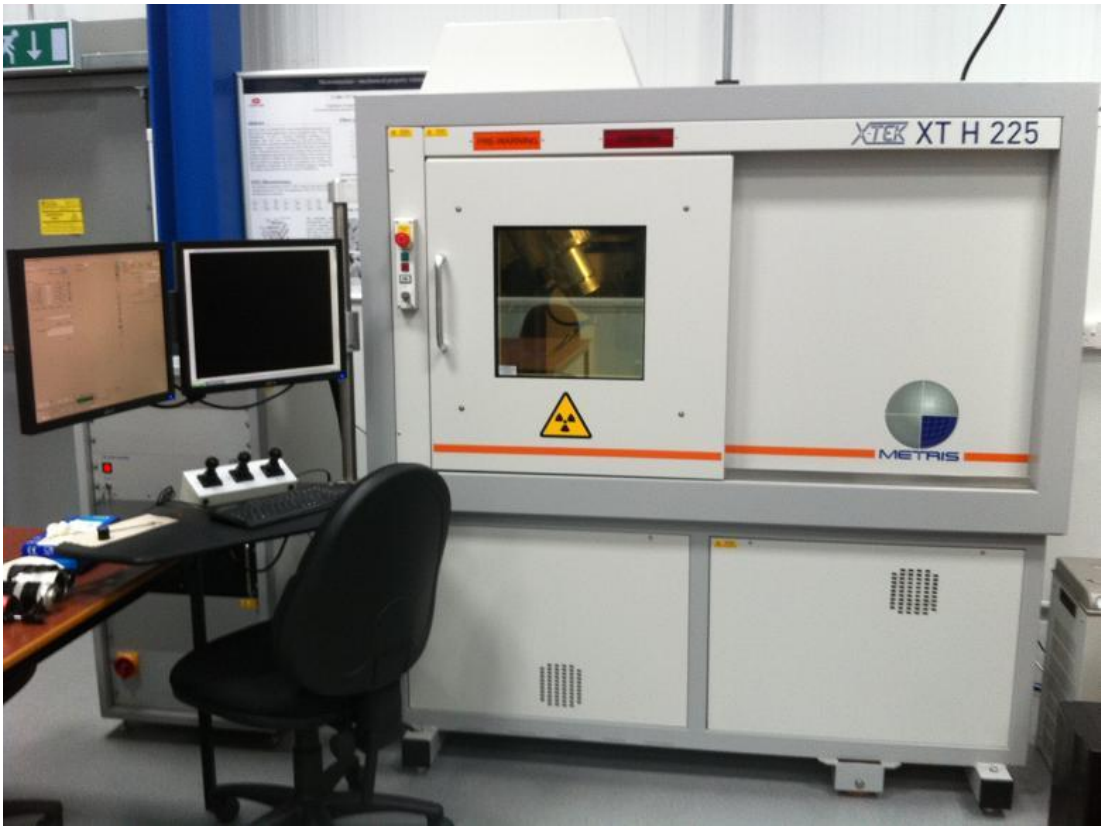


Figure 5-1 X-ray CT system

## 5.1 X-ray CT imaging method

A plastic die having a diameter of 4 mm is manufactured and assembled onto an aluminium base. The material is chosen in order to be transparent to X-rays. The die is filled with the particles and placed upon the rotation stage in X-ray system. As the specimen is made of microcrystalline cellulose (a relatively low density material), the powder of X-ray source was set at 75keV and a current of 125 μA. To reduce the beam hardening effects, 0.5mm aluminium plate was placed over the X-ray source to filter the low energy X-rays.

X-ray CT builds complete reconstructions of a three dimensional object assembled by a series of cross-sectional images. The following settings were used:

1. Sample setup. The specimen is rotated to ensure that it stays in the field of view through 360 degrees. The numbers of projection images and a number of frames are specified. The numbers of projection images are the total number of CT images that are taken. Because the structure of particle packing is complex, 2000 projection images were generated in this study. A typical frame presents a level of noise. For improving image quality 16 or 32 frames were averaged (the signal to noise ratio is proportional to the square root of the number of frames; whereas the time to acquire is proportional to the number of frames; e.g. doubling the number of frames doubles the acquisition time, however, increases the signal to noise ratio by 40% only). As long as the noise is low in an average of the number of frames that has been chosen, then the number of projections should be increased as this gives extra angular information as well as a higher signal to noise ratio. In this study 4 frames were used;

2. Shading correction. At this point, the specimen position and structure (shown in Figure 5-2) at which the CT scan will be done is established. Also the imaging and X-ray conditions are stored. The aim is to clear the background of scanning area by collecting white and black reference images which are generated without the specimen in view. After shading correction, the specimen is automatically moved back to its initial position;

3. Centre of Rotation. When the shading correction images have been collected, the centre of rotation is acquired and generate a red line in the image. The red line needs to move to a height at which the specimen structure does not change rapidly with height and there is good contrast in the image. It is better fairly close to the image centre line, otherwise determining the centre of rotation can take a long time. Because in order to reconstruct the central slice, only a single line needs to be read out of every projection image whereas to reconstruct a slice offset vertically. Since this projects as a band, a band of lines needs to be read from each projection image which takes a lot longer;

4. Reconstruction setup and acquisition. Reconstruction setup involves selecting the final scanning area by delimiting the total size of the image on the top and side views of the specimen. Acquisition involves storing the data, which are then transferred to a workstation for generating 3D reconstruction.

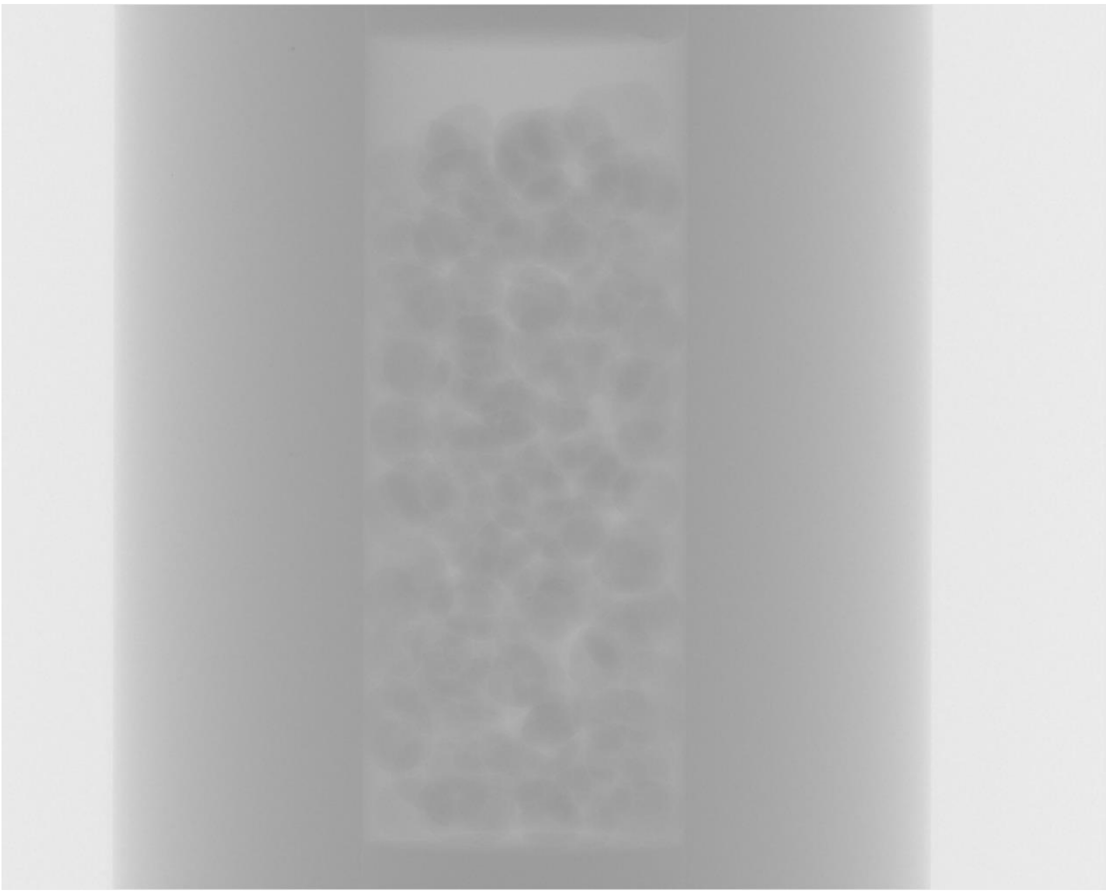

Figure 5-2 An example of radiography of particle packing arrangement in scanning system

## 5.2 Results and analysis

The 3D reconstruction of the particulate assembly is presented in Figure 5-3 and it well indicated the detail of particle shape and packing arrangement. The 3D reconstruction is generated by a pixel-based approach in which the 3D image is reconstructed using a filtered projection algorithm (Orlov, Morgan &Cheng, 2006). The quality of the final 3D geometry is affected by errors and limitations of the reconstruction algorithms, which limit the degree of detail of the image. The use of squared pixels is inaccurate for representing particle contacts because a contact is not identified as a boundary between two separate particles. Particles appear to merge together at the contacts because of the insufficient microscopic accuracy of the X-ray CT. To solve this contact problem, Meshlab (which is an open source, portable, and extensible software for processing and editing of unstructured 3D triangular meshes) was used to help the processing of the typical unstructured geometry arising in 3D scanning, providing a set of tools for editing, cleaning and converting meshes. From the X-ray CT system, the 3D geometry is created by approximated using a triangle mesh, which is exported to Meshlab as a stereolithography (STL) file. Meshlab simplifies the geometry and can reduce the total number of faces significantly (in a particular case from 1612276 to 20000) and the total vertices is also simplified (from 804638 to 9479 in the example referred to above). In order to avoid a distorted particle packing, the numbers of faces are redefined as no less than 20000 (shown in Figure 5-4). The simplified model does not only make it easier to edit contact area, but also reduces the calculating time in further simulation.

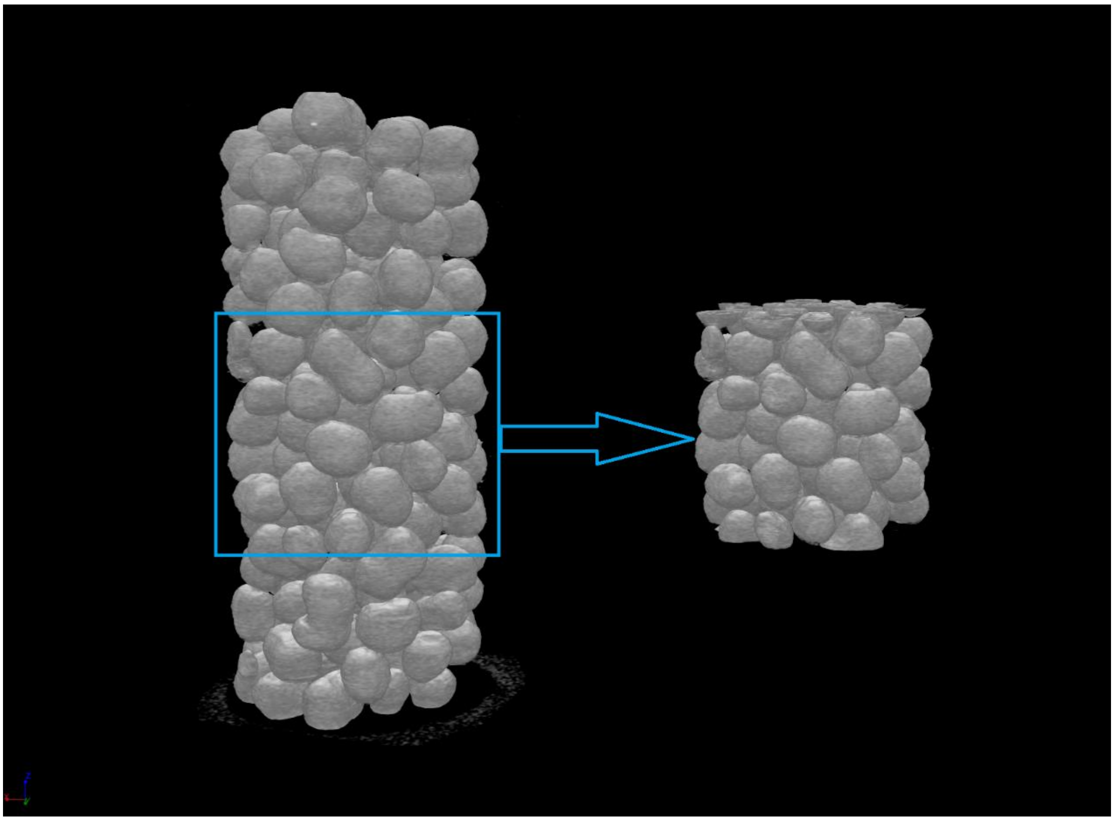

Figure 5-3 The 3D reconstruction of real packing arrangement in X-ray CT system

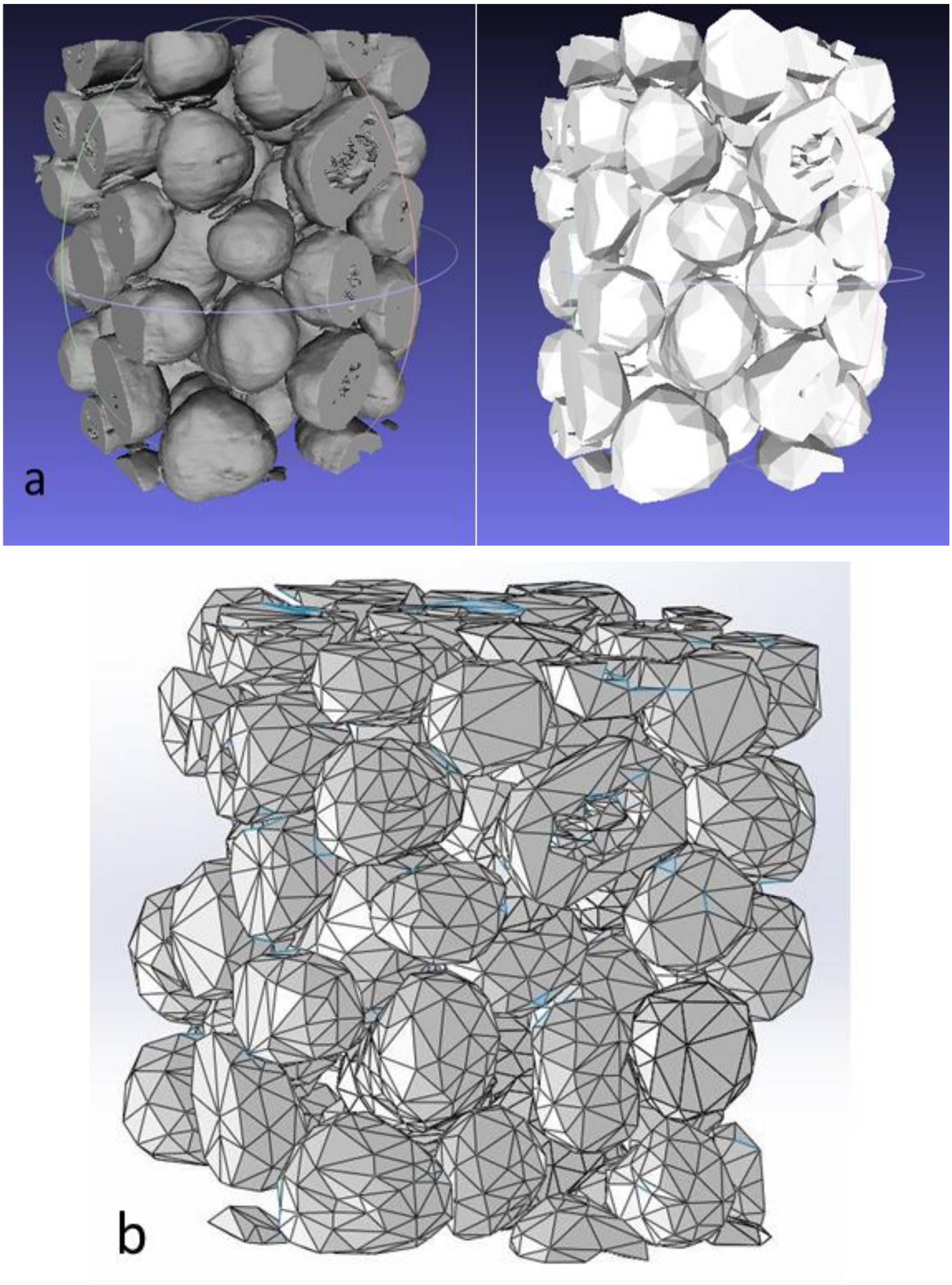

Figure 5-4 The particle packing edited in Meshlab (a) and Solidworks (b)

After simplifying the surfaces of the particles, the merged areas between particles are redefined as distinct particle in contact using Meshlab. Then, particles are individually located but with the loophole. To fill these loopholes, Solidworks is implemented to close every single particle using 3D editing surface feature. In Solidworks, triangle faces can create by nodes along the loophole. Some cavities have been found using X-ray CT. showing the actual structure of the particle. However, the presence of cavities also create difficulties regarding meshing, which increases the computational effort in the FE model. The reason to create only triangle faces rather than rectangular faces is the initial geometry generation mode of 3D reconstruction in X-ray CT system. It may affect the mesh definition in further multi-particle FE model as well.

## 5.3 Conclusions

X-ray computed tomography has been successfully applied to generate 3D packing straucures of the particles as input data into MPFEM. X-ray CT can be used to visulalise irregular particles and packing arrangements. It has allowed image capture rather than simplifications of the real irregular particle shapes into spheres or cluster of particles. Due to the limitation of X-ray CT system, two pieces of software are involved in the editing of the particles contact area. A processing method was developed to produce 3D geometry in a format that can be readily imported into FEA packages. This method is to offer a possibility of presenting studies of particle packing, especially to investigate the relationship between particle morphology and packing arrangement. It has the advantage that can be helpful to understand the practical particle compaction process.

# Chapter 6. Multi-Particle Finite Element Modelling of compaction

MPFEM of compaction involves setting up a discrete assembly of particles that form a representative a unit cell, which was chosen as a cuboid. Numerical tests are set-up by applying a defined macroscopic strain conditions. The commercial finite element software Abaqus/EXPLICIT v.6.12. The set-up of the model involves importing the three-dimensional geometry from X-ray CT, creating rigid bodies to represent the compression tool surfaces, defining the material properties and section properties of the unit cell; defining the analysis procedure and output requests; applying boundary conditions; meshing; and finally running and analysing the results.

## 6.1 Model construction

Since the unit cell is created from X-ray CT system and edited in Meshlab and Solidworks, only six rigid bodies need to be created in part section, and the unit cell is imported as a part. The size of rigid bodies is larger than the unit cell which is measured as 3.12mm in height, 2.76mm in length and 2.64mm in width.

### 6.1.1 Material properties

The properties of particles are presented in Table 6-2. Since Abaqus does not use a built-in system of units, thus all input data were specified in consistent units as presented in Table 6-1:

Table 6-1 Consistent units

| **Quantity** | **SI** | **SI (mm)** |
| --- | --- | --- |
| Length | m | mm |
| Force | N | N |
| Mass | kg | tone($10^3$kg) |
| Time | s | s |
| Stress | Pa(N/$m^2$) | MPa(N/$mm^2$) |
| Energy | J | mJ($10^{-3}$J) |
| Density | kg/$m^3$ | Tone/$mm^3$ |

The interaction between wall and particles is defined as frictionless in order to contribute a uniform stress state. No inter-particle cohesion need was considered; this choice was motivated by an argument put forward by Procopio and Zavaliangos (2005). For under monotonic loading, cohesion does not play a significant role (Procopio and Zavaliangos, 2005). The contact between particles is represented by friction as shown in Table 6-2.

Table 6-2 MPFEM particle properties and model boundary conditions

| | |
|---|---|
| Particle shape | Irregular( close to spheres) |
| Particle density | 1480 kg/m$^3$ |
| Particle radius (average) | 0.8mm |
| Element type | 3D stress |
| Number of elements | 109857 |
| Number of nodes | 25177 |
| Young's modulus (E) | 1.3GPa |
| Poisson's ratio (v) | 0.35 |
| Yield strength ($\sigma_{yield}$) | 40MPa |
| Friction coefficient (μ) | 0.2 |

Particles subject to compression undergo a range of deformation and densification mechanisms, which are not captured by a linear elastic-perfectly plastic constitutive model. The hardening behaviour of a material (increase of yield strength with plastic deformation) can be measured using different techniques (e.g. nanoindentation), however, due to the structural length scales involved (the compact is made of 0.8 mm particles, which are made of 50 micrometer granules, which are in turn made of micrometre size particles), existing experimental methods were considered impractical. A numerical study has been carried out by considering (assumed) hardening law of this MPFEM as illustrated in Figure 6-1. This hardening law of particles created from lines as a start to find out slope, then a suitable curved hardening law was chosen so that a match between MPFEM and instrumented die experiments could be obtained. The hardening law played an important role to support the model after yield stress achieved.

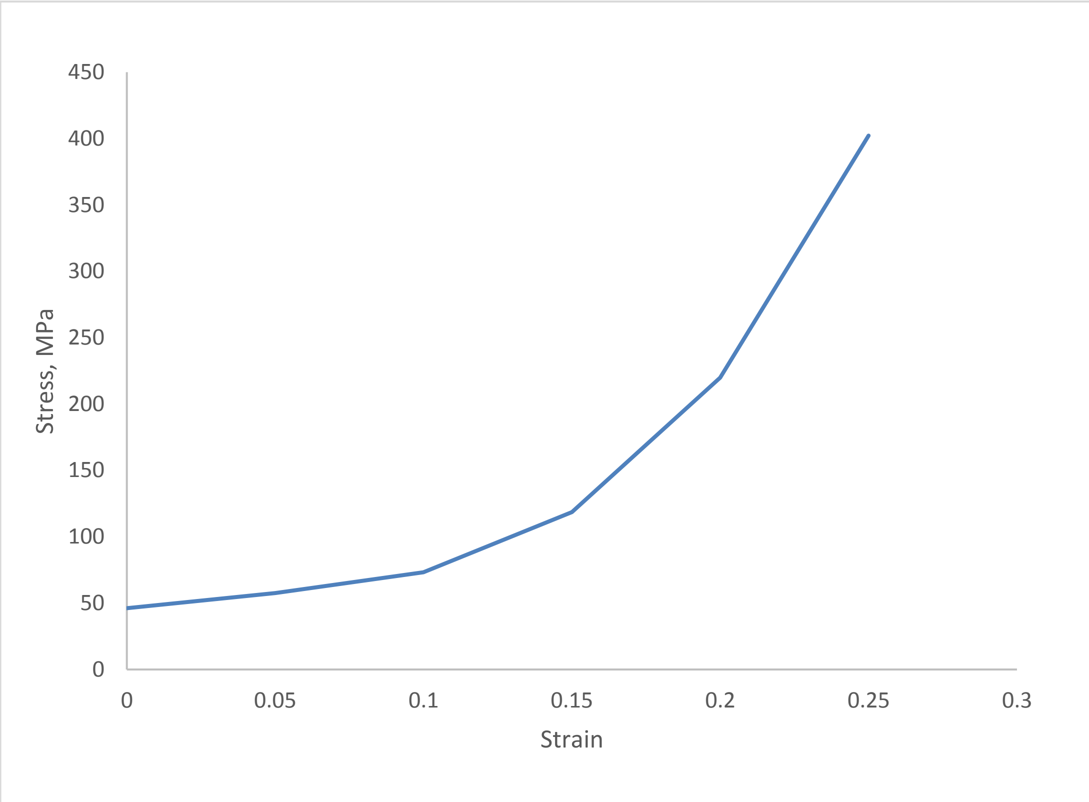


Figure 6-1 The numerical hardening law using in FEM

### 6.1.2 Time step

For computational efficiency in quasi-static analyses that contain a few very small elements, mass scaling can be used to control the stable time increment. Powder compaction simulations involved complex contact conditions. Because the explicit central difference method is used to integrate the equations in time, the discrete mass matrix used in the equilibrium equations plays a key role in both computational efficiency and accuracy for complex nonlinear problems. Mass scaling can often improve the computational efficiency while keeping the necessary degree of accuracy required for a particular problem level if used appropriately (Abaqus, 2006).

Because the quasi-static simulation incorporates strain rate-independent material behaviour, the natural time scale is generally not important. In order to get a computationally economical solution, methods of reducing the time period of the analysis or increasing the mass of the model artificially are often used. If the strain rate dependencies are included in the model because the natural time scale is considered, mass scaling is the first choice for reducing the solution time. Mass scaling is usually used on the entire model. However, when different parts of a model have different stiffness and mass properties like these discrete particles in FEM, it is useful to scale only selected parts of the model or scale each of the parts independently. It is not generally possible to increase the mass arbitrarily without degrading accuracy. A limited amount of mass scaling will result in a corresponding increase in the time increment and a corresponding reduction in computational time. However, it must be ensured that changes in the mass and consequent increases in the inertial forces do not affect the solution significantly. In this study, semi-automatic mass scaling is selected to perform fixed mass scaling at the beginning of the simulation step. In addition, scale to a target time increment of n is involved to enter a desired element stable time increment in the field provided. If this is below the minimum target, it is only element scaled; its stable time increments are less than the given time increments, so that the stable time increments are equal to the defined time increments.

### 6.1.3 Finite element mesh

The model geometry is transferred from the software packages described in Chapter 5. The original mesh (shown in Figure 5-4 b) was refined within Abaqus as represented in Figure 6-2. Given that finer mesh is necessary only at contact regions, global adaptive mesh refinement was therefore used, which employs an error estimation strategy to determine the point in the modelling domain where the local is largest. Then the system solves this error estimation using the information to create an entirely new mesh. Smaller elements are used in the area where the local error is significant, and the local error throughout the model is considered. Different mesh size are tried without any change, and bigger mesh is selected in order to reduce the amount of CPU calculation.

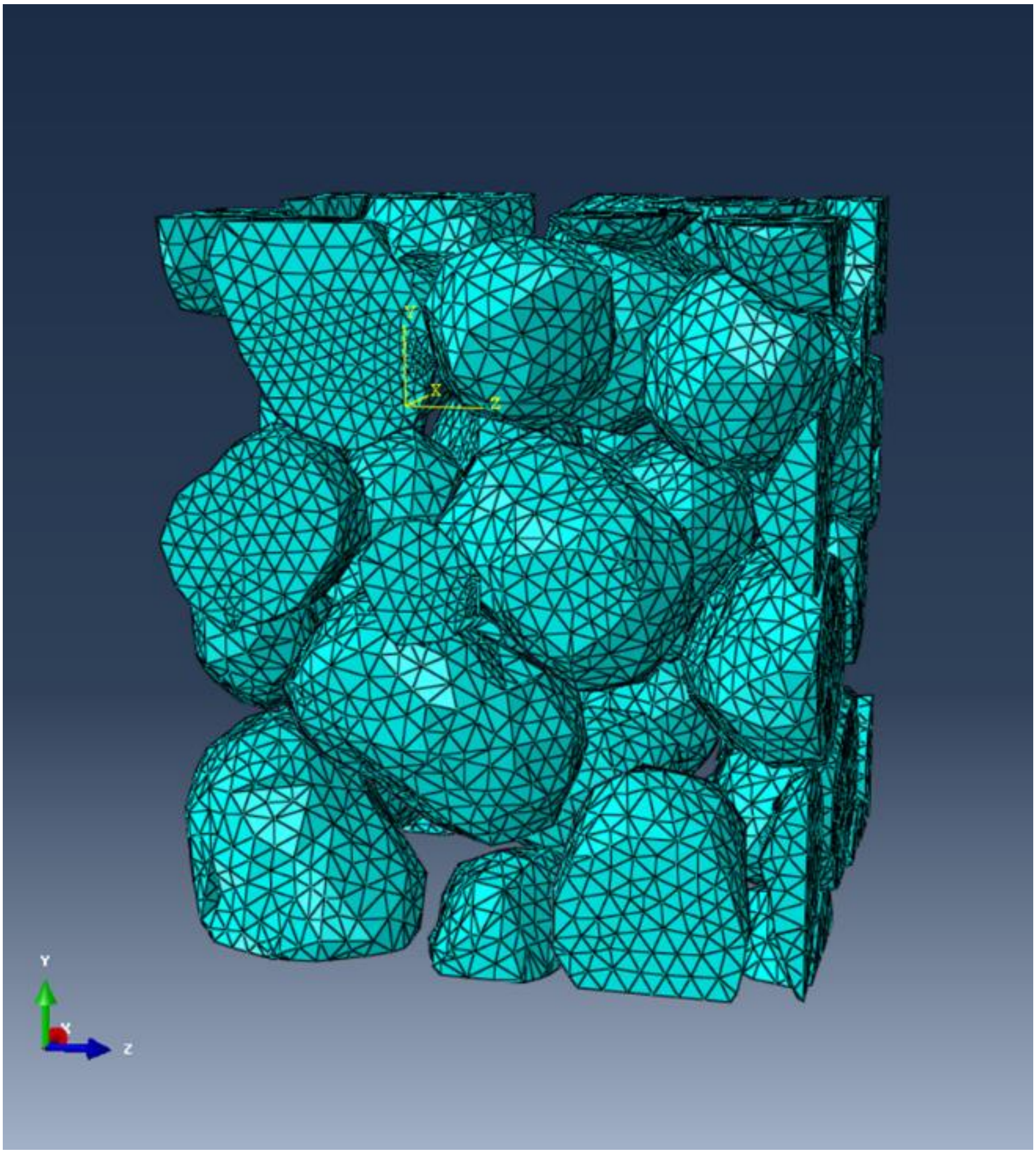

Figure 6-2 Fine mesh defined in Abaqus

### 6.1.4 Boundary conditions

The numerical tests are prescribed using boundary conditions and use of rigid body movement. The rigid surface applies displacement boundary conditions through their interactions with neighbouring particles. The disadvantage of this technique is that of the wall effect, which means the presence of a layer of particles next to the wall that may not be representative of the overall collection of particles. Nevertheless, it is sufficient to generate macroscopic stress-strain behaviour. There are six rigid bodies in the model, five fixed and one moving boundary, representing the faces of the cuboid. and simulating close die compaction.

## 6.2 Result and discussion

The establishment of the MPFEM is successful for powder compaction. Figure 6-3 shown the initial packing arrangement and compressed particles in MPFEM. It can be observed that the particle labelled (a) is initially contact with another particle, labelled (c). During compaction, particle (a) makes contact with particle (d) and particle (b). Particle (b) not only translates to a centre position but also rotated during compaction. This particle rearrangement occurred at an early stage of the compaction process.

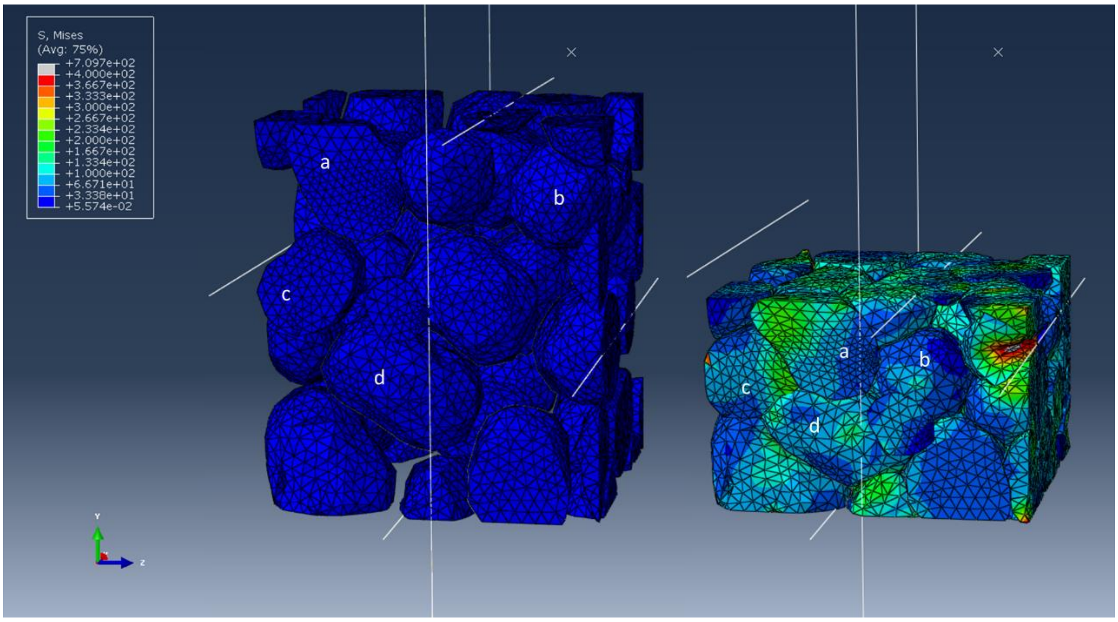


Figure 6-3 MPFEM of uniaxial compaction

In the simulation process convergence issues were experienced and mesh distortion problems were triggered. For the model convergence, friction played a key role in improving convergence. Distortion was solved by massing scaling and global adaptive mesh. Meanwhile, the mass scaling can obviously decrease the simulating time by neglecting the tiny element effects. To calibrate the multi-particle model, the average of the axial stress from instrumented die compaction (section 4.2) was used to illustrate whether single particle properties are suitable to present in the multi particle model. An elastic perfectly plastic model is created in order to explain the necessity of hardening law in MPFEM. Compared with experimental data, the model results, which are represented in Figure 6-4, shown a good agreement. The results can describe well the elastic behaviour of the multi-particle compaction using single particle properties and an empirically determined hardening law.

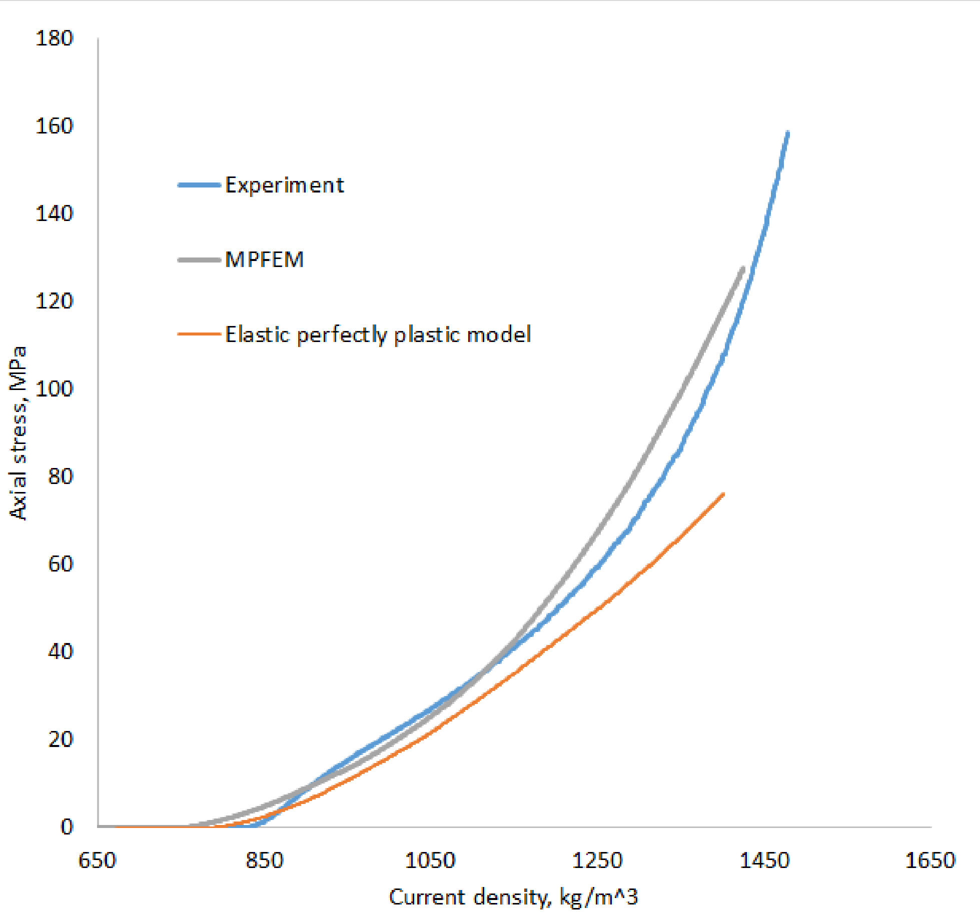


Figure 6-4 Uniaxial compaction of MPFEM and Instrumented die compaction result achieved in Chapter 4

## 6.3 Conclusions

MPFEM is capable of capturing rearrangement, rotation, non-affine motion and large deformation to high densities. MPFEM gives the necessary degrees of freedom that allow for realistic contact deformation. It also captured the statistical nature of a powder bed.

MPFEM predictions are consistent with experimental results generated using a instrumented die method. The methods developed in this work is relevant to practical powder compaction by its use of realistic particle shapes, packing arrangements and material properties.

# Chapter 7. Constitutive law development

The deformation plasticity model is used as a theoretical framework for the evaluation of material behaviour for a class of loading histories experienced in practical processing (Sinka and Cocks, 2006). Deformation plasticity provides a general framework for the analysis of MPFEM data as described below.

## 7.1 Methodology to develop constitutive law using MPFEM

MPFEM was used to generate a set of numerical experiments where radial loading in strain space is applied by prescribing different ratios between the macroscopic strains applied. Six types of triaxial compression have been conducted as shown in Figure 7-1. "SR" indicates the strain ratio which is calculated by lateral strain (equal in tow of the directions, for convenience of cross-referencing with the closed die cylindrical configuration this will be referred to as "radial" strain ) divided by the strain in the third direction (referred to as "axial" strain).

Apart from the boundary conditions that apply the radial loading in strain space all other model parameters presented in Chapter 6 are retained.

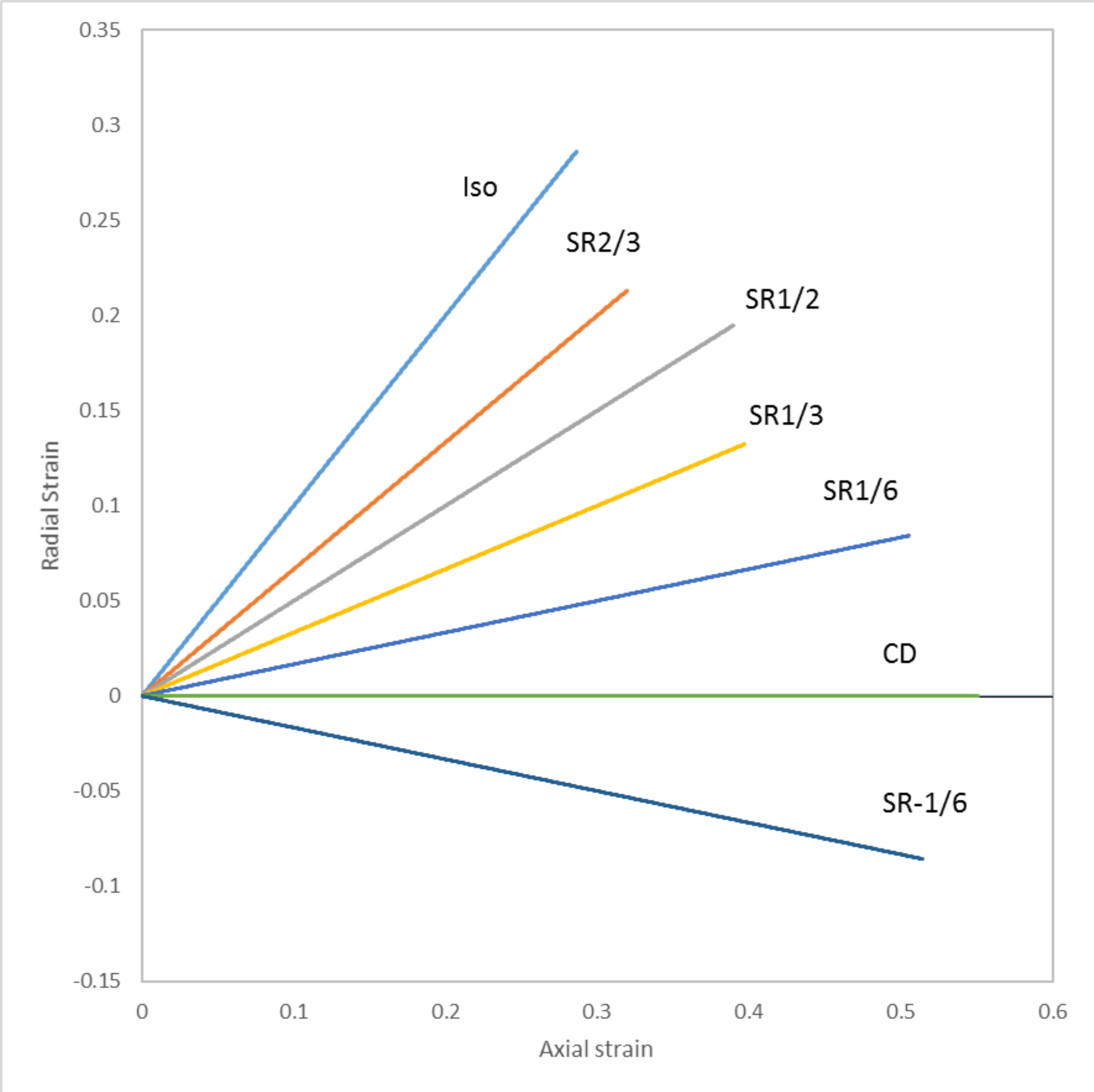


Figure 7-1 Types of numerical compression tests: CD- closed die compaction, SR- radial loading in strain space labelled as the radial to axial strain ratio, Iso- Isostatic compaction

# 7.2 Results and discussion

## 7.2.1 Contours of constant density

There are two types of contours plots which are motivated by different types of constitutive models. In previous research, the models of powder compaction have assumed that the state of the material can be described by using the density (Trasorras et al., 1998). Density based model are motivated by practical desire to maximise the performance of the product by maximising the total density and minimising any density variations. The density contours in effective stress and hydrostatic stress space are shown in Figure 7-2. The effective and hydrostatic stress of each compression is chosen based on same density. Then, these points are linked as a contour. Five level of density are picked to show the group of contours. However, the contour lines do not form a set of consistent convex contours that may be related to yield surfaces. It can be concluded that the isodensity plots were not sufficiently coherent to offer a suitable basis for developing constitutive models for the particle properties and packing arrangements considered, which is sensitive to deformation during the early stages of compaction. Even considering the uncertainties introduced by the sensitivity of the response at early stage of compaction, it can be concluded that density is not the most appropriate variable to characterise the compaction response from dense random packing of particles to full density.

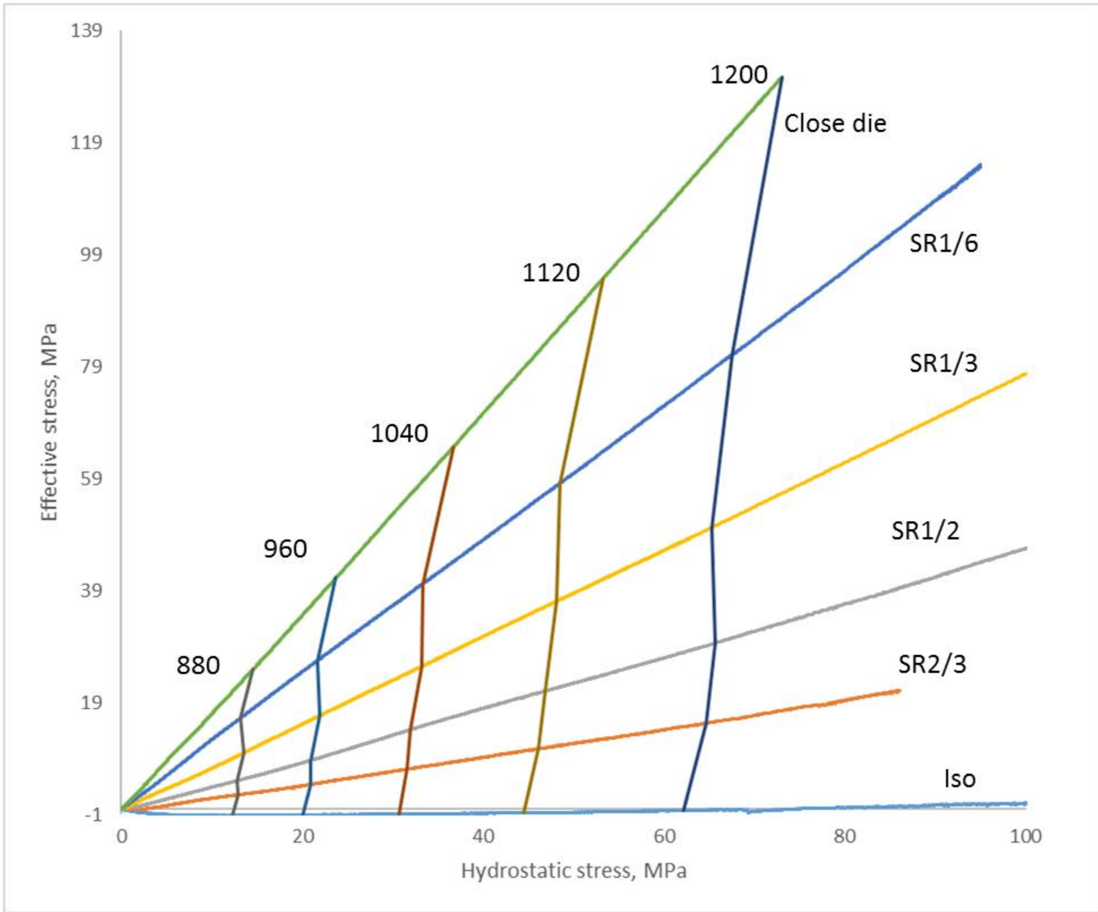


Figure 7-2 Isodensity contours, labels indicate current density (kg/m$^3$)

### 7.2.2 Deformation plasticity framework

In this section the numerical experiments are analysed using the deformation plasticity framework. The model proposed by Cocks and Sinka (2007) is introduced first.

Deformation plasticity using total true strain and Kirchhoff stress. Three types of test in Kirchhoff effective stress-hydrostatic stress space has been achieved: simulated close die compaction, different strain ratio of triaxial compaction and isostatic compaction. The actual values of the hydrostatic stress and effective stress at same value of the complementary work done are shown in the Appendix. Contours of complementary work done are constructed in Kirchhoff stress space. In order to find a coherent set of convex contours, SR-1/6 is involved which means that during axial compression, the MPFEM system allows the radial loading paths to expand. The complementary work is a maximum for the SR-1/6 paths, and the closed die has lower values. Then bigger set of strain ratios is chosen to output Kirchoff stress until the strain ratio achieves 1. It means that the region of the contour of complementary work done is obtained from uniaxial loading paths with little radial expansion to the isostatic loading paths.

The contours of constant complementary work done per unit initial volume areas shown in Figure 7-3. The contours are created by picking same value of complementary work done in Kirchoff effective and hydrostatic stress under different compression. The points in Figure 7-3 show the analytical solution of empirical model developed below. Compared with the current density contours presented in Figure 7-2, a coherent group of convex contours can be obtained. It can be concluded that the deformation plasticity model is appropriate for a limit level of loading histories that are similar to those experienced under practical die compression operations (e.g. monotonically increasing loading), and the contours of constant complementary work done along different loading paths in strain space can be considered as good surfaces expression for the purpose of analysis.

An empirical model based on the data presented in Figure 7-3 was developed as follows. In the range from isostatic to closed die conditions, all principal strains are compressive. An implicit potential ψ can be defined as a quadratic function of the Kirchhoff stresses. This can lead the form of the expressions that are selected to describe the parameters of the ellipse equation as functions of the complementary work done per unit initial volume ($\bar{\Omega}_e$). Our aim is to determine a simple model that can describe the behaviour of the material and fit, if possible a single expression can for the whole range of data-points achieved from MPFEM. A practical model, which is given by this method, is fully described and calibrated below. The implicit potential ψ can be defined as (Cocks and Sinka, 2007):

$$\psi(\bar{\Omega}_e) = \left(\frac{T_{ke}}{B(\bar{\Omega}_e)}\right)^2 + \left(\frac{T_{kh} - C(\bar{\Omega}_e)}{A(\bar{\Omega}_e)}\right)^2 - 1 = 0 \tag{7-1}$$

Where $T_{ke}$ and $T_{kh}$ are the Kirchoff effective and hydrostatic stresses, $A(\bar{\Omega}_e)$, $B(\bar{\Omega}_e)$ and $C(\bar{\Omega}_e)$ are functions of complementary work done per unit initial volume. Based on known Kirchhoff effective stress and hydrostatic stress values from MPFEM, $A(\bar{\Omega}_e)$, $B(\bar{\Omega}_e)$ and $C(\bar{\Omega}_e)$ can be calculated by fitting equation (7-1).

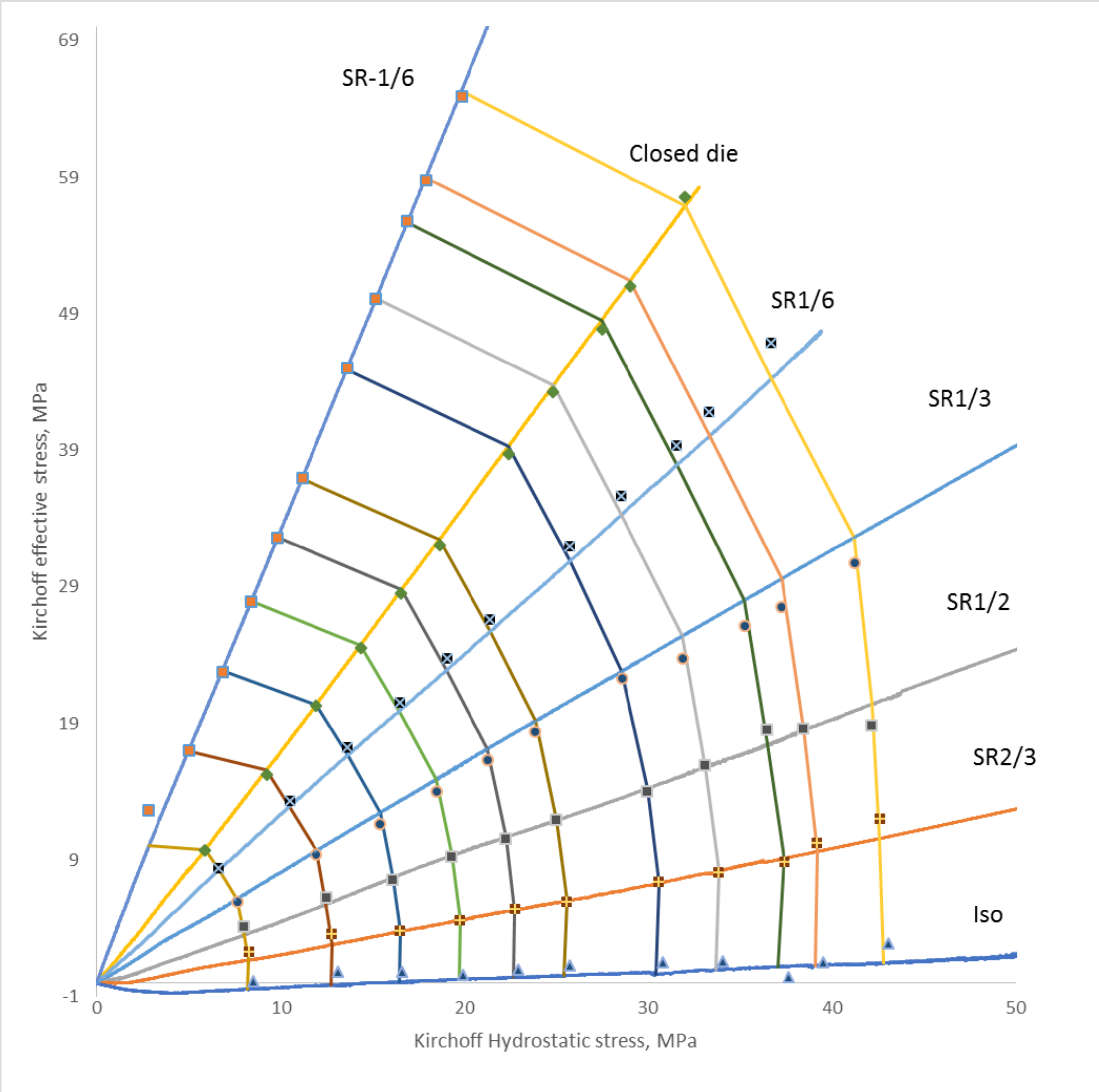


Figure 7-3 Contours of constant complementary work done ($MJm^{-3}$) per unit initial volume in Kirchhoff stress space

（contours - same complementary work done under Kirchhoff stress in MPFEM, lines - Kirchhoff stress in MPFEM and points - Kirchhoff stress fitted by equation 7-1）

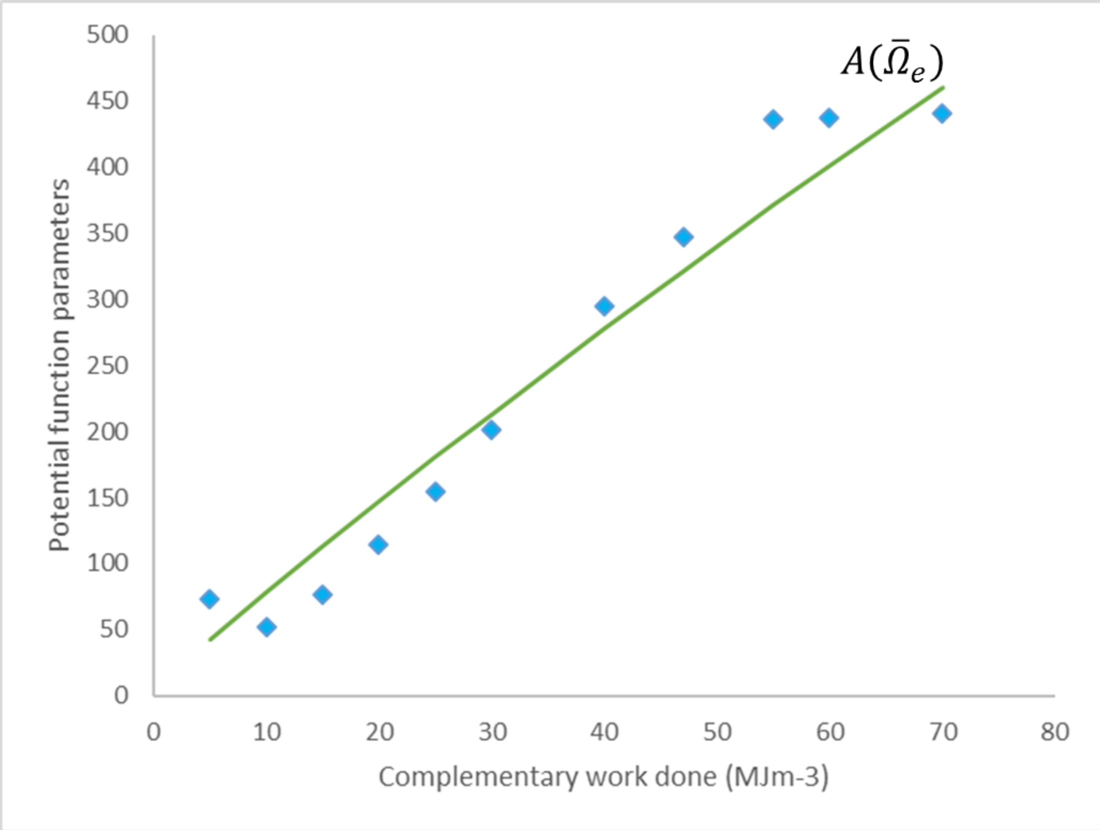

$A(\bar{\Omega}_e)$
Potential function parameters
Complementary work done (MJm-3)
0
50
100
150
200
250
300
350
400
450
500
0
10
20
30
40
50
60
70
80


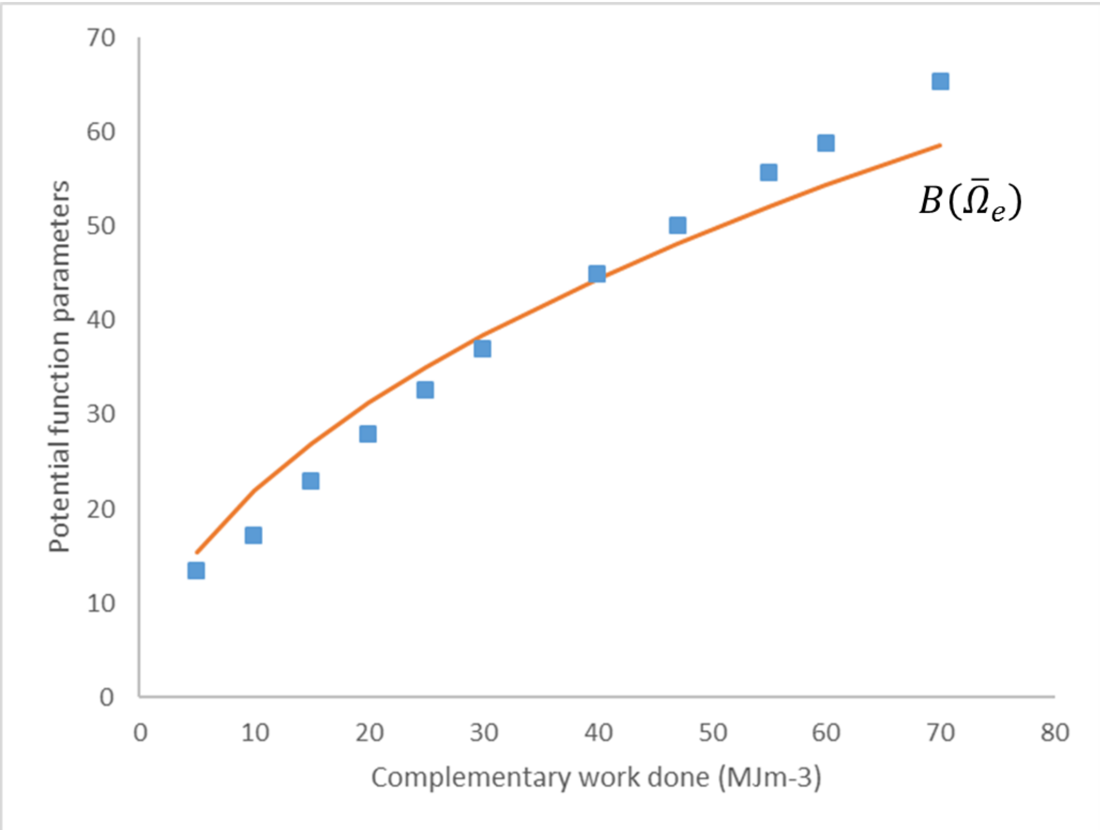

$B(\bar{\Omega}_e)$
Potential function parameters
Complementary work done (MJm-3)
0
10
20
30
40
50
60
70
0
10
20
30
40
50
60
70
80

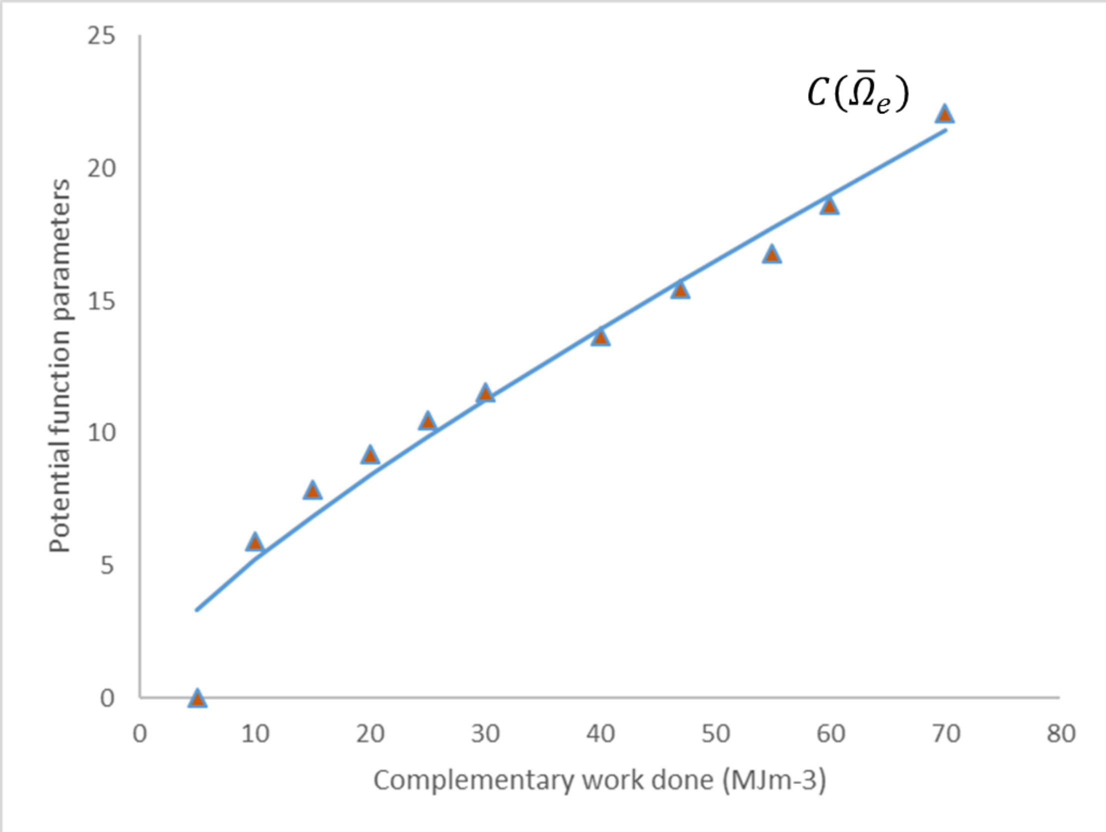


Figure 7-4 Model parameters as functions $A(\bar{\Omega}_e)$, $B(\bar{\Omega}_e)$ and $C(\bar{\Omega}_e)$ of complementary work done per unit initial volume

As shown above, the more detailed equations of functions $A(\bar{\Omega}_e)$, $B(\bar{\Omega}_e)$ and $C(\bar{\Omega}_e)$ are chosen to ensure consistency with the micromechanical framework (Cocks and Sinka, 2007). The simple expressions that satisfy these requirements are

$$B(\bar{\Omega}_e) = \frac{b_1 \bar{\Omega}_e^{\frac{1}{2}} + b_2 \bar{\Omega}_e}{1 + b_3 \bar{\Omega}_e} \tag{7-2}$$

$$A(\bar{\Omega}_e) = \frac{a_1 \bar{\Omega}_e^{\frac{1}{2}} + a_2 \bar{\Omega}_e}{1 + a_3 \bar{\Omega}_e} \tag{7-3}$$

$$C(\bar{\Omega}_e) = c_1 \bar{\Omega}_e^{\frac{1}{2}} + c_2 \bar{\Omega}_e \tag{7-4}$$

The method of fitting the model parameters is expressed as follows. The form of

Equation (7-2) is such that as $\bar{\Omega}_e \to \infty$, $B(\bar{\Omega}_e)$ asymptotes to a constant value $(b_2/b_3)$ which is determined by the yield strength of the material. As a reference, the previous research shows the hardness of the Microcrystalline cellulose using Nano-indentation (Gocedarica et al., 2011 and Krishnamachari, 2012). The yield strength of fully dense Microcrystalline cellulose is approximately 180 MPa, thus we have $b_2/b_3 = 90.9$. To obtain a good fit with the MPFEM data by Equation (7-1), we assume: $b_1 = 6.7, b_2 = 0.1$ and $b_3 = 0.0011$. And to achieve the value of $c_1$ and $c_2$, equation (7-4) is fitted to the MPFEM data and we obtain $c_1 = 1.097$ and $c_2 = 0.1747$.

Finally, the initial stress ratio is given by the micromechanical model for simulated closed condition is 1/3, so a relation between $A(\bar{\Omega}_e)$, $B(\bar{\Omega}_e)$ and $C(\bar{\Omega}_e)$ can be obtained (Cocks and Sinka, 2006)

$$3a_1^2R - 2b_1^2 - c_1R\sqrt{4b_1^2 + 9a_1^2} = 0 \tag{7-5}$$

Where R = 1.2 is the effective to hydrostatic stress ratio in Kirchhoff stress space which relates to a radial to axial stress ratio of 1/3 in Cauchy stress space according to the micromechanical model. From equation (7-5), $a_1$ is calculated as 4.5. Then fitting equation (7-3) to the MPFEM data gives $a_2 = 6.5$ and $a_3 = 0.001$.

## 7.3 Conclusions

Contours of constant density were generated, however, a consistent set of convex surfaces could not be obtained to the purpose of incremental plasticity model development using density as state variable. Contours of constant complementary work done in Kirchhoff stress space, however, were obtained and were described using a potential function with a good agreement. The model parameters were presented as the function of the complementary work done per unit initial volume. The model data and fitted parameters are shown in Figure 7-4. This model provides a good description of MPFEM results. Therefore, in the case of powder compaction loaded along different loading paths, the data can be organised by contours of constant complementary work done per unit initial volume of material using a suitable deformation plasticity model that can be developed.

# Chapter 8. Conclusions and future work

## 8.1 Overall conclusions

For the purpose of simulating powder compaction, an accurate constitutive law needs to be determined to describe the material response. A complete framework was developed to obtain numerical constitutive laws based on a single particle properties and a realistic packing arrangement. For the particle characterisation, the single particle breakage test was carried out to obtain material properties for the particles (e.g. Young's Modulus, Poisson' ratio and yield stress). A single particle compression model was validated against experimental data. Through these series of experimental measurements, numerical calculation and simulation, the parameters of single particle compression were used as input into the multi-particle model.

To achieve the practical particle shape and packing arrangement, X-ray CT techniques were used, and methods for importing and meshing the particulate assembly were developed.

A practical method was used to validate the multi-particle model using an instrumented die with radial stress sensors. The stress-strain curve during compaction was measured and the data were corrected for system compliance and frictional effects which introduce non-homogeneous stress state.

To develop a constitutive law for powder compaction MPFEM was used. The finite element analysis based model with discrete characteristics captured both the structural features of the realistic particles and the contact conditions between particles such as rotation, rearrangement and friction. Thus, the development of a MPFEM based on practical consideration made the analysis of particle compaction in a finite element environment more diversified, in a way which combined the advantages of DEM and FEM.

The deformation plasticity framework provided an appropriate structure to describe the material response during compaction. The stress states were determined along different loading paths in strain space. Contours of current density were not sufficiently consistent to offer a basis for constructing a constitutive model. However, in Kirchhoff stress space a coherent set of convex contours of constant complementary work done per unit initial volume were obtained. This model can be used for the class of loading histories relevant to practical die compression situations (e.g. monotonically increasing loading). The parameters of the complementary work functions were fully calibrated from numerical experiments.

## 8.2 Future work

In powder compaction, the material changes from loose powder into a dense compact. It is a complex process, especially for numerical modelling that builds up something very close to the practical conditions (e.g. particle shape, packing arrangement and particle strength). This thesis has well established a complete methodology, which combined X-ray CT technology with finite element simulation and studied the relationship between realistic particle properties and MPFEM. In order to optimise MPFEM to develop numerical constitutive laws the following two main areas require future work:

1. Hardening law

The hardening law plays a key role in improving the description of the plastic behaviour of the material. The single particle compression model is not sensitive to the details of the hardening law. A simplified MPFEM could be created for finding the hardening law.

2. Model convergence

The packing arrangement, particle contacts, and mesh directly affect mesh distortion and numerical convergence in MPFEM. This could be addressed by either improving the design of the initial mesh (e.g. the process of transferring data from X-ray CT to FEM) or by more suitable automatic remeshing techniques.

Last, but not least, the methodology developed in this work used a relatively large particle (0.8mm diameter). Real powders used in pharmaceuticals, food, detergents and other powder processing industries have significantly smaller particle size and considerably more complex shape. Consideration of such particles requires improved X-ray CT characterisation of packing arrangement, experimental characterisation of mechanical properties and interactions between particles, improved MPFEM technology and significantly higher computational power.

## References

ABAQUS, 2006. ABAQUS 6.6 Theory Manual. ABAQUS Inc.

Adams, M. J., Mckeown, R. and Whall, A., 1997. A micromechanical model for the confined uniaxial compression of an assembly of elastically deformation spherical particles, J. Phys. D. Appl. Phys. 30 (1997) 912-920.

Akisanya, A.R., Cocks, A.C.F. and Fleck, N.A., 1994. Hydrostatic compaction of cylindrical particles. Journal of the Mechanics and Physics of Solids, Vol. 42, iss. 7, pp. 1067–1085.

Allied Chemicals & PharmaCeuticals Pvt. Ltd. 2013. *Company profile*. Available online at: http://www.eqfscertification.com/members.php?id=532

Ansari, M. A. and ˇStepánek, F. (2006b). Formation of hollow core granules by fluid bed in situ melt granulation: Modelling and experiments. International Journal of Pharmaceutics, 321, 108-116.

Artz, E., 1982. Influence of an increasing particle coordination on the densification of spherical powders. Acta Materiall, Vol. 30, pp. 1883–1890.

Asaro, R. J., 1983. Micromechanics of crystals and polycrystals. Adv. Appl. Mech. 23, 1-115.

Ben Aim R. and Le Goff, P., 1968. La Coordinance des Empilements Desordonnes de Spheres. Application aux Melanges Binaires de Sphere. Powder Technology, Vol. 2, pp. 102.

Betson, M., Barker, J., Barnes, P., Atkinson, T. and Jupe, A. (2004). Porosity imaging in porous media using synchrotron tomographic techniques. Transport in Porous Media, 57, 203-214.

Bier W., Dariel M. P., Frage N., Hartmann S. and Michailov O., 2007. Die compaction of copper powder designed for material parameter identification. International Journal of Mechanical Sciences. Vol. 49, pp. 766-777.

Briscoe, B.J. and Rough, S.L., 1998. The effect of wall friction on the ejection of pressed ceramic parts. Powder Technology. Vol. 99, pp. 228-233.

Budiansky, B., 1959. A reassessment of deformation theory of plasticity. J. Appl. Mech. 26, 259-264.

Burch, S.F., 2001a. Measurement of density variations in compacted parts using X-ray computed tomography. In: Proceedings of EuroPM2001, Nice, France, October 22–24, pp. 398–404.

Burch, S.F., 2001b. X-ray computerised tomography for quantitative measurement of density variations in materials. Insight 43, 29–31.

Busignies, V., Leclerc, B., Porion, P., Evesque, P., Couarraze, G., & Tchoreloff, P. (2006). Quantitative measurements of localized density variations in cylindrical tablets using X-ray microtomograghy. European Journal of Pharmaceutics and Biopharmaceutics, 64, 38-50.

Caligaris, R.E., Topolevsky, R., Maggi, P., & Brog F. 1985. Compaction behaviour of ceramic powders, Powder Technology, 42, 263-267.

Chaboche, J-L., 1993. Cyclic viscoplastic constitutive equations: a thermodynamically consistent formulation. J. Appl. Mech. 60, 813-821.

Chester, A. W., Kowalski, J. A., Coles, M. E., Muegge, E. L., Muzzio, F. J. and Brone, D. 1999. Mixing dynamics in catalyst impregnation in double-cone blenders. Powder Technology, 102, 85-94.

Cocks, A. C. F. and Sinka, I. C., 2007. Constitutive modelling of powder compaction-I. Theoretical concepts. Mechanics of Materials 39, 392-403.

Cocks, A. C. F., 2002. The constitutive behaviour of particulate materials: models for compaction and ejection. In: Lawley, A., Smugeresky, J.E. (Eds), Process modelling in powder metallurgy and Particulate Materials. MPIF, Princeton, NJ.

Coube O. and Riedel H., 2000. Numerical simulation of metal powder die compaction with special consideration of cracking. Powder Metallurgy. Vol. 43(2), pp. 123-131.

Coube O., 1998. Modelling and numerical simulation of powder die compaction with consideration of cracking. PhD thesis, University Pierre et Marie Curie, Paris.

Cumberland, D.J. and Crawford, R.J., 1987. *The packing of particles*. Amsterdam: Elsevier Science

Cundall, P.A. and Strack, O.D.L., 1979. A discrete numerical model for granular assemblies. Geotechnique. Vol. 29, no. 1, pp. 47-65.

Cunningham, J.C., Sinka, I.C. and Zavaliangos, A., 2004. Analysis of tablet compaction. Part 1 – Characterisation of mechanical behaviour of powder and powder/tooling friction. Journal of Pharmaceutical Sciences. Vol. 93, no. 8, pp. 2022-2039.

Diarra H., Mazel V., Boillon A., Rehault L., Busignies V., Bureau S. and Tchoreloff P., 2012. Finite element method modelling of the powder compaction of cosmetic products: comparison between simulated and experimental results. Powder Technology. v 224 ( 2012) 233-240.

Dimaggio F. L. and Sandler I. S., 1971. Material models for granular soils. ASCE Journal of engineering Mechanics. Vol. 97, pp. 935.

Dintwa, E., Tijskens, E. and Ramon, H., 2007. On the accuracy of the Hertz model to describe the normal contact of soft elastic spheres. In H.J. Herrmann(ed.), Granular Matter, Vol. 10, Iss. 3, pp. 209-221.

Djuri, M., Marinkovi-Neduin, R., Ranogajec, J., & Radeka, M. (1995). Particle size range as a factor influencing compressibility of ceramic powder, Ceramics International, 21, 227-230.

Donzé, F.V., Richefeu, V. and Magnier, S.-A., 2009. State of the art of geotechnical engineering, electronic journal of geotechnical engineering, Advances in Discrete Element Method Applied to Soil, Rock and Concrete Mechanics. Electronic Journal of Geotechnical Engineering. pp. 1–44.

Doremus, P., Geindreau, C., Martin, A., Debove, L., Lecot, R. and Dao, M., 1995. High pressure triaxial cell for metal powder. Powder Metallurgy. Vol. 38, pp. 284-287.

Drucker, D.C. and Prager, W., 1952. Soil mechanics and plastic analysis or limit design. Quarterly Applied Mechanics. Vol. 10, pp. 157-165.

Ernst, E., Thummler, F., Beiss, P., Wahling R. and Arnhold, V., 1991. Friction measurements during powder compaction. Powder Metallurgy International. Vol.23, no.2, pp. 77-84.

Fischmeister, H. F and Arzt, E., 1983. Densification of powders by particle deformation, Powder Metall, 26 (1983) 82-88.

Fleck, N.A., 1995. On the cold compaction of powders. Journal of the Mechanics and Physics of Solids. Vol. 43, no. 9, pp. 1409-1431.

Fleck, N. A, Storakers, B., McMeeking, R. M., 1997. The viscoplastic compaction of powders. In: Fleck, N. A., Cocks, A. C. F. (Eds.), Mechanics of Granular and Porous Materials. Kluwer, pp. 1-10.

Frangin, E., Martin, P. and Daudeville L., 2006. On the use of combined finite/discrete element method for impacted concrete structures. J. Phys. IV France. Vol.134, pp. 461-466.

Frenning, G., Nordström, J., & Alderborn, G. (2009). Effective Kawakita parameters for binary mixtures, Powder Technology, 189, 270-275.

Gan, K. & Gu, M. (2008). The compressibility of Cu/SiCp powder prepared by high-energy ball milling, Journal of Materials Processing Technology, 199, 173-177.

Gens, A. and Potts, D.M., 1988. Critical state models in computational geomechanics. Engineering Computation. Vol. 5, pp. 178–197.

Golchert, D. J., Moreno, R., Ghadiri, M. and Litster, J. (2004). Effect of granule morphology on breakage behaviour during compression. Powder Technology, 143-144, 84-96.

Golchert, D. J., Moreno, R., Ghadiri, M., Litster, J. and Williams, R. (2004). Application of X-ray microtomography to numerical simulation of agglomerate breakage by distinct element method. Advanced Powder Technology, 15, 447-457.

Govedaruca, B., Skarabot. M, Llic. L, Planinsek. O, Musevic. I and Srcic. S., 2011. Mapping the local elastic properties of pharmaceutical solids using atomic force microscopy. Procedia Engineering 10 (2011) 2857-2866.

Govindarajan R. M. and Aravas N., 1994. Deformation processing of metal powders: Part 1-Cold isostatic pressing. International Journal of Mechanical Sciences. Vol. 36, pp. 343-357.

Gregory, D. and Newton, I. S., 1694. Letter from David Gregory to Isaac Newton. Corr. IV, pp. 20-21, n.472.

Gurson, A.L., 1977. Continuum theory of ductile rupture by void nucleation and growth: part I, yield criteria and flow rules for porous ductile media. Journal of Engineering Material and Technology. Transactions of the ASME. Vol. 99, pp. 2–15.

Guyoncourt, D.M.M., Tweed, J.H., Gough, A., Dawson, J. and Pater, L., 2001. Constitutive data and friction measur ements of powders using instrumented-die. Powder Metallurgy. Vol. 44, pp. 25-33.

Han L. H., Elliott J. A., Bentham A. C., Mills A., Amidon G. E., Hancock B. C., 2008. A modified Drucker-Prager Cap model for die compaction simulation of pharmaceutical powders. International Journal of Solids Structure. Vol. 45, pp. 3088-3106.

Harthong, B., Jerier, J.-F., Dorémus, P., Imbault, D., Donzé, F.-V., 2009. Modeling of highdensity compaction of granular materials by the discrete element method. International Journal of Solids and Structures. Vol. 46, pp. 3357–3364.

Hasting, J. K., Juds, M. A. and Brauer, J. R., 1985. Accuracy and economy of finite element magnetic analysis. 33rd Annual National Relay Conference.

Helle, A. S., Easterling, K. E., Ashby, M. F., 1985. Hot-isostatic pressing diagrams: new developments. Acta Metall. 33 (12), 2163-2174.

Hertz, H., 1895. "Über die Berührung fester elastischer Körper," Gesammelte Werke (P. Lenard, ed.), Bd. 1, (J.A. Barth, Leipzig,) pp. 155-173.

Heukamp, F.H., Ulm, F-J. and Germaine, J.T., 2003. Poroplastic properties of calcium-leached cement-based materials. Cement and Concrete Research. Vol. 33, iss. 8, pp. 1155-1173.

Heyliger, P.R., 2013. Adaptive Materials and Nanotube Mechanics. Available online at: [http://spacegrant.engr.colostate.edu/projects/archive/pre2003/Recent/Adaptive%20Materials/Index.htm](http://spacegrant.engr.colostate.edu/projects/archive/pre2003/Recent/Adaptive%20Materials/Index.htm)

Hibbitt, Karlsson & Sorensen, 1998. ABAQUS Theory Manual Version 5.8, Hibbitt, Karlsson & Sorensen, Inc., Pawtucket, RI.

Hill, R., 1950. The Mathematical Theory of Plasticity. Oxford University Press, Oxford.

Hill, R., Storåkers, B. and Zdunek, A.B., 1989. A theoretical study of the brinell hardness test, Royal Society of London Proceedings Series A. Vol. 423, pp. 301–330.

Huang, F., An, X., Zhang, Y. abd Yu A. B., 2017. Multi-particle FEM simulation of 2D compaction on binary AL/SiC composite powders. Powder Technology 317 (2017) 39-48.

Hutchinson, J. W., 1974. Plastic buckling. Adv. Appl. Mech. 14, 67-144.

James, J. F., 1977. Particle deformation during cold isostatic pressing of metal powders, Powder Metallurgy. 20, 199-204.

Jerier, J.-F., Hathong, B., Richefeu, V., Chareyre, B., Imbault, D., Donze, F.-V. and Doremus, P., 2011. Study of cold powder compaction by using the discrete element method. Powder Technology. Vol. 208, pp. 537–541.

Jia, X., Caulkin, R., Fairweather, M. and Williams, R. A. (2007). A novel approach to predicting the behaviour of arbitrary particulate mixture under vibration. In 17th European symposium on computer aided process engineering (ESCAPE 17) Bucharest, Romania.

Jia, X. and William, R. A. (2006). From microstructure of tablets and granules to their dissolution behaviour. Dissolution Technology, 13, 11-12.

Jia, X. and Williams, R. A. (2007). A hybrid mesoscale modelling approach to dissolution of granules and tablets. Chemical Engineering Research & Design, 85, 1027-1038.

Johansson, B., Nicklasson, F. and Alderborn, 1998. Effect of pellet size on degree of deformation and densification during compression and on compactibility of microcrystalline cellulose pellets, Int. J. Pharm. 163 35-48.

Johnson, K.L., 1985. *Contact Mechanics*, Cambridge: Cambridge University Press.

Jonsson, H and Frenning, G., 2016. Investifations of single microcrystalline cellulose-based granules subjected to confined triaxial compression. Powder Technology 289, 79-87.

Kai, T., Misawa, M., Takahashi, T., Tiseanu, I. and Ichikawa, N. (2005). Analysis of the structure of catalyst layers around bubbles in a fluidized catalyst bed. In 4$^{th}$ world congress on industrial process tomography Aizu, Japan, (pp. 794-799).

Kak, A. C., 1979. Computerized tomography with X-ray, emission and ultrasound sources. Proc. IEEE 67, 1245-1272.

Karpyn, Z. T. and Piri, M. (2007). Prediction of fluid occupancy in fractures using network modelling and X-ray microtomography. I. Data conditioning and model description. Physical Review E, 76, 016315.

Kim, H.S., Oh, S.T. and Lee, J.S., 2002. Constitutive model for cold compaction of ceramic powder. Journal of the American Ceramic Society. Vol. 85, pp. 2137-2138.

King ceramic industry, 2012. *Products.* Available online at:
http://www.qrbiz.com/product/553552/zirconia-ceramic-parts.html

Kingman, J.F.C., 1965. Book Review on Packing and Covering. Nature. Vol. 205, p. 738.

Klevan, I., Nordström, J., Bauer-Brandl, A., & Alderborn, G. (2009). On the physical interpretation of the initial bending of a Shapiro–Konopicky–Heckel compression profile, European Journal of Pharmaceutics and Biopharmaceutics, 71, 395-401.

Klevan, I., Nordström, J., Tho, I., & Alderborn, G. (2010). A statistical approach to evaluate the potential use of compression parameters for classification of pharmaceutical powder materials, European Journal of Pharmaceutics and Biopharmaceutics, 75, 425-435.

Koerner, R.M., 1971. Triaxial compaction of metal powders. Powder Metallurgy International. Vol. 3, no. 4, pp.186-188.

Kozicki, J. and Donze, F.V., 2008. A new open-source software developed for numerical simulations using discrete modeling methods. Computer Methods in Applied Mechanics and Engineering. Vol. 197, iss. 49-50, pp. 4429-4443.

Krishnamachari. P, Hashaikeh. R, Chiesa. M and Gad el rab. K. R. M, 2012. Effects of acid hydrolysis time on cellulose nanocrystals properties: nanaoindentation and thermogravimetric study. Cellulose Chem. Technol., 46(1-2), 13-18 (2012).

Kruggel-Emden, H., Wirtz, S. and Scherer, V., 2008. A study on tangential force laws applicable to the discrete element method (DEM) for materials with viscoelastic or plastic behaviour[J]. Chemical Engineering Science. Vol, 63, pp. 1523-1541.

Le Goff, P., Leclerc D. and Dodds, J., 1985. The structure of packed Beds: Continuity of Research in Nancy and Some New Results. Powder Technology. Vol. 42, pp. 47-53.

Leonard, A., Blacher, S., Marchot, P., Pirard, J. P. and Crine, M. (2003). Moisture profiles determination during convective drying using X-ray microtomography. In Proceedings of the 3rd world congress on industrial process tomography Banff, Canada, (pp. 730-735).

Li, X., Lin, C. L., Miller, J. D. and Johnson, W. P. (2006). Pore-scale observation of microsphere deposition at grain-to-grain contacts over assemblage-scale porous media domains using X-ray microtomograghy. Environmental Science and Technology, 40, 3762-3768.

Lin, C. L., Miller, J. D. and Cortes, A. B. (1992). Application of X-ray computed tomography in particulate systems. KONA, 10, 88-95.

Lin, C. L. and Miller, J. D. (2001). A new cone beam X-ray microtomography facility for 3D analysis of multiphase materials. In The 2nd world congress on process tomography Hannover, Germany, (pp. 98-109).

Lin, C. L. and Miller, J. D. (2004). Pore structure analysis of particle beds for fluid transport simulation during filtration. International Journal of Mineral Processing, 73, 281-294.

Lu, S., Landis, E. N. and Keane, D. T. (2006). X-ray microtomography studies of pore structure and permeability in Portland cement concrete. Materials and Structures, 39, 611-620.

Martin, C.L., 2004. Elasticity fracture and yielding of cold compacted metal powders. Journal of the Mechanics and Physics of Solids. Vol. 52, pp. 1691–1717.

Martin, C.L., Bouvard, D. and Shima, S., 2003. Study of particle rearrangement during powder compaction by the DEM. Journal of the Mechanics and Physics of Solids. Vol. 51, pp. 667–693.

McDonogh, R.M., Fane, A.G., Fell C.J.D. and Flemming, H.C., 1998. The influence of polydispersity on the hydraulic behaviour of colloidal fouling layers on membranes:

Perturbations on the behaviour of the “idea” colloidal layer. Colloids and Surfaces A: Physicochemical and Engineering Aspects. Vol. 138, Iss. 2-3, pp. 231-244.

McDowell, G. R., 2002. On the yielding and plastic compression of sand. Soils Found. 42, No.1, 139-145.

Mesarovic, S., Fleck, N., 2000. Frictionless indentation of dissimilar elastic-plastic spheres. Int. J. Solids struct. 37, 7071-7091.

Mersereau, R. M., 1974. Digital reconstruction of multidimensional signals from their projections. Proc. IEEE 62, 1319-1338.

Michrafy, A., Ringenbacher, D., & Tchoreloff, P. (2002). Modelling the compaction behaviour of powders: application to pharmaceutical powders, Powder Technology, 127, 257-266.

Miller, J. D., Lin, C. L. and Cortes, A. B. (1990). A review of X-ray computed tomography and its applications in mineral processing. Mineral Processing and Extracting Metallurgic Review, 7, 1-18.

Mitra B., Hilden J. and Litster J. D., 2016. Effects of the granule composition on the compaction behaviour of deformable dry granules. Powder Technology, 291. 00. 487-498.

Mroz, Z., 1967. On the description of anisotropic work hardening. J. Mech. Phys. Solids 15, 163.

Mueth, D. M., Debregeas, G. F., Karczmar, G. S., Eng, P. J., Nagel, S. R., and Jaeger, H. M. (2000). Signatures of granular microstructure in dense shear flows. Nature, 406, 385-

389.

Nakashima, Y. and Watanabe, Y. (2002). Estimate of transport properties of porous media microfocus X-ray computed tomography and random walk simulation. Water Resources Research. 38. 1272.

Nakata, Y., Hyde, A. F. L., Hyodo, M. and Murata, H., 1999. A probabilistic approach to sand particle crushing in the triaxial test. Geotechnique 49, No. 5, 567-583.

Nikolenko, A.N. and Kovalchenko, M.S., 1985. Analysis of the Random Packing of Identical Particles II. Structural Characteristics of the Packing of Disk on a Plane Surface. Soviet Powder Metallurgy and Metal Ceramics. Vol. 24, pp. 912-914.

Oda, M., Konishi, J. and Nemat-Nasser, S., 1982. Experimental micromechanical evaluation of the strength of granular materials: effect of particle rolling. In: Jenkins, J.T., Satake, M. (Eds.), Mechanics of Granular Materials: New Models and Constitutive Relations. Elsevier, Amsterdam, pp. 21-30.

Oda, M., Iwashita, K., 2000. Study on couple stress and shear band development in granular materials based on numerical simulation studies. Int. J. Eng. Sci. 38, 1713.

Olson, J. F. and Rothman, D. H. (1997). Two-fluid flow in sedimentary rock: Simulation, transport and complexity. Journal of Fluid Mechanics, 341, 343-370.

Orlov, I. M., Morgan, D. G. & Cheng, R. H. (2006). Efficient implementation of a filtered back-projection algorithm using a voxel-by-voxel approach. Journal of Structure Biology, 154, 287-296.

Phillips, D. H., Lannutti, J. J., 1997. Measuring physical density with X-ray computed tomography. NDT&E Int. 30, 339-350.

Phillips, A., Lu, W. Y., 1984. An experimental investigation of yield surfaces and loading surfaces of pure aluminium with stress-controlled and strain-controlled loading paths. J. Eng. Mat. Tech. 106, 349-354.

PM Modnet Computer Modelling Group, 1999. Comparison of computer models representing powder compaction process. Powder Metallurgy. Vol. 42, pp. 301-311.

PM Modenet Research Group, 2002. Numerical simulation of powder-compaction for two multilevel ferrous parts, including powder characterisation and experimental validation. Powder Metallurgy. Vol. 45, pp. 335-334.

Ponter, A. R. S., Martin, J. B., 1972. Some external properties and energy theorems for inelastic materials and their relationship to the deformation theory of plasticity. J. Mech. Phys. Solids 20, 281-300.

Procopio, A.T. and Zavaliangos, A., 2005. Simulation of multi-axial compaction of granular media from loose to high relative densities. Journal of the Mechanics and Physics of Solid. Vol. 53, pp. 1523-1551.

Procopio, A.T., Zavaliangos, A. and Cunningham, J.C., 2003. Analysis of the diametrical compression test and the applicability to plastically deforming materials. Journal of Materials Science. Vol. 38, pp. 3629-3639.

Ramakrishnan, K.N., Nagarajan, R., RamaRao G.V., & Venkadesan, S. (1997). A compaction study on ceramic powders, Materials Letters, 33, 191-194.

Ransing, R.S., Gethin, G.T., Khoei, A.R., Mosbah P. and Lewis, R.W., 2000. Powder compaction modelling via the discrete and finite element method. Materials & Design. Vol. 21, iss. 4, pp. 263–269.

Redanz, P., Fleck, N. A., 2001. The compaction of a random distribution of metal cylinders by the discrete element method. Acta Mater. 49, 4325.

Reddy, J. N., 2006. An introduction to the finite element method (Thirded.). McGraw-Hill.

Ridgway, K. and Tarbuck, K.J., 1967. The Random packing of spheres. British Chemical Engineering. Vol. 12, pp. 384-388.

Rogers, C.A., 1958. The Packing of Equal Spheres. Proceedings of the London Mathematical Society. Vol. 8, ser. 3, pp. 609-620.

Rogers, C.A., 1964. Packing and Covering. London: Cambridge University Press.

Rumpf, H. and Gupte, A. R., 1975. The influence of porosity and grain size distribution on the permeability equation of porous flow. Chemie Ing. Techn. (Weinheim) 43(6), 367-375

Samimi, A., Hassanpour, A., & Ghadiri, M. (2005). Single and bulk compressions of soft granules: Experimental study and DEM evaluation, Chemical Engineering Science, 60, 3993-4004.

Schneider, L.C.R., 2003. Compaction and yield behaviour of particulate materials. PhD thesis, University of Leicester, UK.

Schofield, A. and Wroth, C.P., 1968. Critical State Soil Mechanics. London: McGraw-Hill.

Selomulya, C., Tran, T. M., Jia, X. and Williams, R. A. (2006). An integrated methodology to evaluate permeability from measure microstructures. AlChE Journal, 52, 3394-3400

Shang, C., 2012. Modelling powder compaction and breakage of compacts. Unpublished PhD thesis, University of Leicester, UK.

Shyamala, B. and Lakshmi, P. K., 2010. Extrusion spheronization-a review. International Journal of PharmTech Research. Vol. 2, No. 4, pp 2429-2433.

Simo, J.C. and Hughes, T.J.R., 1998. Computational Inelasticity, New York: Springer.

Sinka, I.C., Cunningham, J.C., Zavaliangos, A., 2003. The effect of wall friction in the compaction of pharmaceutical tablets with curved faces: a validation study of the Drucker-Prager cap model. Powder Technology. Vol. 133, iss. 1-3, pp. 33–43.

Sinka, I.C., Cunningham, J.C., Zavaliangos, A., 2004a. Analysis of tablet compaction. II. Finite element analysis of density distributions in convex tablets. Journal of Pharmaceutical Sciences. Vol. 93, iss. 8, pp. 2040–2053.

Sinka, I.C., Motazedian, F., Cocks, A.C.F. and Pitt, K.G., 2009. The effect of processing parameters on pharmaceutical tablet properties. Powder Technology. Vol. 189, pp. 276-284.

Sivasankaran, S., Sivaprasad, K., Narayanasamy, & R., Iyer, V.K. (2010). An investigation on flowability and compressibility of AA 6061100 − x-x wt.% TiO2 micro and nanocomposite powder prepared by blending and mechanical, alloying, Powder Technology, 201, 70-82.

Sloane, N.J.A., 1984. The packing of spheres. Scientific American. Vol.250, no.1, pp. 116-125.

Smith, C.S., 1953. Further notes on the shape of metal grains: space-filling polyhedral with unlimited sharing of corners and faces. Acta Metallurgica. Vol. 1, pp. 295-300.

Spanne, P., Thovert, J. F., Jacquin, C. J., Lindquist, W. B., Jones, K. W. and Adler, P. M. (1994). Synchrotron computed microtomography of porous meida: Topology and transports. Physical Review Letters, 73 (14), 2001-2004.

Stasiak, M., Tomas, J., Molenda, M., Rusinek, R., & Mueller, P. (2010). Uniaxial compaction behaviour and elasticity of cohesive powders, Powder Technology, 203, 482-488.

Storåkers, B., Biwa, S. and Larsson, P.-L., 1997. Similarity analysis of inelastic contact. International Journal of Solids and Structures. Vol. 34, pp. 3061–3083.

Storakers, B., Fleck, N. A., McMeeking, R. M., 1999. The viscoplastic compaction of composite powders. J. Mech. Phys. Solids 47, 785-815.

Strang, G. and George, F., 1973. An analysis of the finite element method. Prentice Hall.

Sukop, M. C., Huang, H., Lin, C. L., Deo, M. D., Oh, k. and Miller, J.D. (2008). Distribution of multiphase fluids in porous meids: Comparison between lattice Boltzmann modelling and micro-X-ray tomography. Physical Review E, 77, 026710.

Sun X. K. and Kim K. T., 2013. Simulation of cold die compaction densification behaviour of iron and copper powders by Cam-clay model. Powder Metallurgy. Volume

40. 193-195.

Thornton, C. and Antony, S.J., 1998. Quasi-static deformation of particulate media, Philosophical Transactions Royal Society Mathematical. Physical and Engineering Sciences. Vol. 356, pp. 2763–2782.

Timoshenko, S and Goodier,J.N., 1970. Theory of elasticity. McGraw-Hill Book Company, Inc

Torre, C., 1948. Berg-Huttenmann. Monatsh. Montan. Hochschule leoben 93, 62.

Trasorras, J.R.L, Parameswaran R. and Cocks, A.C.F., 1998. Mechanical behavior of metal powders and compaction modeling. ASM Handbook, Powder Metal Technologies and Applications. ASM International. Vol. 7, pp. 326-342.

Tsuji, Y., Tanaka, T. and Ishida, T., 1992. Lagrangian numerical simulation of plug flow of cohesionless particles in a horizontal pipe[J]. Powder Technology. Vol. 71, pp.239-250.

Turenne S., Godere C., Thomas Y. and Mongeon P. E, 1999. Evaluation of friction conditions in powder-compaction for admixed and die-wall lubrication. Powder Metallurgy. Vol. 42, pp. 263-268.

Turner M., Clough R. W., Martin H.C. and Topp L. J., 1956. Stiffness and deflection analysis of complex structures. J. Aeronaut. Sci. 23(9), pp. 805-823.

Tvergaard, V., 1981. Influence of voids on shear band instabilities under plane strain condition. International Journal of Fracture Mechanics. Vol. 17, pp. 389-407.

Tvergaard, V. and Needleman, A., 1984. Analysis of the cup-cone fracture in a round tensile bar. Acta Metall. Vol. 32, pp.157-169.

Tvergaard, V., 1990. Material failure by void growth to coalescence. Adv. Appl. Mech. 27, 83-151.

Vogel, H-J., Tolke, J., Schulz, V. P., Krafczyk, M. and Roth, K. (2005). Comparison of a Lattice-Boltzmann capillary pressure-saturation relationships. Vadose Zone Journal, 4, 380-388.

Vogler, T.J., Lee, M.Y., & Grady, D.E. (2007). Static and dynamic compaction of ceramic powders, International Journal of Solids and Structures, 44, 636-658.

Watson, T.J. and Wert, J.A., 1993. On the development of constitutive relations for metallic powders. Metallurgical Transactions A. Vol. 24A, pp. 2071-2081.

Whelan, P. M. and Hodgeson, M. J., 1978. Essential principles of Physics. 2nd Edition

Wikman, B., Solimannezhad, H., Larsson, R., Oldenburg, M. and Haggblad, H.A., 2000. Wall friction coefficient estimation through modelling of powder die pressing Experiment. Powder Metallurgy. Vol. 43, pp. 132-138.

Wildenschild, D., Hopmans, J. W., Vaz, C. M. P., Rivers, M.L., Rikard, D. and Christensen, B. S. B. (2002). Using X-ray computed tomography in Hydrology: Systems, resolutions and limitations. Journal of Hydrology, 267, 285-297.

Wong, P., 1999. Methods of the physics of porous media San Diego: Academic Press.

Wornyoh, E. Y. A., Jasti, V. K. and Higgs, C. F., 2007. A review of dry particulate lubrication: powder and granular materials. Journal of Tribology, Vol. 129.

Wu, B.L., 2005a. Compaction properties of sand-bentonite buffer materials in nuclear waste disposal concept. PhD thesis, National Central University, Taiwan.

Wu C. Y. and Cocks, A.C.F., 2006. Numerical and experimental investigations of the flow of powder into a confined space. Mechanics of Materials. Vol. 38, iss. 4, pp. 304-324.

Wu, C.Y., Cocks, A.C.F. and Gillia, O.T., 2003. Die filling and power transfer. International Journal of Powder Metallurgy. Vol. 39, pp. 51–64.

Wu, C.Y., Dihoru, L. and Cocks, A.C.F., 2003. The flow of powder into simple and stepped dies. Powder Technology. Vol. 134, pp. 24-39.

Wu, C.Y., Hancock, B.C., Mills, A., Bentham, A.C., Best, S.M. and Elliott, J.A., 2008. Numerical and experimental investigation of capping mechanisms during pharmaceutical tablet compaction. Powder Technology. Vol. 181, pp. 121–129.

Wu, W., Jiang, G., Wagoner, R.H. and Daehn, G.S., 2000. Experimental and numerical investigation of idealized consolidation: Part 1: Static compaction. Acta Materialia. Vol. 48, iss. 17, pp. 4323–4330.

Wu, C.Y., Ruddy, O.M., Bentham, A.C., Hancock, B.C., Best, S.M., Elliott, J.A., 2005. Modelling the mechanical behaviour of pharmaceutical powders during compaction. Powder Technology. Vol. 152, iss. 1–3, pp. 107–117.

Yang, C. Y. and Fu, X. Y. (2004). Development and validation of a material-labeling method for powder process characterization using X-ray computed tomography. Powder Technology, 146, 10-19.

Yap, S.F., Adams, M.J., Seville, J.P.K., & Zhang, Z. (2008). Single and bulk compression of pharmaceutical excipients: Evaluation of mechanical properties, Powder Technology, 185, 1-10.

Yu, H.S., 1998. CASM: a unified state parameter model for clay and sand. International Journal for Numerical and Analytical Methods in Geomechanics. Vol. 22, iss. 8, pp. 621–653.

Zhang, Z., Seville, J.P.K. , Adams, M., & Yap, S.F. (2006). Understanding the mechanical properties of single microparticles and their compaction behaviour, China Particuology, 4, 35-40.

Zhou, M., Huang, S., Hu, J., Lei, Y. and Zou, F., 2017. A density-dependent modified Drucker-Prager Cap model for die compaction of Ag57.6-Cu22.4-Sn10-Ln10 Mixed metal powders. Powder Technology 2017 v.305 pp. 183-196.

# Appendix

| Test type | Hydrostatic stress, MPa | Effective stress, MPa | Kirchoff hydrostatic stress, MPa | Kirchoff effective stress, MPa | CWD per initial vol., MJ m$^{-3}$ | Current density, kg m$^{-3}$ |
|---|---|---|---|---|---|---|
| SR -1/6 | 6.86 | 14.146 | 2.841 | 10.048 | 5.0059 | 947.51 |
| Closed die | 8.106 | 15.101 | 5.905 | 9.736 | 5.007 | 1015.550 |
| SR 1/6 | 10.440 | 12.987 | 6.642 | 8.263 | 5.008 | 1057.782 |
| SR 1/3 | 12.317 | 9.921 | 7.645 | 6.158 | 5.007 | 1084.280 |
| SR 1/2 | 13.188 | 5.263 | 8.022 | 3.495 | 5.004 | 1106.470 |
| SR 2/3 | 13.622 | 2.739 | 8.266 | 1.662 | 5.004 | 1109.130 |
| Iso | 13.600 | 1.158 | 8.183 | 0.490 | 5.005 | 1118.511 |

| Test type | Hydrostatic stress, MPa | Effective stress, MPa | Kirchhoff hydrostatic stress, MPa | Kirchhoff effective stress, MPa | CWD per initial vol., MJ $m^{-3}$ | Current density, kg $m^{-3}$ | Line |
|---|---|---|---|---|---|---|---|
| SR -1/6 | 11.489 | 25.64 | 5.017 | 17.002 | 10.001 | 1014.954 | 1 |
| Closed die | 15.218 | 26.112 | 9.241 | 15.574 | 10.003 | 1108.344 | 2 |
| SR 1/6 | 18.124 | 22.316 | 10.489 | 12.916 | 10.010 | 1162.832 | 3 |
| SR 1/3 | 21.165 | 17.162 | 11.942 | 9.684 | 10.009 | 1192.749 | 4 |
| SR 1/2 | 22.603 | 9.542 | 12.498 | 5.761 | 10.011 | 1217.112 | 5 |
| SR 2/3 | 23.335 | 5.079 | 12.800 | 2.786 | 10.001 | 1226.844 | 6 |
| Iso | 23.401 | 0.947 | 12.756 | 0.159 | 10.019 | 1234.610 | 7 |

| Test type | Hydrostatic stress, MPa | Effective stress, MPa | Kirchhoff hydrostatic stress, MPa | Kirchhoff effective stress, MPa | CWD per initial vol., MJ $m^{-3}$ | Current density, kg $m^{-3}$ | Line |
|---|---|---|---|---|---|---|---|
| SR -1/6 | 15.711 | 36.087 | 6.838 | 22.844 | 15.004 | 1063.169 | 1 |
| Closed die | 20.833 | 36.082 | 11.956 | 20.381 | 15.007 | 1172.701 | 2 |
| SR 1/6 | 25.035 | 30.521 | 13.673 | 16.670 | 15.019 | 1232.229 | 3 |
| SR 1/3 | 29.043 | 23.454 | 15.423 | 12.455 | 15.011 | 1267.317 | 4 |
| SR 1/2 | 30.934 | 13.659 | 16.122 | 7.712 | 15.014 | 1291.355 | 5 |
| SR 2/3 | 31.975 | 7.251 | 16.516 | 3.745 | 15.018 | 1302.933 | 6 |
| Iso | 32.126 | 0.845 | 16.484 | 0.048 | 15.035 | 1311.685 | 7 |

| Test type | Hydrostatic stress, MPa | Effective stress, MPa | Kirchhoff hydrostatic stress, MPa | Kirchhoff effective stress, MPa | CWD per initial vol., MJ $m^{-3}$ | Current density, kg $m^{-3}$ | Line |
|---|---|---|---|---|---|---|---|
| SR -1/6 | 19.708 | 45.831 | 8.417 | 27.957 | 20.000 | 1103.299 | 1 |
| Closed die | 26.042 | 45.443 | 14.363 | 24.737 | 20.011 | 1220.205 | 2 |
| SR 1/6 | 31.514 | 38.059 | 16.485 | 19.908 | 20.010 | 1286.577 | 3 |
| SR 1/3 | 36.392 | 29.278 | 18.486 | 14.872 | 20.008 | 1324.943 | 4 |
| SR 1/2 | 38.703 | 17.415 | 19.317 | 9.334 | 20.001 | 1348.393 | 5 |
| SR 2/3 | 39.995 | 9.297 | 19.776 | 4.597 | 20.011 | 1361.051 | 6 |
| Iso | 40.223 | 0.728 | 19.737 | 0.242 | 20.030 | 1371.603 | 7 |

| Test type | Hydrostatic stress, MPa | Effective stress, MPa | Kirchhoff hydrostatic stress, MPa | Kirchhoff effective stress, MPa | CWD per initial vol., MJ $m^{-3}$ | Current density, kg $m^{-3}$ | Line |
|---|---|---|---|---|---|---|---|
| SR -1/6 | 23.564 | 55.125 | 9.850 | 32.622 | 25.009 | 1137.274 | 1 |
| Closed die | 30.984 | 54.457 | 16.562 | 28.764 | 25.003 | 1259.063 | 2 |
| SR 1/6 | 37.678 | 45.338 | 19.044 | 22.915 | 25.015 | 1331.566 | 3 |
| SR 1/3 | 43.357 | 34.955 | 21.272 | 17.150 | 25.010 | 1371.730 | 4 |
| SR 1/2 | 46.171 | 20.819 | 22.264 | 10.693 | 25.011 | 1395.668 | 5 |
| SR 2/3 | 47.645 | 11.149 | 22.763 | 5.326 | 25.005 | 1408.696 | 6 |
| Iso | 47.929 | 0.620 | 22.695 | 0.383 | 25.025 | 1421.304 | 7 |

| Test type | Hydrostatic stress, MPa | Effective stress, MPa | Kirchhoff hydrostatic stress, MPa | Kirchhoff effective stress, MPa | CWD per initial vol., MJ $m^{-3}$ | Current density, kg $m^{-3}$ | Line |
|---|---|---|---|---|---|---|---|
| SR -1/6 | 27.303 | 64.111 | 11.183 | 36.970 | 30.026 | 1167.82 | 1 |
| Closed die | 35.851 | 63.120 | 18.645 | 32.481 | 30.030 | 1294.113 | 2 |
| SR 1/6 | 43.613 | 52.410 | 21.415 | 25.735 | 30.029 | 1370.584 | 3 |
| SR 1/3 | 50.108 | 40.295 | 23.881 | 19.204 | 30.029 | 1412.152 | 4 |
| SR 1/2 | 53.356 | 24.007 | 24.999 | 11.889 | 30.007 | 1436.405 | 5 |
| SR 2/3 | 55.089 | 12.998 | 25.727 | 6.034 | 30.051 | 1449.814 | 6 |
| Iso | 55.368 | 0.387 | 25.452 | 0.530 | 30.034 | 1464.081 | 7 |

| Test type | Hydrostatic stress, MPa | Effective stress, MPa | Kirchhoff hydrostatic stress, MPa | Kirchhoff effective stress, MPa | CWD per initial vol., MJ $m^{-3}$ | Current density, kg $m^{-3}$ | Line |
|---|---|---|---|---|---|---|---|
| SR -1/6 | 34.484 | 81.334 | 13.624 | 44.947 | 40.029 | 1217.853 | 1 |
| Closed die | 45.105 | 79.845 | 22.412 | 39.290 | 40.031 | 1354.475 | 2 |
| SR 1/6 | 54.955 | 65.921 | 25.759 | 30.899 | 40.019 | 1435.829 | 3 |
| SR 1/3 | 62.983 | 50.304 | 28.581 | 22.827 | 40.016 | 1483.073 | 4 |
| SR 1/2 | 67.132 | 30.342 | 29.983 | 14.220 | 40.033 | 1506.858 | 5 |
| SR 2/3 | 69.202 | 16.426 | 30.546 | 7.267 | 40.042 | 1521.807 | 6 |
| Iso | 69.557 | 0.488 | 30.449 | 0.594 | 40.020 | 1537.379 | 7 |

| Test type | Hydrostatic stress, MPa | Effective stress, MPa | Kirchhoff hydrostatic stress, MPa | Kirchhoff effective stress, MPa | CWD per initial vol., MJ $m^{-3}$ | Current density, kg $m^{-3}$ | Line |
|---|---|---|---|---|---|---|---|
| SR -1/6 | 39.333 | 93.003 | 15.212 | 50.128 | 47.031 | 1248.656 | 1 |
| Closed die | 51.311 | 91.208 | 24.849 | 43.781 | 47.042 | 1389.696 | 2 |
| SR 1/6 | 62.560 | 75.104 | 28.541 | 34.264 | 47.002 | 1475.197 | 3 |
| SR 1/3 | 70.986 | 53.251 | 31.870 | 25.403 | 47.001 | 1506.256 | 4 |
| SR 1/2 | 76.298 | 34.825 | 33.119 | 15.773 | 47.010 | 1550.451 | 5 |
| SR 2/3 | 78.683 | 19.057 | 33.845 | 8.197 | 47.049 | 1564.630 | 6 |
| Iso | 79.162 | 0.336 | 33.692 | 0.983 | 47.058 | 1581.278 | 7 |

| Test type | Hydrostatic stress, MPa | Effective stress, MPa | Kirchhoff hydrostatic stress, MPa | Kirchhoff effective stress, MPa | CWD per initial vol., MJ $m^{-3}$ | Current density, kg $m^{-3}$ | Line |
|---|---|---|---|---|---|---|---|
| SR -1/6 | 44.829 | 106.016 | 16.904 | 55.695 | 55.101 | 1281.088 | 1 |
| Closed die | 58.273 | 103.800 | 27.480 | 48.547 | 55.045 | 1427.185 | 2 |
| SR 1/6 | 71.115 | 85.452 | 31.568 | 37.932 | 55.071 | 1516.133 | 3 |
| SR 1/3 | 80.144 | 45.367 | 35.235 | 28.015 | 55.001 | 1558.485 | 4 |
| SR 1/2 | 86.515 | 39.806 | 36.479 | 17.476 | 55.011 | 1596.140 | 5 |
| SR 2/3 | 88.697 | 6.578 | 37.404 | 9.119 | 55.072 | 1610.865 | 6 |
| Iso | 89.688 | 0.802 | 37.073 | 1.187 | 55.002 | 1628.203 | 7 |

| Test type | Hydrostatic stress, MPa | Effective stress, MPa | Kirchhoff hydrostatic stress, MPa | Kirchhoff effective stress, MPa | CWD per initial vol., MJ $m^{-3}$ | Current density, kg $m^{-3}$ | Line |
|---|---|---|---|---|---|---|---|
| SR -1/6 | 48.127 | 113.88 | 17.904 | 58.976 | 60.047 | 1299.605 | 1 |
| Closed die | 62.500 | 111.498 | 29.043 | 51.411 | 60.019 | 1448.319 | 2 |
| SR 1/6 | 76.323 | 91.686 | 33.351 | 40.063 | 60.064 | 1540.210 | 3 |
| SR 1/3 | 89.321 | 60.467 | 37.285 | 29.998 | 60.046 | 1601.322 | 4 |
| SR 1/2 | 92.785 | 42.962 | 38.464 | 18.501 | 60.045 | 1623.476 | 5 |
| SR 2/3 | 95.167 | 8.265 | 39.216 | 9.622 | 60.035 | 1642.542 | 6 |
| Iso | 96.237 | 0.915 | 39.105 | 1.252 | 60.054 | 1656.302 | 7 |

| Test type | Hydrostatic stress, MPa | Effective stress, MPa | Kirchhoff hydrostatic stress, MPa | Kirchhoff effective stress, MPa | CWD per initial vol., MJ $m^{-3}$ | Current density, kg $m^{-3}$ | Line |
|---|---|---|---|---|---|---|---|
| SR -1/6 | 54.641 | 129.495 | 19.839 | 65.307 | 70.019 | 1334.486 | 1 |
| Closed die | 70.830 | 126.710 | 32.013 | 56.860 | 70.010 | 1489.063 | 2 |
| SR 1/6 | 86.400 | 104.180 | 36.709 | 44.263 | 70.034 | 1584.024 | 3 |
| SR 1/3 | 101.435 | 65.124 | 41.228 | 32.634 | 70.051 | 1629.548 | 4 |
| SR 1/2 | 104.960 | 49.144 | 42.176 | 20.426 | 70.050 | 1674.874 | 5 |
| SR 2/3 | 106.254 | 8.264 | 42.608 | 10.574 | 70.004 | 1697.168 | 6 |
| Iso | 108.858 | 1.180 | 42.826 | 1.440 | 70.024 | 1710.689 | 7 |

| |
|---|
| Line |
| 1 |
| 2 |
| 3 |
| 4 |
| 5 |
| 6 |
| 7 |